

2016

# Graphene on nanoscale gratings for THz electron-beam radiation and plasmonics

---

<https://hdl.handle.net/2144/17076>

*"Downloaded from OpenBU. Boston University's institutional repository."*

BOSTON UNIVERSITY  
COLLEGE OF ENGINEERING

Dissertation

**GRAPHENE ON NANOSCALE GRATINGS FOR THZ ELECTRON-BEAM  
RADIATION AND PLASMONICS**

by

**KHWANCHAI TANTIWANICHAPAN**

B.A., King Mongkut's Institute of Technology Ladkrabang, 2001  
M.S., Boston University, 2011

Submitted in partial fulfillment of the  
requirements for the degree of  
Doctor of Philosophy

2016



Approved by

First Reader

---

Roberto Paiella, Ph.D.  
Professor of Electrical and Computer Engineering  
Professor of Materials Science and Engineering

Second Reader

---

Theodore Moustakas, Ph.D.  
Distinguished Professor Emeritus of Photonics and Optoelectronics  
Professor Emeritus of Electrical and Computer Engineering  
Professor Emeritus of Materials Science and Engineering  
Professor Emeritus of Physics

Third Reader

---

Anna Swan, Ph.D.  
Associate Professor of Electrical and Computer Engineering  
Associate Professor of Materials Science and Engineering

Fourth Reader

---

Alexander Sergienko, Ph.D.  
Professor of Electrical and Computer Engineering  
Professor of Physics

## **DEDICATION**

I would like to dedicate this work to my beloved family.

## ACKNOWLEDGMENTS

First of all, I would like to thank all professors in electrical engineering in Boston University who educate, support, and suggest me directly and indirectly both in class and research. Those are really valuable experiences in my graduate student path. Specially, I would like to honorably thank to my academic advisor, Professor Roberto Paiella who gives me an opportunity to do photonic semiconductor research what I am truly interested in. Thanks to his advices, his teachings, his patients and all his supports, I am valuably educated in intriguing research from the beginning to the end in my Ph.D. career.

I would like to thank to my committee members: Professor Theodore Moustakas, Professor Anna Swan and Professor Alexander Sergienko who sacrifice their precious time and their scholarly knowledge to evaluate my thesis work. Importantly, it is my pleasure to collaborate with Professor Swan in the project. She contributes distinctively intellectual opinion, which is considerably useful to my research.

I also would like to thank my collaborators Professor Cory Dean's group in Columbia University. Especially, Carlos who processes remarkable exfoliate graphene between hBN samples for my project and provides me useful information and discussion.

I am really grateful to my former and current group members: John, Faisal, Jeff, Cicek, Yin Jian, Habibe, Kogos, Xiaowei, Sunami and Yuyu for many technical helps, all supports and general discussions. Specifically, I am thankful to Jeff who patiently trained me all experimental skills. Also, it is my pleasure to collaborate with Xuanye Wang from Professor Swan's group who diligently improves and supplies numberless transferred graphene samples combined with Raman study for my research.

Last but not least, I am wholeheartedly grateful to my family for all mental and physical supports in everything. Thanks to my parents who are always besides me in every moment and make me being myself as present. I am also blessed to receive fully support from my siblings: Rugphon, Kannikar, and Teedanai who have been shared everything since we were born.

# **GRAPHENE ON NANOSCALE GRATINGS FOR THZ ELECTRON-BEAM**

## **RADIATION AND PLASMONICS**

**KHWANCHAI TANTIWANICHAPAN**

Boston University College of Engineering, 2016

Major Professor: Roberto Paiella, Ph.D., Professor of Electrical and Computer Engineering, Professor of Materials Science and Engineering

### **ABSTRACT**

Terahertz (THz) technologies have numerous applications such as biological and medical imaging, security screening, remote sensing, and industrial process control. However, the lack of practical THz sources and detectors is still a significant problem limiting the impact of these applications. In this Thesis work, three novel THz radiation mechanisms are proposed and investigated, based on the distinctive electronic properties of charge carriers in 2D single-layer graphene and related 1D conductors (i.e., graphene nanoribbons and carbon nanotubes), combined with the use of nanoscale dielectric gratings. Numerical simulations as well as fabrication and characterization activities are carried out.

The first proposed radiation mechanism is based on the mechanical corrugation of a single-layer sheet of graphene or 1D carbon conductor, deposited on a lithographically-defined sinusoidal grating. In the presence of a dc voltage, carriers will therefore undergo periodic angular motion and correspondingly radiate (similar to cyclotron emission but without the need for any external magnetic field). My numerical simulations indicate that technologically significant output power levels can correspondingly be obtained at geometrically tunable THz frequencies. Initial graphene samples on sinusoidal gratings

were fabricated and found to undergo significant strain redistribution, which affects their structural quality.

Charge carriers moving in a flat sheet of graphene or linear 1D carbon conductor parallel to a nanoscale grating can also produce THz radiation based on the Smith-Purcell effect. The role of the grating in this case is to diffract the evanescent electromagnetic fields produced by the moving electrons and holes so that THz light can be radiated. Once again, numerical simulations indicate that this approach is promising for the realization of ultra-compact THz sources capable of room-temperature operation. Initial experimental results with ultra-high-mobility graphene samples embedded in boron nitride films show promising THz electroluminescence spectra.

The last approach considered in this Thesis involves graphene plasmons at THz frequencies, which can be excited through the decay of hot electrons injected with an applied bias voltage. A nearby grating can then be used to outcouple the guided electromagnetic fields associated with these collective charge oscillations into radiation. The excitation of these THz plasmonic resonances at geometrically tunable frequencies has been demonstrated experimentally via transmission spectroscopy measurements.

## TABLE OF CONTENTS

DEDICATION .....	iv
ACKNOWLEDGMENTS .....	v
ABSTRACT .....	vii
TABLE OF CONTENTS .....	ix
LIST OF FIGURES .....	xi
LIST OF ABBREVIATIONS .....	xvii
1 INTRODUCTION .....	1
2 CYCLOTRON-LIKE TERAHERTZ RADIATION FROM CORRUGATED GRAPHENE .....	7
2.1 Proposed radiation mechanism .....	7
2.2 Simulation results.....	9
2.3 Sinusoidal grating fabrication and corrugated-graphene strain analysis .....	21
3 GRAPHENE ON NANOSCALE GRATINGS FOR THE GENERATION OF TERAHERTZ SMITH-PURCELL RADIATION .....	31
3.1 Proposed radiation mechanism .....	31
3.2 Simulation results.....	33
3.3 Sample fabrication .....	42
3.4 Electrical characteristic and electroluminescence measurements.....	45

4	TERAHERTZ ELECTRON-BEAM RADIATION IN 1D CARBON NANOSTRUCTURES .....	55
4.1	Proposed radiation mechanisms.....	56
4.1.1	Graphene nanoribbons .....	60
4.1.2	Carbon nanotubes.....	65
4.2	Simulation results.....	70
5	GRAPHENE TERAHERTZ PLASMONICS .....	81
5.1	Theoretical background .....	81
5.2	Sample fabrication .....	85
5.3	Transmission spectroscopy and electroluminescence results .....	89
6	CONCLUSION.....	93
	BIBLIOGRAPHY.....	95
	CURRICULUM VITAE.....	101

## LIST OF FIGURES

Figure 1.1 Graphene lattice (a) and reciprocal lattice (b) .....	4
Figure 1.2 (a) Energy band structure of graphene in its first Brillouin zone. (b) Graphene (2D) and graphene allotropes, i.e., carbon nanotube (1D) and Fullerene (0D). .....	4
Figure 1.3 Graphene Field Effect Transistor (GFET), charge distribution, and Fermi energy level ( $E_F$ ) for $V_{gs}=0$ , $V_{gs}>0$ , and $V_{gs}<0$ .....	5
Figure 2.1 Schematic illustration of the corrugated graphene geometry studied in this work. Two exemplary electron trajectories (with different values of the angle $\theta$ ) are also shown.....	8
Figure 2.2 Schematic illustration of the electric dipole distribution used in the FDTD simulations to compute the optical power radiated by an electron moving at constant speed in a sinusoidal trajectory. ....	12
Figure 2.3 Spectral properties of the THz radiation output of corrugated graphene. (a) Calculated radiation spectra emitted by individual electrons traveling along different trajectories, in the absence of collision broadening ( $\theta$ is the angle between the electron wavevector and the projection of the x-axis on the corrugated surface). (b) Total output spectrum computed using equation (2.6), including the effect of collision broadening for different values of the mean free path $d$ . The grating period and amplitude used in these simulations are 300 nm and 50 nm, respectively. ....	13
Figure 2.4 Peak emission frequency (circles) and total output power per unit area (squares) of corrugated graphene versus corrugation period (a) and versus corrugation amplitude (b). The amplitude and period in (a) and (b) are fixed at 50	

nm and 300 nm, respectively. The output power was computed using equation (2.6) assuming a carrier density of $5 \times 10^{12} \text{ cm}^{-2}$ and room temperature. ....	15
Figure 2.5 Far-field radiation pattern of a corrugated sheet of graphene with 300-nm period and 50-nm amplitude. Panels (a) and (b) contain polar plots of the emitted light intensity on the $xy$ and $xz$ planes, respectively (defined relative to the system of coordinates of Figure 2.1). ....	17
Figure 2.6 Schematic process flow for the fabrication of Si/SiO <sub>2</sub> nanoscale sinusoidal gratings. ....	23
Figure 2.7 AFM images of gratings fabricated on a Si substrate: (a) after a wet etch in KOH; (b) and (c) after a subsequent oxidation step followed by a buffered oxide etch to selectively remove the SiO <sub>2</sub> layer. In (a) and (b), the bottom left panel contains a plan-view surface-morphology image; a cross-sectional line scan is shown in the top panel, with its Fourier spectrum plotted in the bottom right panel. ....	23
Figure 2.8 Graphene on a silicon dioxide grating. Scale bar: 10 $\mu\text{m}$ . (a) Optical image. (b) Map of the Raman 2D-band peak center. (c) AFM height map. (d) AFM line profile. The red and green boxes correspond to the same regions in (a), (b) and (c). ....	27
Figure 2.9 Line scan of the Raman G band. Top through bottom: optical image of graphene, G peak center versus position, and G linewidth versus position. The blue, green and red boxes correspond to graphene on the flat surface (under compression), and on the grating under medium strain and high strain, respectively. ....	29

Figure 2.10 Friction versus strain. There is a clear indication of reduced friction with increasing uniaxial strain. The corresponding value of $\Delta\varepsilon/\mu\text{m}$ versus strain is marked on the right hand side. The purple diamond data point on the right shows the maximum strain variation predicted from the linewidth broadening calculation. ....	30
Figure 3.1 (a) Schematic illustration of the sample geometry investigated in this chapter. (b) Close-up image of the hole array of (a), with a pictorial definition of some of the key parameters used in the simulations. ....	34
Figure 3.2 Single-electron radiation spectra for different values of the mean free path $d$ , produced by an electron traveling at an angle $\theta_{\mathbf{k}} = 0^\circ$ (a) and $10^\circ$ (b) with respect to the $x$ direction in the sample geometry of Figure 3.1. The array period is 100 nm. The arrows in the insets show the direction of the electron velocity. ....	37
Figure 3.3 Far-field radiation pattern in the array substrate produced by an electron traveling in the $x$ direction, for $\Lambda = 100$ nm and $d = 1$ $\mu\text{m}$ . The $x$ - $y$ coordinate system is the same as in Figure 3.1(b) .....	38
Figure 3.4 Emission spectra of three graphene SP samples of different period $\Lambda$ , computed with a mean free path $d$ of 1 $\mu\text{m}$ . The total output power per unit area of each structure, integrated over all frequencies, is also listed in the inset. ....	41
Figure 3.5 Schematic process flow for the fabrication of samples involving hBN-graphene-hBN heterostructures on 2D hole arrays. ....	44
Figure 3.6 SEM and AFM image of a 2D hole array with 200-nm period and 100-nm hole diameter on an $\text{SiO}_2/\text{Si}$ substrate fabricated by EBL, and RIE. ....	44

Figure 3.7 Optical image of an hBN-graphene-hBN stack transferred on top of a hole array (blue areas) with metal contacts (yellow areas).....	45
Figure 3.8 (a) Room-temperature conductivity of the sample of Figure 3.7 vs carrier density. (b) Mean free path vs mobility for different values of the carrier density. .	47
Figure 3.9 Electroluminescence measurement setup. ....	49
Figure 3.10 Emission spectrum with different gate voltage $V_{gs}$ at liquid nitrogen temperature 77 (a), and at room temperature 300 K (b) with fixed $I_{ds} = 24\text{mA}$ . ....	51
Figure 3.11 Emission spectrum with different gate voltage $V_{gs}$ at liquid nitrogen temperature 77 (a), and at room temperature 300 K (b) with fixed $I_{ds} = 28\text{mA}$ . ....	53
Figure 4.1 : Schematic cross-sectional view of representative device structures for the demonstration of THz electron-beam radiation in 1D carbon nanostructures. (a) Corrugated carbon nanowire for the generation of cyclotron-like THz radiation. (b) Carbon nanowire in the near-field vicinity of a grating for the generation of THz Smith-Purcell radiation. ....	57
Figure 4.2 Crystal structure of the 1D carbon nanostructures under study. (a) ZZ-GNR. (b) AC-SWNT. In (a), $a_1$ and $a_2$ are the basis vectors of the crystal lattice, $C_h$ is the chiral vector, and the letters A and B indicate representative atoms belonging to the two sub-lattices. ....	61
Figure 4.3 Electronic band structure of a ZZ-GNR with 40-nm width. The wavevector $k$ is measured along the axis of the nanoribbon, relative to the center of the graphene first Brillouin zone. ....	64

Figure 4.4 Electronic band structure of an AC-SWNT with 2-nm diameter. The wavevector $k$ is measured along the axis of the nanotube, relative to the center of the graphene first Brillouin zone. ....	66
Figure 4.5 Photon emission rate per unit frequency of an electron in a corrugated carbon nanowire, plotted as a function of radiated frequency for different values of the electron velocity $v_k$ . The corrugation period and amplitude are 68 nm and 17 nm, respectively. Inset: total emission rate of the same electron, integrated over all frequencies, versus electron velocity. ....	73
Figure 4.6 Output radiation spectra per unit length for different periods of the grating or corrugation: (a) cyclotron-like radiation from sinusoidally corrugated ZZ-GNRs; (b) Smith-Purcell emission from ZZ-GNRs near a rectangular grating; (a) cyclotron-like radiation from sinusoidally corrugated AC-SWNTs; (b) Smith-Purcell emission from AC-SWNTs near a rectangular grating. ....	76
Figure 4.7 Total output power per unit length of the structures of Figure 4.6, integrated over all frequencies and plotted as a function of the corresponding frequency of peak emission. ....	77
Figure 4.8 Output radiation spectra per unit length for different values of the electronic mean free path: (a) cyclotron-like radiation from sinusoidally corrugated ZZ-GNRs; (b) Smith-Purcell emission from ZZ-GNRs near a rectangular grating; (a) cyclotron-like radiation from sinusoidally corrugated AC-SWNTs; (b) Smith-Purcell emission from AC-SWNTs near a rectangular grating. ....	79

Figure 5.1 (a) Surface plasmons at the interface between a metal and a dielectric. (b)	
Dispersion relation of surface plasmons (solid line) and of radiation in the bulk	
dielectric material (dash line).....	82
Figure 5.2 Resonance frequency of grating-coupled graphene plasmons versus carrier	
density, for different values of the grating period.....	84
Figure 5.3 Schematic process flow for the fabrication of pillar arrays on graphene. ....	86
Figure 5.4 CVD graphene for transmission measurements, after patterning (a) and after	
deposition of the pillar array and source-drain contacts (b). ....	88
Figure 5.5 Transmission spectrum from plasmons graphene sample with 1.5 $\mu\text{m}$ period (a)	
and 5 $\mu\text{m}$ period (b) 2D metal pillar array. ....	90
Figure 5.6 Transmission spectrum from plasmons graphene sample with different period	
P. ....	91

## LIST OF ABBREVIATIONS

2DEG .....	Two Dimensional Electron Gas
AC.....	Alternative Current
AC-SWNTs.....	Armchair Single Wall Nanotubes
ADC .....	Analog to Digital Converter
AFM.....	Atomic Force Microscopy
AlGaAs .....	Aluminum Gallium Arsenide
Au.....	Gold
BOE.....	Buffered Oxide Etch
CHF <sub>3</sub> .....	Fluoroform
Cr.....	Chromium
CVD .....	Chemical Vapor Deposition
DC.....	Direct Current
EBL.....	Electron Beam Lithography
FDTD .....	Finite Different Time Domain
FELs .....	Free Electron Lasers
FTIR.....	Fourier Transform Infrared Spectrometer
FWHM .....	Full Width Half Maximum
GaAs .....	Gallium Arsenide
GFET.....	Graphene Field Effect Transistor
GHz.....	Gigahertz
hBN .....	hexagonal Boron Nitride

I-V .....	Current-Voltage
KOH .....	Potassium Hydroxide
LEDs .....	Light Emitting Diodes
LIA .....	Lock-In Amplifier
Pd .....	Palladium
PDMS .....	Polydimethylsiloxane
PMMA .....	Polymethyl Methacrylate
PPC .....	Poly-Propylene Carbonate
PVP .....	Polyvinylpyrrolidone
QCL .....	Quantum Cascade Lasers
RIE .....	Reactive Ion Etch
sccm .....	Cubic Centimeter per Minute
SEM .....	Scanning Electron Microscope
Si .....	Silicon
SiC .....	Silicon Carbide
SiGe .....	Silicon Germanium
SiO <sub>2</sub> .....	Silicon Dioxide
SP .....	Smith-Purcell
THz .....	Terahertz
ZZ-GNRs .....	Zigzag Graphene Nanoribbons

## 1 INTRODUCTION

THz technologies can provide unique imaging and sensing capabilities, related to the ability of THz light to penetrate through common packaging materials with little attenuation, and to the presence of distinctive rotational/vibrational resonances at THz frequencies in many molecules of interest. These properties enable a wide range of applications, e.g., for security screening, manufacturing quality control, and medical diagnostics. However, despite the obvious significance and timeliness of these applications, to date terahertz technologies remain relatively underutilized, mostly due to the lack of practical sources. Of particular importance are electrically driven solid-state emitters, which can provide unparalleled miniaturization, low power consumption, and suitability to large-scale integration.

Light emission in semiconductors typically occurs via electronic transitions between different energy bands in bulk samples, or between quantum-confined states in low-dimensional systems. These emission processes form the basis of several well established devices operating at visible and infrared wavelengths, such as LEDs, diode lasers, and quantum cascade lasers. In recent years, their domain has also been extended to longer and longer wavelengths across the far-infrared spectrum through the development of THz quantum cascade lasers, whose operation however is fundamentally limited to cryogenic temperatures (Williams 2007). An alternative class of radiation mechanisms in solid-state systems involves the periodic acceleration of charge carriers under static bias conditions. This approach is similarly well established at microwave frequencies, as in the case of electronic oscillators such as tunneling diodes, transit-time devices, and Gunn

diodes. In recent years, several efforts have also been devoted to devise similar processes suitable for THz light emission, motivated by fundamental questions about ultrafast carrier dynamics in low-dimensional systems as well as the emerging need for practical solid-state THz sources (Lee and Wanke 2007). However, the resulting mechanisms mostly require cryogenic temperatures, and generally produce extremely broad and weak radiation spectra. These limitations are fundamentally related to basic material properties of traditional semiconductors, such as limited carrier velocities, low mobilities at room temperature, and broad thermal distributions of drift velocities.

The recent emergence of graphene, with its unique electronic and mechanical properties, offers a new perspective and fundamental benefits. The carbon atoms in graphene are connected to one another in a honeycomb lattice with  $sp^2$  hybridization, i.e., each atom makes three  $\sigma$ -bonds consisting of three hybridized valence electrons  $2s^1$ ,  $2p^1$ , and  $2p^2$  with its three nearest neighbor atoms as shown by the black lines in Figure 1.1(a). The remaining non-hybridized valence electron  $2p^3$  forms a  $\pi$ -like orbital, as indicated by the green lines. As clearly established by extensive experimental and theoretical work (Novoselov et al. 2004; Novoselov et al. 2005; Zhang et al. 2005; Berger et al. 2006; Castro Neto et al. 2009), charge transport in these single-layer sheets of carbon is dominated by these  $2p^3$  valence electrons leading to exceptional electronic properties.

The unit cell of the graphene lattice is triangular with basis vectors  $\mathbf{a1}$  and  $\mathbf{a2}$  (shown in Figure 1.1(a)) and contains two non-equivalent carbon atoms, denoted A and B. The corresponding first Brillouin zone with its reciprocal lattice vectors  $\mathbf{b1}$  and  $\mathbf{b2}$  is shown in Figure 1.1(b). The energy band diagram can be obtained with the tight binding

approximation by only including the coupling between nearest-neighbor atoms, leading to the following expression

$$E_{\pm}(\mathbf{k}) = \pm t \sqrt{1 + 4 \cos\left(\frac{\sqrt{3}k_x a}{2}\right) \cos\left(\frac{k_y a}{2}\right) + 4 \cos^2\left(\frac{k_y a}{2}\right)} \quad (1.1)$$

where  $a$  is the lattice parameter (i.e., the length of the basis vectors  $\mathbf{a}_1$  and  $\mathbf{a}_2$ ) and  $t$  is the nearest-neighbor hopping parameter. The plus and minus signs in this formula correspond to the conduction and valence bands, respectively. According to equation (1.1), the bandgap energy  $E_+ - E_-$  is zero at two distinct high-symmetry points within the first Brillouin zone, labeled K and K', as shown in Figure 1.2(a). In the vicinity of these points, both bands have conical dispersion  $E_{\pm} \approx \pm \hbar v_F k$ , where the wavevector  $k$  is measured from K or K' and  $v_F = (\sqrt{3}ta)/2$  is the Fermi velocity. This behavior is similar to that of ultra-relativistic particles described by the massless Dirac equation (albeit at smaller speeds). As illustrated in Figure 1.2(b), a 2D sheet of graphene can be rolled up to form a 1D carbon nanotube or 0D Fullerene, or can be stacked up to form 3D graphite, resulting in all cases in very different electronic properties.

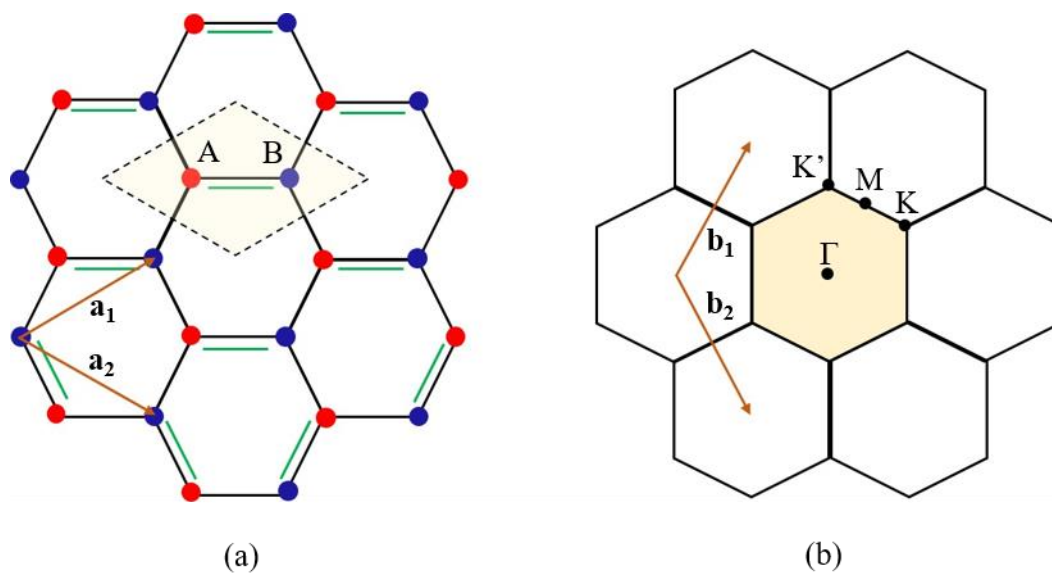


**Figure 1.1** Graphene lattice (a) and reciprocal lattice (b)

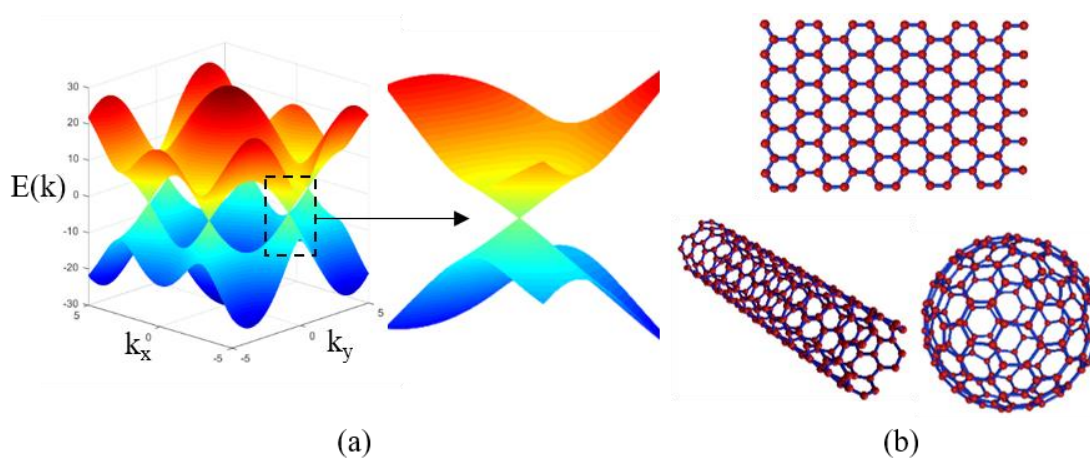


**Figure 1.2** (a) Energy band structure of graphene in its first Brillouin zone. (b) Graphene (2D) and graphene allotropes, i.e., carbon nanotube (1D) and Fullerene (0D).

An important device configuration commonly used with graphene is the graphene field effect transistor (GFET). With this geometry, large densities of electrons or holes can

be created in the graphene conduction and valence bands in a highly controllable fashion through the application of a gate voltage, as shown in Figure 1.3. The resulting carrier density ( $n$ ) in graphene can be calculated from the equation (Bolotin et al. 2008; Du et al. 2008),

$$n = \frac{\epsilon_0 \epsilon_r V_{gs}}{q t_{ox}} \quad (1.2)$$

where  $\epsilon_0$  is the permittivity of free space,  $\epsilon_r$  is the relative dielectric constant of  $\text{SiO}_2$ ,  $V_{gs}$  is the applied Gate-Source voltage,  $q$  is the electron charge, and  $t_{ox}$  is the thickness of the  $\text{SiO}_2$  layer.

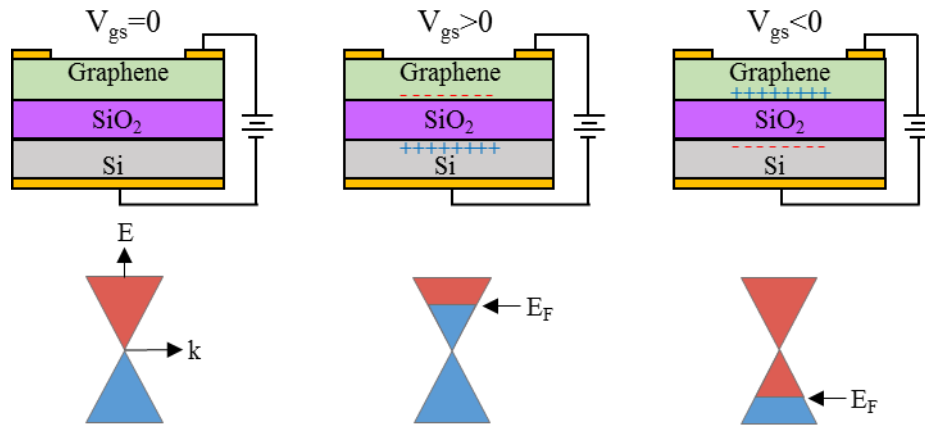


**Figure 1.3 Graphene Field Effect Transistor (GFET), charge distribution, and Fermi energy level ( $E_F$ ) for  $V_{gs}=0$ ,  $V_{gs}>0$ , and  $V_{gs}<0$**

With the setup of Figure 1.3, exceptional electronic transport properties have been demonstrated, including micrometer-scale ballistic transport and record large room-temperature mobilities above  $1 \times 10^5 \text{ cm}^2/\text{Vs}$  in suspended samples (Bolotin et al. 2008; Du et al. 2008), and in samples deposited on atomically smooth, highly inert hexagonal boron nitride (hBN) films (Dean et al. 2010; Mayorov et al. 2011). Potential device applications

to THz photonics have also been investigated recently (Ryzhii, Ryzhii, and Otsuji 2007; Rana 2008; Sun et al. 2010; Ju et al. 2011; Boubanga-Tombet et al. 2012; Prechtel et al. 2012; Sensale-Rodriguez et al. 2012; Yan et al. 2012; Ren et al. 2012; Vicarelli et al. 2012), mostly based on interband electronic transitions and related to the ultrafast carrier relaxation/recombination dynamics near the Dirac points. In particular, THz amplification (Boubanga-Tombet et al. 2012) and spontaneous emission (Prechtel et al. 2012) under optical pumping have already been reported. The use of tunable plasmonic excitations in electrostatically gated graphene is also being widely investigated for several infrared (including THz) device applications (Rana 2008; Ju et al. 2011; Yan et al. 2012; Koppens, Chang, and Garcia De Abajo 2011).

The fundamental goal of this work is to show that, by virtue of their distinctive electronic properties (including linear energy dispersion, relatively large Fermi velocity, and ultra-high mobilities), charge carriers in graphene and related 1D conductors are ideally well suited to radiation mechanisms that so far have been the primary domain of high-energy electron beams in vacuum-based systems. Such mechanisms include cyclotron emission, the Smith-Purcell effect (S. J. Smith and Purcell 1953; Wirner et al. 1993) and more in general Cherenkov radiation in photonic crystals (Luo et al. 2003), all of which involve charges traveling at constant speed in the presence of a periodic spatial modulation (in either their trajectory or the surrounding dielectric environment).

## **2 CYCLOTRON-LIKE TERAHERTZ RADIATION FROM CORRUGATED GRAPHENE**

### **2.1 Proposed radiation mechanism**

In this chapter, I investigate the use of sinusoidally corrugated graphene for the generation of THz light based on a novel cyclotron-like radiation process. The required geometry, illustrated schematically in Figure 2.1, could be obtained by depositing a sheet of graphene on a grating patterned on the surface of a suitable substrate (e.g., an oxidized silicon wafer, as commonly employed in graphene electronics). Because of the ultrasmall thickness (i.e., single-atomic-layer) of graphene, conformal adhesion to the corrugated surface can be expected even with sub-micron grating periodicities. In the presence of a dc voltage in the direction of the corrugation, electrons (or holes) introduced in the graphene sheet via field doping will therefore undergo periodic angular motion and correspondingly radiate.

This mechanism is well established in the context of vacuum electron-beam devices such as free-electron lasers (Marshall 1985). However, it represents a novel paradigm for light emission in condensed matter, and the formal analogy between electrons and holes in graphene and relativistic charges provides a natural motivation for its study. The use of geometrical constraints (as opposed to the application of an external magnetic field) to obtain radiation via angular motion is also fundamentally new. Specifically, in the case of a free-electron laser sinusoidal carrier trajectories are obtained with a periodic array of magnets with alternating poles (the undulator). In the present context, the same periodic angular motion is instead produced by the graphene mechanical corrugation, combined

with its two-dimensional nature that ensures that the carrier trajectories perfectly conform to the corrugation.

The basic radiation properties of charges under periodic angular motion can be calculated using classical electrodynamics (Jackson 1975; Fedorchenko et al. 2010). From the Larmor formula, when a charge travels with constant velocity  $v_0$  along a sinusoidal trajectory, radiation is emitted with power  $P_{ch}$  and frequency  $f_{rad}$  given by

$$f_{rad} = \frac{v_0}{\Lambda} \quad (2.1)$$

$$P_{ch} = \frac{4\pi^3 q^2 A^2 v_0^4}{3\epsilon_0 c^3 \Lambda^4} \quad (2.2)$$

Here,  $\Lambda$  and  $A$  are the period and amplitude of the sinusoidal trajectory, respectively, and the assumptions  $v_0 \ll c$  and  $A \ll \Lambda$  are made.

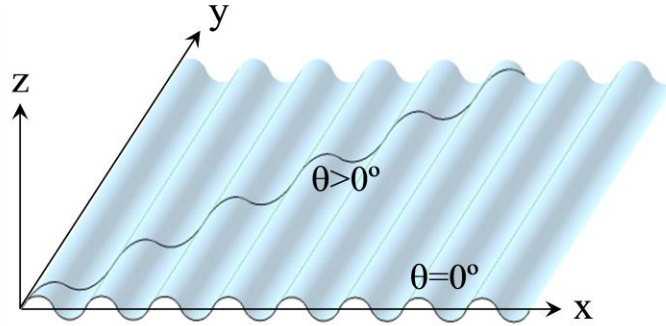


**Figure 2.1 Schematic illustration of the corrugated graphene geometry studied in this work. Two exemplary electron trajectories (with different values of the angle  $\theta$ ) are also shown**

Recently, a theoretical analysis based on these expressions has been applied to the case of charge transport in periodically corrugated SiGe heterojunctions (Fedorchenko et al. 2010). Equations (2.1) and (2.2), while only approximate, can be used to substantiate

the advantages of the unique electronic structure of graphene for this application. Due to the linear energy dispersion near the Dirac points, all conduction electrons and holes in graphene travel at the same speed  $dE/d(\hbar k) = v_F = 10^8$  cm/s. This value is substantially larger than the maximum drift velocities achievable in typical semiconductors (by about an order of magnitude), which is desirable due to the  $v_0^4$  dependence of the emitted power [see equation (2.2)]. At the same time, proportionally higher emission frequencies  $f_{rad}$  within the THz spectral region can be obtained with graphene using realistic corrugation periods  $\Lambda$  on the order of a few hundred nanometers [see equation (2.1)]. Furthermore, in a traditional two-dimensional electron gas with a parabolic energy band, the electron speed varies (linearly) with wavenumber  $k$ . As a result, in the geometry of Figure 2.1, a much narrower distribution of the electron velocity component along the direction of the corrugation can be expected in graphene compared to conventional semiconductors, particularly under highly non-equilibrium conditions. Since the cyclotron emission frequency  $f_{rad}$  is proportional to this velocity component [ $v_0$  in equation (2.1)], the end result is a narrower and therefore stronger emission spectrum.

## 2.2 Simulation results

In my thesis work, I have simulated electron-beam radiation from corrugated graphene (Tantiwanichapan et al. 2013) by using the FDTD (Finite-difference time-domain) method with the Lumerical software package (“FDTD Solutions” 2009). In order to apply the FDTD method to this problem, I take advantage of the formal equivalence between a time-varying distribution of electric dipoles [described by a polarization density  $\mathbf{P}(\mathbf{r}, t)$ ] and the

current density  $\mathbf{J}(\mathbf{r}, t) = \partial \mathbf{P}(\mathbf{r}, t) / \partial t$  [i.e.,  $\mathbf{J}(\mathbf{r}, \omega) = -i\omega \mathbf{P}(\mathbf{r}, \omega)$  in the frequency domain]. As a result of this equivalence, the radiation output of any accelerated charge [carrying a current density  $\mathbf{J}(\mathbf{r}, t)$ ] is identical to that of the polarization density  $\mathbf{P}(\mathbf{r}, t)$  whose time derivative is equal to  $\mathbf{J}(\mathbf{r}, t)$ . Once the equivalent dipole distribution described by this polarization density is identified, it can be readily modeled using the built-in dipole radiation sources of the FDTD simulation engine.

Specifically, I consider an electron in an arbitrary Bloch state of wavevector  $\mathbf{k}$  (measured from the nearest Dirac point), in the presence of a sinusoidal corrugation along the x direction having amplitude  $A$  and period  $\Lambda$ . In the plane of the graphene sheet, the electron travels at constant speed  $v_F = 10^8$  cm/s along the direction of  $\mathbf{k}$ . Due to the corrugation, this direction varies as a function of position, while remaining at a fixed angle  $\theta$  with respect to the projection of the x-axis on the corrugated surface. In terms of the system of coordinates shown in Figure 1.1, the electron trajectory can be written as

$$\mathbf{r}_e(t) = \hat{\mathbf{x}}x_e(t) + \hat{\mathbf{y}}l(x_e(t))\tan\theta + \hat{\mathbf{z}}A\sin(px_e(t)) \quad (2.3)$$

where  $x_e(t)$  is the instantaneous position along the x direction,  $p = 2\pi/\Lambda$  is the corrugation wavenumber, and

$$l(x) = \int_0^x d\xi \sqrt{1 + A^2 p^2 \cos^2(p\xi)} \quad (2.4)$$

is the arc length of the corrugation profile along the x direction. The variable  $x_e(t)$  can be calculated numerically as a function of time from the equation  $|\dot{\mathbf{r}}_e(t)| = v_F$ , which simply expresses the condition that the electron speed is constant and equal to  $v_F$ , regardless of the wavevector  $\mathbf{k}$  and the externally applied electric field.

The current density carried by the electron is simply related to its trajectory as  $\mathbf{J}(\mathbf{r}, t) = -q\mathbf{r}'_e(t)\delta(\mathbf{r} - \mathbf{r}_e(t))$ . To determine the equivalent polarization density, I Fourier transform  $\mathbf{J}(\mathbf{r}, t)$  and divide the result by  $-i\omega$ , leading to the following expression:

$$\begin{aligned} \mathbf{P}(\mathbf{r}, \omega) = & \frac{q}{i\omega} [\hat{\mathbf{x}} + \hat{\mathbf{y}}l'(x)\tan\theta + \hat{\mathbf{z}}A\cos(px)] \\ & \times \delta(y - l(x)\tan\theta)\delta(z - A\sin(px)) \end{aligned} \quad (2.5)$$

where  $l' = dl/dx$  and  $t(x)$  is the time instant where the electron position along the corrugation satisfies  $x_e(t) = x$ .

Equation (2.5) describes a continuous distribution of electric dipoles linearly positioned on the charge trajectory, having position-dependent magnitude, phase, and direction of the dipole moment. In the FDTD simulations, this distribution is discretized into a collection of neighboring dipoles separated by a small distance  $\Delta x$  along the  $x$  direction, with  $\Delta x \ll \Lambda$ . A schematic plot of such an ensemble is shown in Figure 2.2, where each dipole is represented by a circle centered about its position and by an arrow in the direction of its moment.

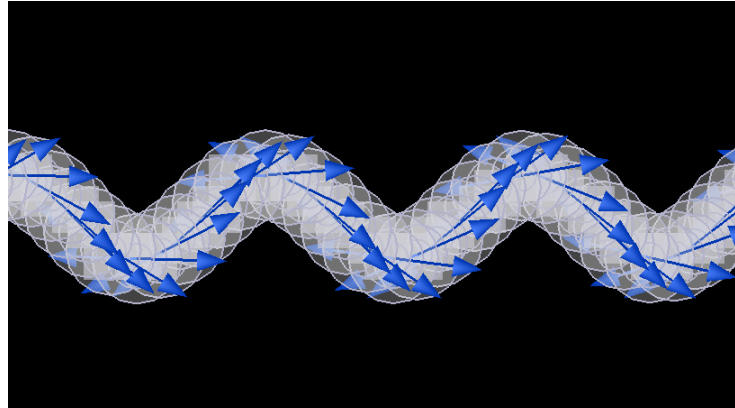


**Figure 2.2 Schematic illustration of the electric dipole distribution used in the FDTD simulations to compute the optical power radiated by an electron moving at constant speed in a sinusoidal trajectory.**

In Figure 2.3(a) I plot the calculated radiation spectra produced by such dipole distributions, for different trajectories (i.e., different values of the angle  $\theta$ ) on a sinusoidal corrugation of period  $\Lambda = 300$  nm and amplitude  $A = 50$  nm. As explained in the preceding paragraphs, these results also describe light emission from a single electron traveling along the same trajectories at constant speed  $v_F$ . In the case of motion along the direction of the corrugation (i.e.,  $\theta = 0^\circ$ ), the emission spectrum of Figure 2.3(a) consists of a sharp peak centered at about 2.7 THz and a weaker feature at twice that frequency. These emission lines can be simply interpreted as the result of constructive interference among the output fields of all the radiating dipoles in the equivalent dipole distribution (higher-order harmonics, not included in the figure, are also present). The peak emission frequency of 2.7 THz is smaller than the predicted radiation frequency  $f_{rad} = 3.33$  THz based the approximate formula of equation (2.1) for  $\Lambda = 300$  nm and  $\theta = 0^\circ$  (i.e.,  $v_0 = v_F$ ). The difference is due to the non-negligible corrugation amplitude of the trajectories considered

in Figure 2.3(a) ( $A = 50$  nm), whereas equation (2.1) assumes  $A \ll \Lambda$ . When this assumption is not satisfied, the distance traveled per period is substantially larger than  $\Lambda$  and the oscillation time is proportionally longer than  $\Lambda/v_0$ . As the angle  $\theta$  is increased and the electron velocity along the direction of the corrugation ( $v_0 \approx v_F \cos\theta$ ) correspondingly decreases, the radiation spectrum is found to red-shift and decrease in peak value. These observations are consistent with equations (2.1) and (2.2), which predict a decrease in both emission frequency  $f_{rad}$  and output power  $P_{ch}$  with decreasing  $v_0$ .

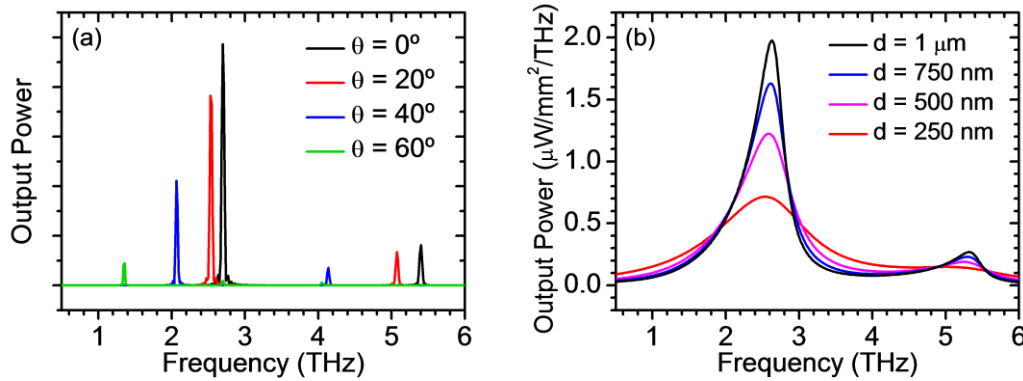


**Figure 2.3 Spectral properties of the THz radiation output of corrugated graphene. (a) Calculated radiation spectra emitted by individual electrons traveling along different trajectories, in the absence of collision broadening ( $\theta$  is the angle between the electron wavevector and the projection of the x-axis on the corrugated surface). (b) Total output spectrum computed using equation (2.6), including the effect of collision broadening for different values of the mean free path  $d$ . The grating period and amplitude used in these simulations are 300 nm and 50 nm, respectively.**

The emission lines of Figure 2.3(a) feature extremely narrow spectral widths, as small as a few ten GHz. In practice, substantial spectral broadening can be expected due to various electronic scattering processes, involving, e.g., charged surface states in the

graphene substrate, phonons, and surface roughness, which are clearly not included in the FDTD simulations just described. Their impact can be quantified as a broadening of the emission lines by the amount  $\Delta f = v_F/\pi d$  (where  $d$  is the mean free path between consecutive collisions) (Oster 1960), and a proportional lowering of their peak values. In Figure 2.3(b) I show the radiation spectrum produced by an electronic ensemble in graphene in the presence of the 300-nm-period, 50-nm-amplitude corrugation considered so far, for different values of  $d$ . These traces were obtained by adding up the single-electron spectra corresponding to different electron trajectories [such as the examples shown in Figure 2.3(a)], each convolved with a Lorentzian lineshape function of full width at half maximum  $\Delta f$ . More details of the computation method are presented below. It follows from this figure that pronounced emission spectra with reasonably large quality factors can be expected even with mean free paths of a few hundred nanometers. Such values can be achieved in high-quality graphene samples even at room temperature (Bolotin et al. 2008; Mayorov et al. 2011), which is another key enabling attribute of graphene in the present context.

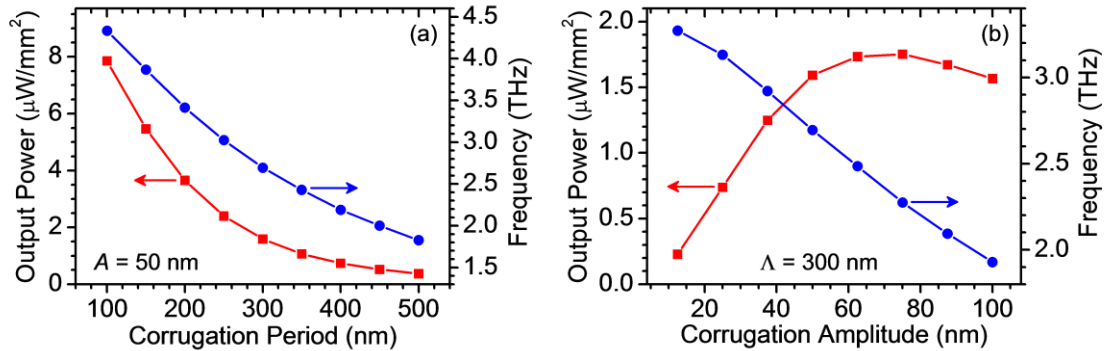


**Figure 2.4** Peak emission frequency (circles) and total output power per unit area (squares) of corrugated graphene versus corrugation period (a) and versus corrugation amplitude (b). The amplitude and period in (a) and (b) are fixed at 50 nm and 300 nm, respectively. The output power was computed using equation (2.6) assuming a carrier density of  $5 \times 10^{12} \text{ cm}^{-2}$  and room temperature.

The circles in Figure 2.4(a) represent the calculated frequency of peak emission (i.e., the main radiation frequency of the  $\theta = 0^\circ$  sinusoidal trajectory) plotted as a function of corrugation period  $\Lambda$  for fixed amplitude  $A = 50$  nm. The observed red-shift with increasing period is in agreement with equation (2.1), although the values plotted in Figure 2.4(a) are consistently smaller than the predictions of this simple formula. The discrepancy is again due to the underlying assumption of equation (2.1), i.e.,  $A \ll \Lambda$ , which is not fully justified in the geometries under study. As shown in Figure 2.4(b) (where a constant period of 300 nm is assumed), the emission frequency also decreases with increasing corrugation amplitude, which can be ascribed to the resulting increase in travel time per period. In any case, the important conclusion from these plots is that radiation frequencies across a wide portion of the THz spectrum can be obtained with realistic values of  $A$  and  $\Lambda$  on the order of several ten and a few hundred nanometers, respectively. Such values can be readily

obtained in surface-relief gratings based on current nanofabrication technologies, which can then be used as substrates for the conformal adhesion of pre-synthesized graphene sheets.

The same FDTD simulations can also be used to determine the far-field radiation pattern of the emitted light. Exemplary results are shown in Figure 2.5, for the case of an electron traveling along the  $\theta = 0^\circ$  trajectory on a sinusoidal corrugation with 300-nm period and 50-nm amplitude. Each panel in the figure contains a polar plot of the far-field output intensity (at the frequency of peak emission), on a different Cartesian plane relative to the system of coordinates of Figure 2.1. In the limit of negligibly small corrugation amplitude relative to the period, simple electromagnetic considerations based on the Larmor formula indicate that the far-field radiation pattern approaches that of a dipole oriented along the z direction. The results plotted in Figure 2.5 still resemble such a field profile, except that they are not symmetric with respect to reflections about the yz plane, with more light emitted along the negative x direction (i.e., antiparallel to the electronic motion) compared to the positive x direction. These considerations are of course important for the purpose of experimentally measuring and quantifying the emitted light intensity.

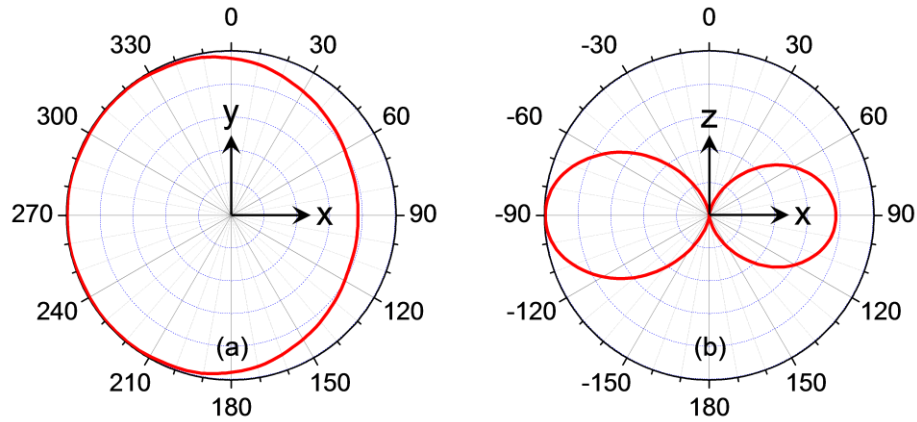


**Figure 2.5** Far-field radiation pattern of a corrugated sheet of graphene with 300-nm period and 50-nm amplitude. Panels (a) and (b) contain polar plots of the emitted light intensity on the  $xy$  and  $xz$  planes, respectively (defined relative to the system of coordinates of Figure 2.1).

Finally, I address the question of how much THz power can be obtained based on the radiation mechanism described in this chapter. Specifically, I consider an n-doped corrugated graphene sheet of electron density  $N$ , under the action of an externally applied voltage producing an electric field  $\hat{x}E$  in the direction of the corrugation. The total emission spectrum  $P_{tot}(\nu)$  can be computed as follows:

$$P_{tot}(\nu) = 4 \sum_{\mathbf{k}} P_e(\mathbf{k}, \nu) f(\mathbf{k}) [1 - f(\mathbf{k}')] \quad (2.6)$$

where the factor of 4 accounts for the spin and valley degeneracies,  $P_e(\mathbf{k}, \nu)$  is the power radiated by an electron in the conduction-band Bloch state of wavevector  $\mathbf{k}$  (i.e., its photon-emission rate times the photon energy),  $f(\mathbf{k})$  is the probability that this initial state is occupied, and  $1 - f(\mathbf{k}')$  is the probability that the corresponding final state after photon emission is empty. The wavevector  $\mathbf{k}'$  of the latter state is related to the initial electronic wavevector  $\mathbf{k}$  by the requirements of conservation of energy, i.e.,  $E(\mathbf{k}) - E(\mathbf{k}') = h\nu$  and

conservation of momentum along the y direction (where the system under study has translational invariance), i.e.,  $k_y' = k_y$ .

The single-electron radiation spectra  $P_e(\mathbf{k}, \nu)$  for different wavevectors  $\mathbf{k}$  can be calculated via the FDTD simulations described earlier [e.g., as plotted in Figure 2.3(a)], further convolved with a Lorentzian lineshape function to account for collision broadening as already discussed. For any given corrugation geometry, these spectra only depend on the electron velocity  $v_{\hat{\mathbf{k}}} = v_F \hat{\mathbf{k}}$  which in turn depends on the direction of  $\mathbf{k}$  but not on its magnitude. Therefore,  $P_e(\mathbf{k}, \nu)$  can be written as  $P_e(\theta, \nu)$ , where  $\theta$  is the angle between  $\mathbf{k}$  and the projection of the x-axis on the corrugated surface, as defined previously. To determine the occupation probabilities  $f(\mathbf{k})$ , I use a semiclassical model of carrier dynamics in crystalline solids (Kittel 1986), where an externally applied electric field  $\hat{\mathbf{x}}E$  has the effect of simply displacing the equilibrium Fermi-Dirac distribution function  $f_0(\mathbf{k})$  as a whole by the amount

$$\delta\mathbf{k} = -\hat{\mathbf{x}} \frac{q}{\hbar} \tau_{\mathbf{k}} E = -\hat{\mathbf{x}} k \frac{\mu E}{v_F} \quad (2.7)$$

leading to  $f(\mathbf{k}) = f_0(\mathbf{k} - \delta\mathbf{k})$ . In equation (2.7),  $\tau_{\mathbf{k}}$  is the momentum relaxation time,  $\mu$  is the mobility, and the second equality is obtained by assuming  $\tau_{\mathbf{k}} = (\mu \hbar k)/(q v_F)$ , an expression that appears to be consistent with the key electronic transport properties of graphene (Castro Neto et al. 2009).

The emission spectra plotted in Figure 2.3(b) were calculated using the procedure just described. Equation (2.6) can also be used to compute the total radiated power, by integrating  $P_{tot}(\nu)$  over all frequencies. The red squares in Figure 2.4(a) and Figure 2.4(b)

correspond to the total power per unit sample-area associated with the fundamental harmonic of the output radiation [e.g., the lower-frequency peak of Figure 2.3(b)], plotted as a function of corrugation period  $\Lambda$  and amplitude  $A$ , respectively. In these calculations I use a reasonably large electron density  $N$  of  $5 \times 10^{12} \text{ cm}^{-2}$ , which is well within the range of experimentally accessible values based on capacitive doping. The temperature used to compute the distribution functions was taken to be 300 K. Finally, for the effective drift velocity  $\mu E$  I used a value of  $2 \times 10^7 \text{ cm/s}$ , based on a recent measurement of saturation velocity in graphene at a carrier density of a few  $10^{12} \text{ cm}^{-2}$  at room temperature (Dorgan, Bae, and Pop 2010). If I assume a relatively small sample area of  $100 \times 100 \text{ }\mu\text{m}^2$ , which can be readily produced using epitaxial techniques or chemical vapor deposition, the plots of Figure 2.4 indicate that power levels of several ten nanoWatts can be obtained, which are already appreciable for this frequency range. In fact, high-quality graphene samples with linear dimensions of several millimeters can now be synthesized, e.g., see (Ren et al. 2012), in which case very large spontaneous emission powers approaching a milliWatt become feasible. In this respect it is important to note that the radiation mechanism described in this work is not affected by capacitive or transit-time effects, which would otherwise limit the usable device area as in the case of other THz sources such as photomixers. Figure 2.4(a) also shows that the output power of corrugated graphene increases monotonically with decreasing corrugation period, which is due to the resulting increase in the curvature of the carrier trajectories. Furthermore, as illustrated in Figure 2.4(b), for fixed period there is an optimal amplitude that maximizes the (fundamental-harmonic) output power. At larger amplitudes, the higher-order harmonics (not included in these plots) are amplified

instead at the expense of the lower-frequency peak. I also note that the power levels plotted in Figure 2.4 are of the same order of magnitude, but consistently smaller, than predictions based on the approximate formula of equation (2.2).

From a technological standpoint, an important property that emerges from the two traces of Figure 2.4(a) is the increase in output power with increasing emission frequency. As a result, the radiation mechanism described in this chapter may allow extending the frequency range of existing room-temperature THz sources such as microwave frequency multipliers and photomixers, whose output power near 1 THz can reach a few microWatt but then rapidly scales down with increasing frequency (Lee and Wanke 2007). Furthermore, cyclotron-like radiation in corrugated graphene can also in principle be used to provide stimulated emission and optical gain for the development of graphene-based THz lasers. Specifically, radiation propagating in the direction of the corrugation can produce a bunching of the electron beam (via a resonant electromagnetic interaction), leading to amplification and coherent light emission, as in the case of traditional free-electron lasers (Marshall 1985). Similar laser sources can therefore be envisioned based on corrugated graphene structures, combined with an optical cavity where the emitted light is reflected back and forth in the direction of the applied voltage. For a comparison with existing THz quantum cascade lasers, I note that at cryogenic temperatures the total spontaneous emission power of their active materials (in the absence of optical feedback leading to stimulated emission) is also a few ten nW for sample areas of order  $100 \times 100 \mu\text{m}^2$  (Xu, Hu, and Melloch 1997; Rochat et al. 1998; Köhler et al. 2002). However, as the temperature is increased, their radiative efficiency rapidly decreases due to phonon-assisted

nonradiative transitions between the active subbands (Williams 2007), so that no detectable radiation is produced at room temperature. In the corrugated graphene emitters considered in this work, increasing the temperature mainly leads to a decrease in the maximum achievable drift velocity  $\mu E$  (an effect that can be quite modest as shown in (Dorgan, Bae, and Pop 2010)), and to enhanced collision broadening of the radiation spectra. As shown in Figure 2.3(b), the latter effect can also be relatively weak in high-quality graphene samples (particularly when deposited on hBN), which feature room-temperature mean free paths  $d$  of several hundred nanometers. As a result, if graphene-based THz “free-electron” lasers can be developed, they may potentially allow for room temperature operation.

### **2.3 Sinusoidal grating fabrication and corrugated-graphene strain analysis**

A key ingredient of the proposed cyclotron-like THz radiators is a nanoscale grating with highly sinusoidal surface corrugation and minimal sidewall roughness, to allow for the required conformal adhesion of the overlaying graphene sheet. In order to fabricate such gratings, I have developed the process illustrated schematically in Figure 2.6. First, a periodic pattern of properly oriented chromium lines is formed on the top surface of an n-type  $\langle 100 \rangle$  Si substrate, using electron beam lithography (EBL) with a PMMA resist, followed by metal evaporation and liftoff [Figure 2.6(a) – (d)]. This pattern is then used as a mask for the wet etch of Si in potassium hydroxide (KOH), which provides a highly orientation-dependent etch rate (400 times faster along the  $\langle 100 \rangle$  crystal directions compared to  $\langle 111 \rangle$ ) [Figure 2.6(e)]. As a result, a periodic pattern of trapezoidal ridges with  $\langle 111 \rangle$ -oriented sidewalls is produced after the Cr lines removal, as shown

schematically in Figure 2.6(f). AFM images of the resulting surface morphology are presented in Figure 2.7(a), for the case of a grating with period  $\Lambda = 400$  nm [giving  $f_{\text{rad}} = 2.5$  THz based on equation (2.1)] and peak-to-peak depth  $2A = 90$  nm.

Next, the patterned Si samples are annealed in a dry thermal oxide furnace at  $1100^\circ\text{C}$  for around 5 hours to produce a conformal silicon dioxide coating of the desired thickness ( $\sim 300$  nm) on their top surface, as shown schematically in Figure 2.6(g). The purpose of this  $\text{SiO}_2$  layer is to enable visualization of the subsequently deposited graphene sheets under an optical microscope, and to electrically insulate these sheets from the conducting Si substrate. Extensive characterization of the oxidized samples (including AFM measurements before and after a buffered oxide etch to selectively remove the  $\text{SiO}_2$ ) reveals that the buried Si/ $\text{SiO}_2$  interface features a much smoother, nearly sinusoidal morphology compared to the trapezoidal shape of the sample top surface. To illustrate, in Figure 2.7(b) and (c) I show AFM images measured with the same sample of Figure 2.7(a), after oxidation and subsequent  $\text{SiO}_2$  etch. A highly uniform sinusoidal pattern with sidewall roughness of less than 1 nm is observed in these images. This highly desirable smoothing effect is attributed to different oxidation rates near the sharp corners of the Si grating compared to the flat regions. A similar sinusoidal shape can be produced in the sample top surface with a second oxidation step after removal of the original  $\text{SiO}_2$  layer [Figure 2.6(h) – (i)].

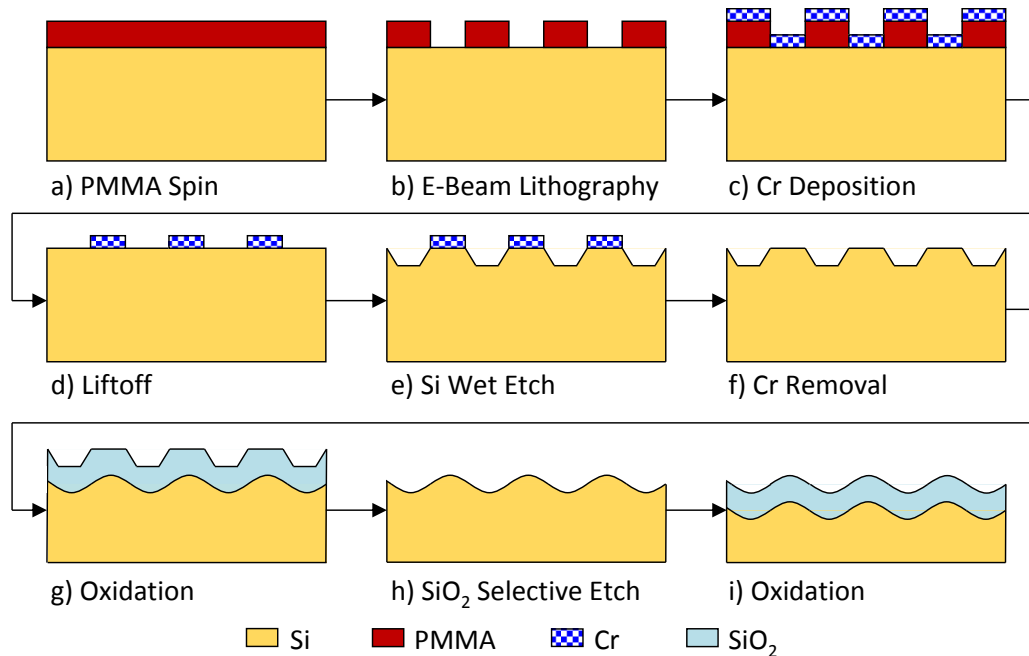


**Figure 2.6 Schematic process flow for the fabrication of Si/SiO<sub>2</sub> nanoscale sinusoidal gratings.**

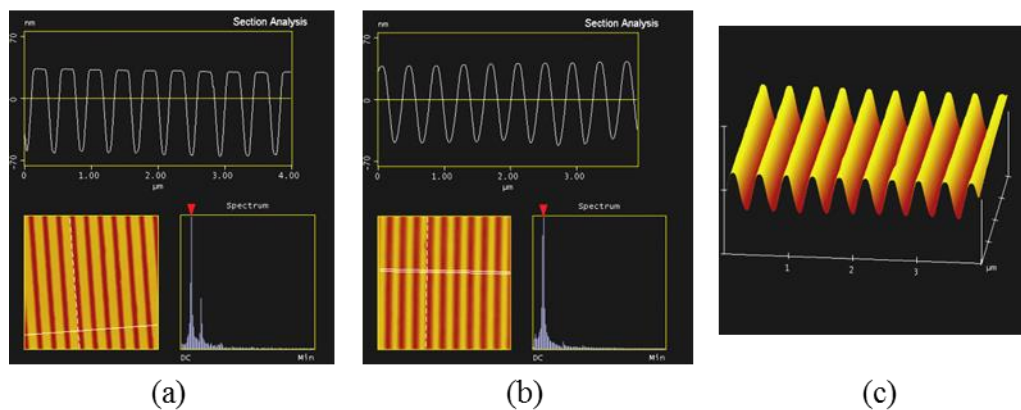


**Figure 2.7 AFM images of gratings fabricated on a Si substrate: (a) after a wet etch in KOH; (b) and (c) after a subsequent oxidation step followed by a buffered oxide etch to selectively remove the SiO<sub>2</sub> layer. In (a) and (b), the bottom left panel contains a plan-view surface-morphology image; a cross-sectional line scan is shown in the top panel, with its Fourier spectrum plotted in the bottom right panel.**

Regarding the grating period  $\Lambda$ , sub-micron values are needed in order to obtain radiation frequencies  $f_{rad}$  above 1 THz as indicated in equation (2.1). Furthermore, as discussed above, the smaller the period, the larger the emitted power and the smaller the broadening of the radiation spectrum due to carrier collisions. At the same time, gratings with larger period are generally easier to fabricate and can perhaps be expected to more readily allow for conformal adhesion of the overlaying graphene sheets. In my initial work, high-quality gratings with a period of 400 nm have been developed reproducibly, as illustrated in Figure 2.7.

A procedure for transferring mechanically exfoliated graphene sheets on these gratings has also been developed by my collaborator Xuanye Wang in Professor Swan's group. Mechanically exfoliated graphene is employed in this work because of its superior electrical properties compared to epitaxially grown samples. However, given the small dimensions of typical exfoliated flakes and of nanopatterned gratings (a few ten microns), an aligned transfer procedure is required that allows placing an exfoliated sheet of graphene on a target pattern with an accuracy of a few microns.

In the procedure developed by Xuanye Wang, graphene is first exfoliated mechanically on a Si substrate that was previously coated with a 90-nm-thick film of the water-soluble polymer polyvinyl-pyrrolidone (PVP) followed by a 200-nm-thick layer of PMMA. The overall optical thickness of this polymeric bilayer is such that single-layer graphene flakes on the PMMA top surface can be readily identified with an optical microscope based on interferometric contrast. Next, the PVP film is dissolved in water to produce a free-standing PMMA membrane supporting the exfoliated flakes. This

membrane is transferred onto a thicker polymer (PDMS) film on a glass side, which is then mounted upside down on a translational stage under a microscope. A single-layer graphene flake of suitable dimensions is identified through the transparent glass/PDMS/PMMA stack. The target substrate is then placed under the same microscope, and the translational stage is used to align and press the selected graphene flake onto the grating. Finally, the sample is heated beyond the PMMA glass transition temperature ( $\sim 110$  °C) to enhance graphene adhesion to the substrate, while the PDMS film is peeled off. Because the deposition step takes place under a microscope, an alignment accuracy of a few microns is readily achieved.

In order to demonstrate THz cyclotron-like radiation from graphene, the charge carriers in the corrugated sheet must travel for at least a few periods of the gratings without collisions. Unfortunately, however, all exfoliated graphene samples transferred on the gratings under study have shown relatively low mobilities corresponding to mean free paths well below the grating period (400nm), due to cleanliness and mechanical-strain issues. Possible graphene transfer methods that may be able to address this problem include the use of hBN-graphene-hBN heterostructures deposited on corrugated gratings, and the formation of suspended corrugated graphene by self-assembly. These processes have not been tried in the course of this thesis work. Instead, samples based on the fabrication process described above have been used by Xuanye Wang to study strain redistribution in corrugated graphene including clamping, sliding and friction between graphene and the SiO<sub>2</sub> surface (X. Wang et al. 2015). These issues are important for the future development of higher-quality corrugated graphene samples, and more in general for strain engineering

applications.

The graphene strain study starts from a detailed analysis of the surface morphology. An optical image, Raman 2D-band peak-center map, and AFM data of a corrugated graphene sample are shown in Figure 2.8(a), (b), and (c), respectively. The lighter-blue areas in the microscope image correspond to graphene with an average sinusoidal corrugation of 20 nm as determined from AFM, which is smaller than what was measured with the same grating before graphene deposition (55 nm). Based on this corrugation level, we can estimate an average geometrical strain  $\varepsilon$  equal to 0.62%. On the other hand, the dark lines in Figure 2.8(a) represent partially suspended graphene regions with a corrugation depth of only 5nm, corresponding to a lower estimated average strain of 0.15%. In contrast, the 2D Raman mapping of Figure 2.8(b) shows that the strain is less than 0.5% in the highly conformed graphene, and more than 0.15% in the low conformed. In other words, the strain values from the 2D Raman map feature smaller variance compared to the geometrical AFM estimates. This observation indicates partial sliding of the graphene over the grating causing a redistribution and homogenization of the induced strain.

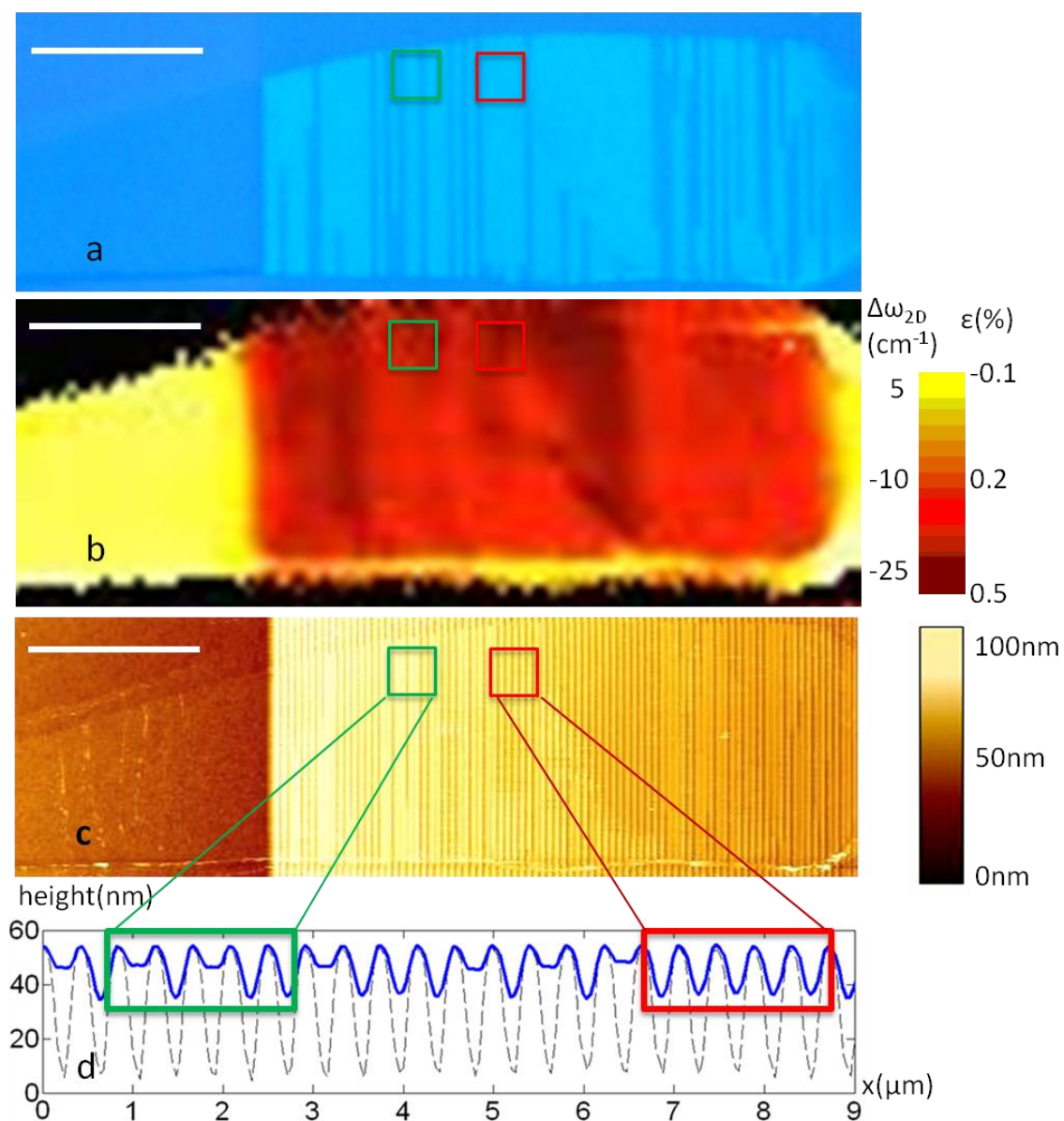


**Figure 2.8** Graphene on a silicon dioxide grating. Scale bar: 10 $\mu$ m. (a) Optical image. (b) Map of the Raman 2D-band peak center. (c) AFM height map. (d) AFM line profile. The red and green boxes correspond to the same regions in (a), (b) and (c).

To investigate the strain in corrugated graphene in more detail, we observe the Raman G-band peak position and linewidth along the scan line shown in Figure 2.9(a), measured with the Raman laser polarized perpendicular to the grating lines. These results can be separated in three regions. The first area is on the left of the grating, and corresponds to graphene on a flat SiO<sub>2</sub> region. In this region, the G peak position is larger than 1582 cm<sup>-1</sup> and the average linewidth is relatively small (around 8.58 cm<sup>-1</sup>). The corresponding strain  $\epsilon$  is negative, indicating compression of the graphene sheet caused by heating during the transfer process. Inside the grating, the green data represent the less conformed graphene regions with G peak positions between 1567-1572 cm<sup>-1</sup> and G linewidth around 9.12 cm<sup>-1</sup>. Finally, the more highly conformed graphene areas are labeled by the red data. Between the flat SiO<sub>2</sub> and the grating, there is a wide transition region where the G peak position rapidly downshifts. These results demonstrate that the van der Waals forces causing friction between SiO<sub>2</sub> and graphene are not strong enough to fully clamp the graphene on the flat area, and therefore the graphene close to the grating can slide to redistribute its strain.

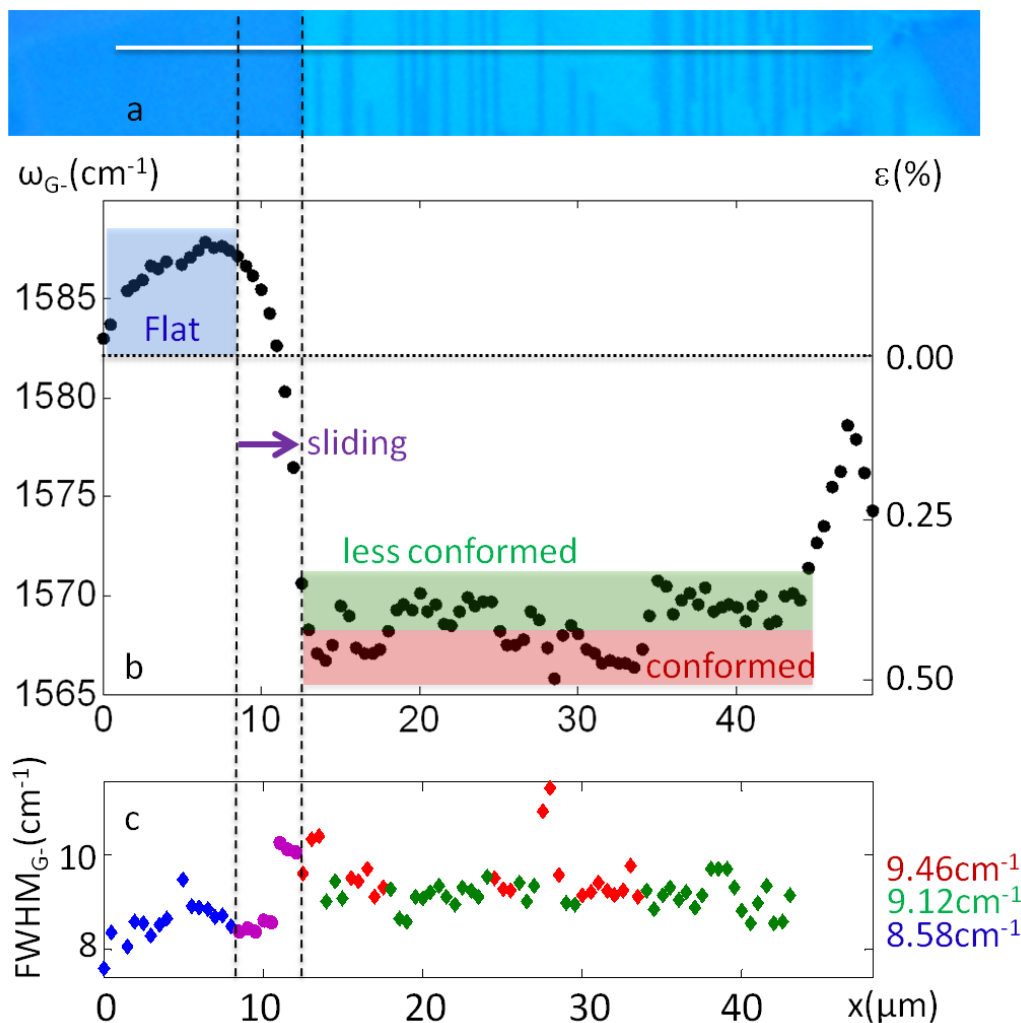


**Figure 2.9** Line scan of the Raman G band. Top through bottom: optical image of graphene, G peak center versus position, and G linewidth versus position. The blue, green and red boxes correspond to graphene on the flat surface (under compression), and on the grating under medium strain and high strain, respectively.

Finally, the friction  $f$  between the  $\text{SiO}_2$  substrate and graphene is studied as a function of strain. The estimated friction (i.e., the force to clamp graphene on the substrate) is found to be inversely proportional to strain for both bilayer and single layer graphene, as indicated in Figure 2.10. The decrease in friction with increasing strain can be explained

as a result of decreasing surface contact area. For zero strain, graphene can conform very well to the underlying substrate surface morphology. Strain however, smooths out the graphene sheet and, hence, reduces the contact area. Such strain dependence of the friction clamping could be an issue for strain engineering devices, although it could be reduced with flatter substrate surface. For the application of interest in this work (i.e., cyclotron-like emission from corrugated graphene), zero strain is desired to obtain maximal conformation and avoid strain-induced structural damage.

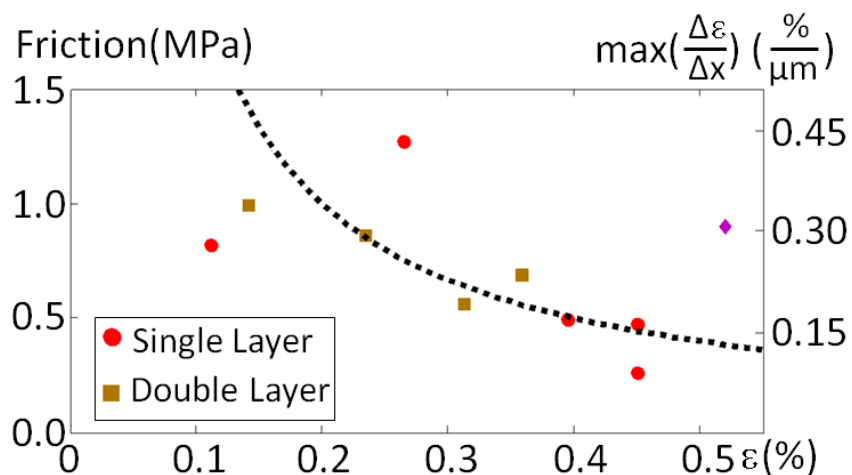


**Figure 2.10 Friction versus strain. There is a clear indication of reduced friction with increasing uniaxial strain. The corresponding value of  $\Delta\epsilon/\mu\text{m}$  versus strain is marked on the right hand side. The purple diamond data point on the right shows the maximum strain variation predicted from the linewidth broadening calculation.**

### 3 GRAPHENE ON NANOSCALE GRATINGS FOR THE GENERATION OF TERAHERTZ SMITH-PURCELL RADIATION

#### 3.1 Proposed radiation mechanism

An alternative electron-beam radiation mechanism involves the use of charges under uniform rectilinear motion in the presence of a periodically modulated dielectric environment. This effect was discovered by Smith and Purcell in 1953, through the measurement of visible light emission from a high-energy electron beam traveling near a metallic grating in vacuum (S. J. Smith and Purcell 1953). Its observation was initially explained in terms of cyclotron radiation from the image charges induced in the metal by the electron beam, which undergo periodic angular motion due to the periodically corrugated metal surface. More rigorously, the underlying radiation mechanism can be ascribed to the evanescent electromagnetic fields associated with the actual moving charges, which, under the proper conditions, can be diffractively scattered by the grating into radiation (van den Berg and Tan 1974). The resulting emission spectrum consists of several peaks whose frequencies  $\omega_{\mathbf{g}}$  are related to the reciprocal lattice vectors  $\mathbf{g}$  of the grating array (which define the corresponding orders of diffraction). In the nonrelativistic limit, where the carrier velocity  $v$  is much smaller than the speed of light  $c$ , this relationship is simply  $\omega_{\mathbf{g}} = \mathbf{v} \cdot \mathbf{g}$ . The use of this mechanism for the generation of microwaves in vacuum-based devices (orotrons) is already well established (Bratman et al. 2010). The measurement of Smith-Purcell (SP) radiation at THz frequencies in condensed matter has also been reported, based on the two-dimensional electron gas (2DEG) of a GaAs/AlGaAs heterojunction near a periodically corrugated surface (Wirner et al. 1993). However, the

output spectrum of this device was found to be extremely broad and weak, and could only be detected at cryogenic temperatures. More recently, the use of charge domains in Gunn diodes has also been theoretically proposed as a promising approach for the generation of THz SP radiation (D. D. Smith and Belyanin 2011).

As already mentioned, the pursuit of this and similar radiation mechanisms in traditional semiconductors is hindered by several material properties, including limited saturation velocities, low mobilities at room temperature, and broad thermal distribution of carrier velocities (leading to proportionally broad SP emission peaks). By virtue of its exceptional electrical properties, (Novoselov et al. 2004; Novoselov et al. 2005; Zhang et al. 2005; Berger et al. 2006; Castro Neto et al. 2009) graphene provides a natural candidate to overcome these limitations. Specifically, record large room-temperature mobilities above  $1 \times 10^5 \text{ cm}^2/\text{Vs}$  can be obtained with optimized sample geometries, including suspended sheets (Bolotin et al. 2008; Du et al. 2008) or sheets deposited on atomically smooth, highly inert hexagonal boron nitride (hBN) films (Dean et al. 2010; Mayorov et al. 2011; L. Wang et al. 2013). The corresponding mean free paths are on the order of one micron, and values exceeding  $15 \text{ }\mu\text{m}$  have also been measured at cryogenic temperatures (L. Wang et al. 2013). These properties, combined with the truly 2D nature of the graphene electron gas, are ideally suited to the demonstration of electron-beam radiation mechanisms at THz frequencies in compact solid-state systems.

### 3.2 Simulation results

In order to evaluate the potential of this approach, I have investigated numerically the specific device geometry shown in Figure 3.1(a) (Tantiwanichapan et al. 2014), where a single-layer sheet of graphene is deposited over a 2D hole array in a solid substrate (e.g., a SiO<sub>2</sub> film on a silicon). In practice, an ultrathin hBN liner could also be inserted under the graphene sheet to increase its carrier mobility. The holes are arranged on a triangular lattice with period  $\Lambda$  and have cylindrical shape with depth  $H$  and diameter  $D$  fixed at 200 nm and  $0.6\Lambda$ , respectively. An external voltage is applied between the source and drain contacts, producing an electric field  $\hat{x}E$  in the direction of a line of holes. The use of a 2D array as opposed to a 1D grating (as in the original experiment by Smith and Purcell (S. J. Smith and Purcell 1953)) is motivated by a fundamental difference between the electron gas in graphene and the typical electron beam of a vacuum-based device. In the latter case, all electrons can be made to travel roughly along the same direction (to within a small divergence angle). In contrast, in a semiconductor 2DEG the carrier distribution in reciprocal space is such that, even in the presence of a bias voltage, there are carriers traveling along all possible directions on the 2DEG plane. In general, efficient SP emission can only be excited by carriers traveling along the directions of the array reciprocal lattice vectors  $\mathbf{g}$ . Therefore, a larger fraction of the 2DEG carriers can contribute to the SP emission if a 2D array (with its multitude of reciprocal lattice vectors along several different directions) is employed.

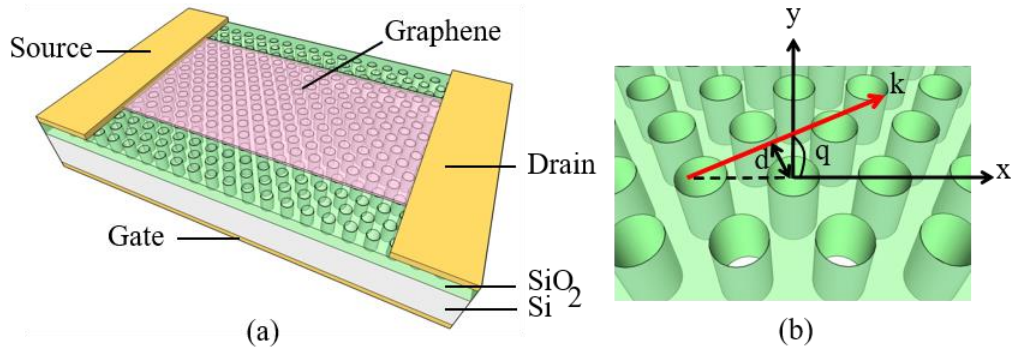


**Figure 3.1 (a) Schematic illustration of the sample geometry investigated in this chapter. (b) Close-up image of the hole array of (a), with a pictorial definition of some of the key parameters used in the simulations.**

N-type samples are considered in these simulations (e.g., produced via electrostatic doping with a positive back-gate voltage), although the same results also apply to p-doped graphene. Once again, the starting point of our analysis is the current density  $\mathbf{J}_{\mathbf{k}} = -q\mathbf{v}_{\mathbf{k}}\delta(\mathbf{r} - \mathbf{v}_{\mathbf{k}}t)$  carried by a single conduction-band electron in between consecutive collisions, where  $\mathbf{k}$  is the electronic wavevector (measured from the nearest Dirac point) and  $\mathbf{v}_{\mathbf{k}} = v_F\hat{\mathbf{k}}$ . Using Fourier analysis,  $\mathbf{J}_{\mathbf{k}}$  can be decomposed in a superposition of harmonic waves at all frequencies  $\omega$ , each having wavevector component along the direction of motion given by  $q_{||} = \omega/v_F$ . Based on the linearity of Maxwell equations, the electromagnetic fields produced by this current density can be decomposed in exactly the same fashion. Since  $\omega/v_F$  is much larger than the total wavenumber  $q_0 = \omega/c$ , the wavevector component perpendicular to the graphene plane  $q_z$  is imaginary for each term in the superposition (i.e., the electromagnetic fields produced by the electron are evanescent, as one would expect for an electron in uniform rectilinear motion). In the

geometry under study, diffractive scattering by the array can then shift the in-plane wavevector of each harmonic component of these electromagnetic fields by any grating vector  $\mathbf{g}$ , to produce a multitude of diffracted waves. In particular, the harmonic components of frequencies near  $\omega_{\mathbf{g}} = \mathbf{v}_{\mathbf{k}} \cdot \mathbf{g}$  are correspondingly scattered into radiative waves, i.e., their shifted in-plane wavevectors become smaller than  $q_0$  so that the out-of-plane components  $q_z$  are real and radiation away from the sample is produced. The argument just presented provides a rigorous explanation of the SP radiation mechanism, and can be used for the numerical evaluation of the output light under suitable assumptions on the grating geometry (van den Berg and Tan 1974). Instead, here, I again use the numerical simulation tool based on the FDTD method, which allows for an accurate solution under very general conditions. As in the work of the previous chapter, these simulations rely on the formal equivalence between current and polarization density. The effect of electronic collisions can then be directly included in the calculations by setting the length of the equivalent dipole distribution equal to the electron mean free path between consecutive collisions  $d$ . With this arrangement, the evanescent electromagnetic fields produced by the simulated dipole distribution are only coherently scattered by a finite number of holes in the array proportional to  $d/\Lambda$ , as in the case of an electron undergoing recurrent collisions in a realistic sample. Specifically, only the holes within the evanescent tail of these electromagnetic fields (i.e., within a distance on the order of  $v_F/\omega_{\hat{\mathbf{k}},\mathbf{g}}$  from the simulated dipole chain) can participate in the SP radiation process.

Using this procedure, I find that the emission spectrum of each electron indeed consists of a series of peak  $P_{\hat{\mathbf{k}},\mathbf{g}}(\omega)$  at the SP frequencies  $\omega_{\mathbf{g}} = \mathbf{v}_{\mathbf{k}} \cdot \mathbf{g} = v_F \hat{\mathbf{k}} \cdot \mathbf{g}$  for any

reciprocal lattice vector  $\mathbf{g}$ . These peaks can be clearly resolved in the FDTD spectra provided that the ratio  $d/\Lambda$  is sufficiently large (i.e., larger than about 3); therefore, only structures that satisfy this condition are considered in the following. The larger  $d/\Lambda$  the narrower the peak linewidths, as illustrated in Figure 3.2, where I show representative single-electron emission spectra computed with a mean free path of 4  $\mu\text{m}$ , 1  $\mu\text{m}$ , and 400 nm. In each case, the array period is 100 nm and the angle  $\theta_k$  [as defined in Figure 3.1(b)] is  $0^\circ$  in Figure 3.2(a) and  $10^\circ$  in Figure 3.2(b). Importantly, all three values of  $d$  considered in this figure are experimentally accessible. Specifically, mean free paths of about 400 nm and 1  $\mu\text{m}$  have been reported at room temperature with graphene samples on oxidized Si substrates (Novoselov et al. 2004) and on ultrathin h-BN films (Mayorov et al. 2011; L. Wang et al. 2013), respectively. The higher value of 4  $\mu\text{m}$  (equal to the full length of the simulated array) has been measured at about liquid-nitrogen temperature with graphene on h-BN (L. Wang et al. 2013). It is also apparent from Figure 3.2 that the center frequency of each emission peak is shifted with decreasing mean free path, a behavior that is often associated with collision broadening (Peach 1981).

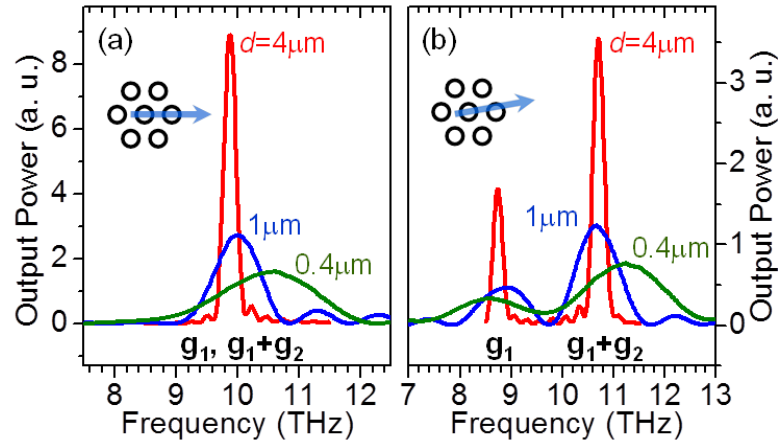


**Figure 3.2** Single-electron radiation spectra for different values of the mean free path  $d$ , produced by an electron traveling at an angle  $\theta_k = 0^\circ$  (a) and  $10^\circ$  (b) with respect to the  $x$  direction in the sample geometry of Figure 3.1. The array period is 100 nm. The arrows in the insets show the direction of the electron velocity.

The same FDTD simulations can also be used to determine the far-field radiation properties of SP emission in graphene. To illustrate, Figure 3.3 shows the radiation pattern in the plane of the substrate produced by an electron traveling along  $\theta_k = 0$  for  $\Lambda = 100$  nm and  $d = 1 \mu\text{m}$ . The corresponding emission in the air above is significantly weaker and therefore is not considered. The key observation here is that most of the light is radiated in an oblique direction with respect to the surface normal, whose projection on the graphene plane is antiparallel to the electronic motion. The radiation pattern of Figure 3.3 was computed at the frequency of peak emission of the electron under study. As the frequency is detuned from this value, the emission angle changes (consistent with the diffractive nature of the underlying mechanism), while the intensity decreases. These results are qualitatively consistent with the far-field radiation properties of SP emission from high-energy electron beams in vacuum (van den Berg and Tan 1974).

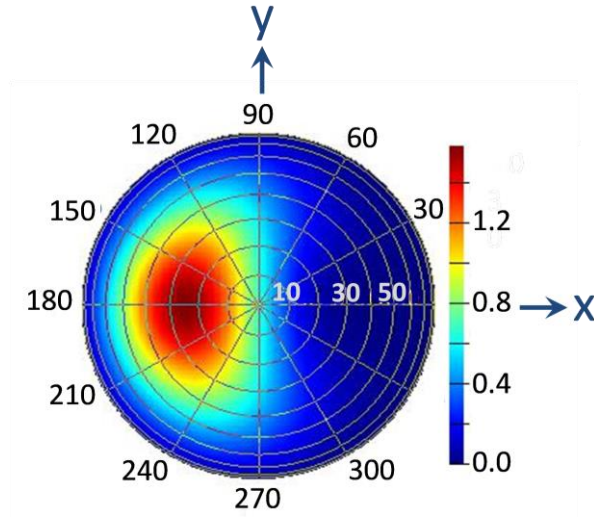


**Figure 3.3** Far-field radiation pattern in the array substrate produced by an electron traveling in the  $x$  direction, for  $\Lambda = 100$  nm and  $d = 1$   $\mu$ m. The  $x$ - $y$  coordinate system is the same as in Figure 3.1(b)

The total radiation output of the sample geometry under study is finally obtained by summing the single-electron contributions over all values of the wavevector  $\mathbf{k}$ , properly weighted by the electronic distribution function  $f_{\mathbf{k}}$ . Specifically, the output power spectrum is computed as follows:

$$P_{\text{tot}}(\omega) = 4 \sum_{\mathbf{k}, \mathbf{g}} P_{\mathbf{k}, \mathbf{g}}(\omega) f_{\mathbf{k}} (1 - f_{\mathbf{k} - \mathbf{g}}) \quad (3.1)$$

where the factor of 4 accounts for the spin and valley degeneracies,  $f_{\mathbf{k}}$  is the probability that the electronic initial state is occupied, and  $1 - f_{\mathbf{k} - \mathbf{g}}$  is the probability that the corresponding final state after photon emission is empty. The assertion that this final state has wavevector  $\mathbf{k} - \mathbf{g}$  follows from the requirement of conservation of quasi-momentum. Furthermore, if  $\mathbf{g}$  is small relative to  $\mathbf{k}$  (which is generally the case), the energy difference between the graphene Bloch states of wavevectors  $\mathbf{k}$  and  $\mathbf{k} - \mathbf{g}$  can be readily shown to be equal to

$\hbar\omega_{\mathbf{k},\mathbf{g}} = \hbar v_F \hat{\mathbf{k}} \cdot \mathbf{g}$  (i.e., the emitted photon energy) so that conservation of energy is also automatically satisfied in equation (3.1).

In order to compute  $P_{\text{tot}}(\omega)$  with a practicable number of FDTD runs, the following procedure is followed. First, the FDTD simulations just described are carried out for a few values of the angle  $\theta_{\mathbf{k}}$  (i.e., the direction of  $\mathbf{k}$ ), namely  $0^\circ$ ,  $10^\circ$ ,  $20^\circ$ , and  $30^\circ$ . From these simulation results, the center frequency, full width at half maximum (FWHM), and integrated power of the corresponding single-electron emission peaks  $P_{\mathbf{k},\mathbf{g}}(\omega)$  are determined. Next, the values of the same parameters for all other angles  $\theta_{\mathbf{k}}$  are extrapolated using a polynomial fit and symmetry considerations. The single-electron spectra  $P_{\mathbf{k},\mathbf{g}}(\omega)$  in equation (3.1) for all values of  $\theta_{\mathbf{k}}$  are then approximated with a Gaussian peak having the correct center frequency, FWHM, and integrated power (as determined with this fitting procedure). The choice of a Gaussian function is consistent with the shape of the FDTD single-electron emission peaks, and does not in any case significantly affect the shape of  $P_{\text{tot}}(\omega)$ . An additional complication is that the single-electron integrated output powers also depend on the displacement parameter  $\delta$  defined in Figure 1.1(b) [i.e., the distance from the electron trajectory to the center of a nearby reference hole]. Therefore, for each simulated value of  $\theta_{\mathbf{k}}$ , different FDTD runs with representative values of  $\delta$  are also carried out to find the average single-electron output power. Finally, to determine the occupation probabilities  $f_{\mathbf{k}}$ , I use once again a semiclassical model of carrier dynamics, where an externally applied electric field  $\hat{\mathbf{x}}E$  has the effect of simply displacing the equilibrium Fermi-Dirac distribution function as a whole

by the amount  $\delta\mathbf{k} = -\hat{\mathbf{x}}k v_d/v_F$ , where  $v_d = \mu E$  is the drift velocity and  $\mu$  is the mobility (Castro Neto et al. 2009).

Figure 3.4 shows the radiation spectra  $P_{\text{tot}}(\omega)$  of three structures of different period between 100 to 300 nm, computed with a mean free path of 1  $\mu\text{m}$ . A reasonably large carrier density of  $5 \times 10^{12} \text{ cm}^{-2}$  is used in these calculations, at a temperature of 300 K. For  $v_d$  I use the experimental saturation value of  $2 \times 10^7 \text{ cm/s}$ , obtained from the high-field current-voltage characteristics of a graphene sample with carrier density of a few  $10^{12} \text{ cm}^{-2}$  at room temperature (Dorgan, Bae, and Pop 2010). As illustrated in Figure 3.2, these radiation spectra  $P_{\text{tot}}(\omega)$  are derived from two  $\theta_{\mathbf{k}}$ -dependent emission lines associated with diffraction by  $\mathbf{g}_1$  and  $\mathbf{g}_1 + \mathbf{g}_2$ . The latter feature is strongest for  $\theta_{\mathbf{k}} = 30^\circ$  (and equivalent directions), whereas for  $\theta_{\mathbf{k}} = 0^\circ$  the two lines are degenerate. In the 100-nm structure of Figure 3.4, the two emission peaks derived from these two lines are sufficiently close to each other in frequency that they overlap (despite their relatively large quality factor), leading to particularly high peak power. In contrast, in the other structures of Figure 3.4 these two peaks are clearly resolved.

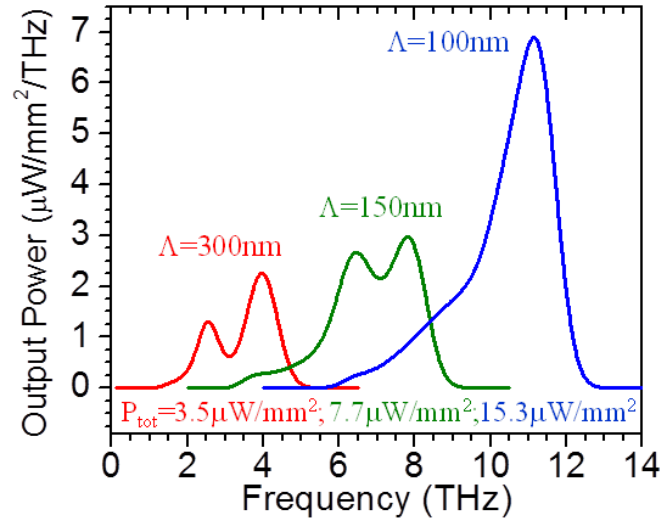


**Figure 3.4** Emission spectra of three graphene SP samples of different period  $\Lambda$ , computed with a mean free path  $d$  of  $1 \mu\text{m}$ . The total output power per unit area of each structure, integrated over all frequencies, is also listed in the inset.

The total output powers per unit area of the structures of Figure 3.4, integrated over all frequencies, are listed in the inset. The key conclusion that emerges from these data is that technologically significant power levels of several  $\mu\text{W}/\text{mm}^2$  can be obtained at geometrically tunable THz frequencies, similar to the cyclotron-like radiation mechanism investigated in chapter 2. Importantly, these high power levels are again produced at frequencies of several THz (in fact, the smaller the array period, the higher the emission frequency and at the same time the larger the output power), contrary to the case of traditional microwave oscillators which are generally limited to frequencies below  $\sim 1$  THz (Lee and Wanke 2007). Combined with the inherent design simplicity and array scalability of the geometry of Figure 3.1, this property makes the SP effect in graphene an attractive candidate to extend the frequency range of existing room-temperature THz sources based

on compact solid-state systems. Once again, these favorable results are a direct consequence of the high mobility and large carrier velocity of single-layer graphene.

### 3.3 Sample fabrication

For the demonstration of Smith-Purcell THz emission from graphene, two-dimensional arrays are preferable as explained in the previous section. The sample fabrication process has been developed, involving a square periodic array of dielectric holes on SiO<sub>2</sub>/Si substrates. The first step of this process is the formation of a gate contact on the doped-Si substrate, using photolithography and a wet etch in buffer oxide etch (BOE) for 5 minutes. Next, Cr and Au are deposited on doped-Si substrate with 5-nm and 60-nm thickness respectively, using electron-beam evaporation and liftoff, as shown in Figure 3.5(c) and (d). 2D hole arrays in SiO<sub>2</sub> are then patterned by electron beam lithography (EBL) combined with reactive ion etching (RIE), as illustrated in Figure 3.5(e) and (f). The RIE parameters used in this process include 200-watts electrical power with 5-sccm oxygen flow and 45-sccm CHF<sub>3</sub> flow under 40-mTorr pressure for 1.5 minutes. Representative SEM and AFM images of a hole array with 100-nm diameter, 20-nm period, and 45-nm depth are shown in Figure 3.6. Highly uniform features with good periodicity can be observed in these images.

Exfoliated graphene sheets encapsulated in thin hBN films (L. Wang et al. 2013) have been transferred on these arrays by Carlos Forsythe, a Ph.D. student working in Professor Cory Dean's group at Columbia University. The transfer process begins with coating a Si substrate with ~1 μm of poly-propylene carbonate (PPC) and transferring a 5-

20 nm thick hBN flake on it. Next, this hBN/PPC film is peeled off manually and placed onto a transparent PDMS stamp. A previously exfoliated graphene sheet and another hBN flake are then picked up sequentially from their initial SiO<sub>2</sub> substrate, using the inverted PDMS/PPC/hBN stamp under a microscope. Next, the resulting stack is transferred onto the hole array again under a microscope. The PDMS film is then released from the glass slide by heating up the substrate to 90°C. Finally, the PPC layer is dissolved with chloroform, leaving only the hBN-graphene-hBN stack on the hole array.

Next, 1D source and drain contacts to the graphene sheet are processed. To that purpose, the top hBN flake is patterned by EBL, followed by etching through the graphene sheet by RIE. With this process, both ends of graphene are exposed to air. A second EBL step is then performed followed by evaporation of Pd/Au with 5/60 nm thickness, to create source and drain metal contacts connecting to the exposed 1D graphene edges (L. Wang et al. 2013). Figure 3.7 presents an optical image of a completed sample based on this fabrication process, with array period of 150 nm.

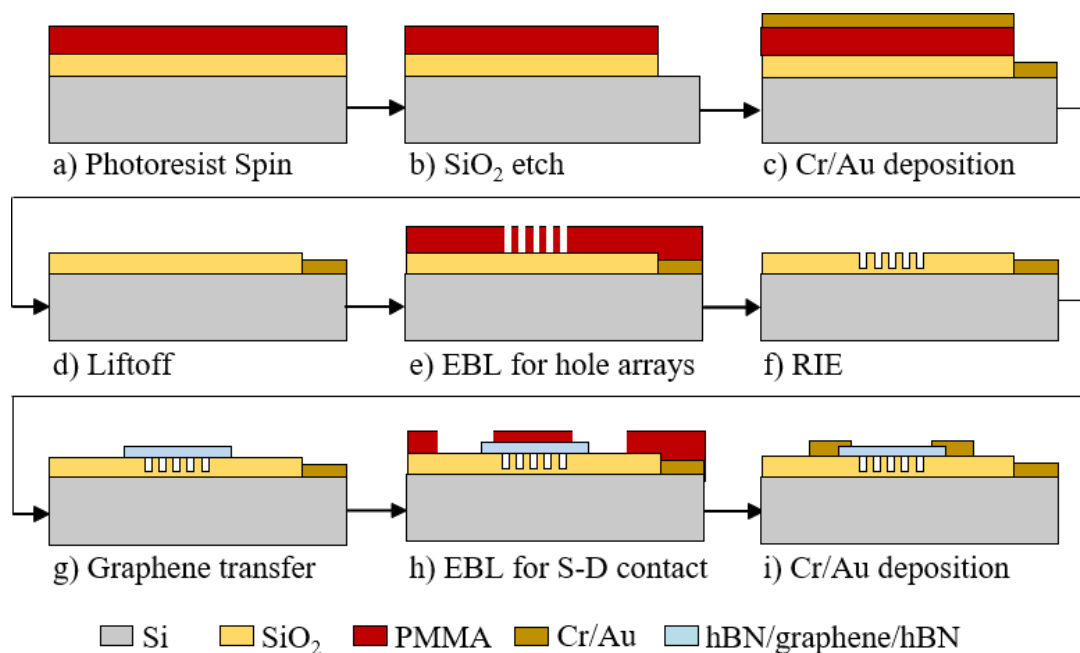


**Figure 3.5 Schematic process flow for the fabrication of samples involving hBN-graphene-hBN heterostructures on 2D hole arrays.**

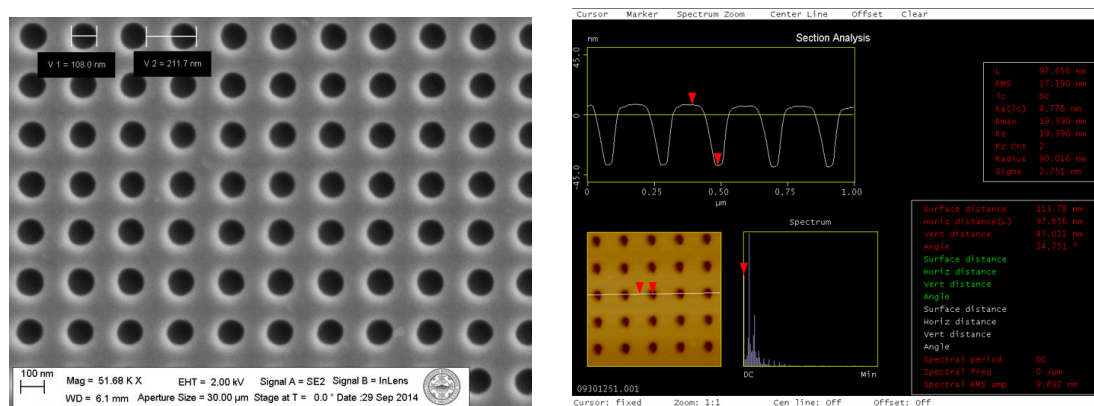


**Figure 3.6 SEM and AFM image of a 2D hole array with 200-nm period and 100-nm hole diameter on an SiO<sub>2</sub>/Si substrate fabricated by EBL, and RIE.**

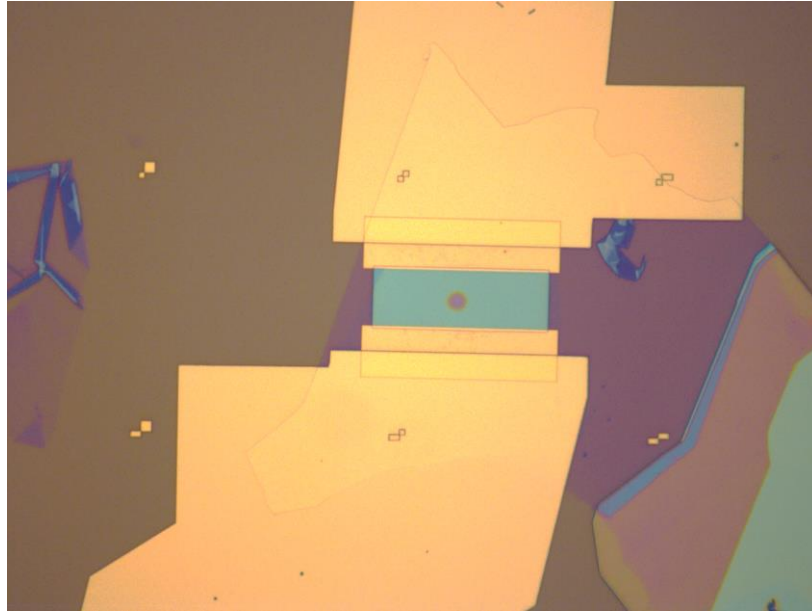


**Figure 3.7 Optical image of an hBN-graphene-hBN stack transferred on top of a hole array (blue areas) with metal contacts (yellow areas).**

### 3.4 Electrical characteristics and electroluminescence measurements

The structural quality of the sample just described (and their suitability to the demonstration of SP emission) can be evaluated from the carrier mobility  $\mu$  and mean free path  $l_m$ , which can be estimated through the measurement of the drain-source resistance versus back-gate voltage  $V_{gs}$ . In these measurements, I supply a fixed AC current  $I_{ds}$  with 70-nA amplitude between the source and drain contacts, and measure the resulting voltage  $V_{ds}$  across the same contacts using a Lock-In Amplifier (LIA). This measurement is repeated for several different values of the back-gate voltage  $V_{gs}$ .

The graphene mobility can be estimated from these data using a standard procedure (Dean et al. 2010; Hwang, Adam, and Sarma 2007). Specifically, first I use equation (1.2)

to convert the gate voltage  $V_{gs}$  to the graphene carrier density  $n$ . Next, the measured drain-source voltage  $V_{ds}$  is used to determine the sheet resistance  $R_s = V_{ds}/I_{ds}$ , from which the conductivity  $\sigma = 1/R_s$  is obtained. Finally, the resulting plot of conductivity versus carrier density is fitted with the following expression (Dean et al. 2010; Hwang, Adam, and Sarma 2007)

$$\sigma = \frac{1}{(q\mu n + \sigma_{min})^{-1} + \rho_s} \quad (3.2)$$

to estimate the mobility  $\mu$ , together with the additional fitting parameters  $\sigma_{min}$  (the minimum conductivity) and  $\rho_s$  (the sheet resistivity due to short range scattering). The solid line in Figure 3.8(a) is the result of this fitting procedure for the hBN-graphene-hBN sample of Figure 3.7 at room temperature, from which a large mobility of about 44,570  $\text{cm}^2/\text{Vs}$  is extrapolated. The mean free path  $l_m$  is proportional to the mobility and to the square root of the carrier density according to the expression

$$l_m = \left(\frac{\hbar}{e}\right)\mu\sqrt{n\pi} \quad (3.3)$$

Figure 3.8(b) shows  $l_m$  based on this equation plotted as a function of  $\mu$  for different values of  $n$ . Using these data, room-temperature mean free path of the sample of Figure 3.7 is found to be approximately 500 nm, which is larger than (but relatively close to) the array period of 150 nm.

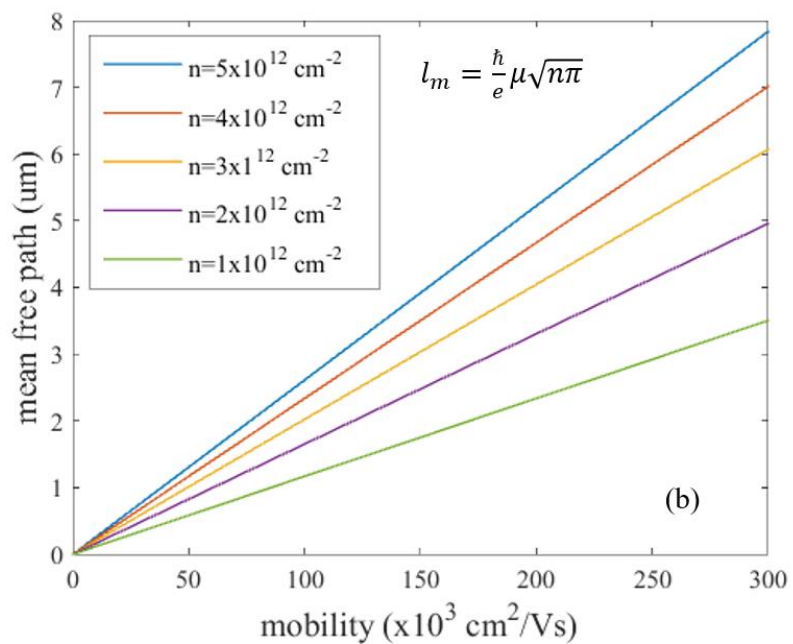
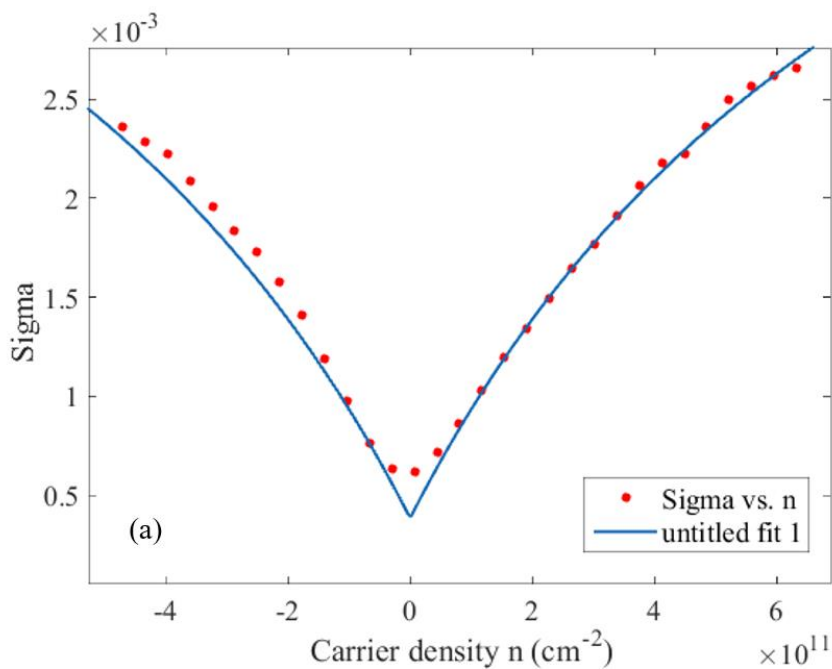


**Figure 3.8 (a) Room-temperature conductivity of the sample of Figure 3.7 vs. carrier density. (b) Mean free path vs. mobility for different values of the carrier density.**

The same measurements are also carried out with the sample at liquid-nitrogen temperature (77 K). Significantly larger values of mobility and mean free path (225,000  $\text{cm}^2/\text{Vs}$  and 2.8  $\mu\text{m}$ , respectively) are correspondingly obtained for  $1 \times 10^{12} \text{ cm}^{-2}$  carrier density. These values suggest that Smith-Purcell radiation can be produced since electrons can travel over considerably longer distances than the hole array period without collisions.

The experimental setup used to measure electroluminescence is shown schematically in Figure 3.9. This setup employs a Fourier transform infrared (FTIR) spectrometer equipped for operation across the entire THz spectrum. The sample is mounted in a continuous-flow cryostat suitably wired to enable the application of a DC gate bias  $V_{\text{gs}}$  and a periodically modulated source-drain voltage  $V_{\text{ds}}$  or current  $I_{\text{ds}}$ . In the measurements, the FTIR interferometer is operated in step-scan mode, and the signal is detected with a liquid-He-cooled Si bolometer followed by a Lock-In Amplifier (LIA) to further improve the measurement sensitivity. Finally, the output signal from the LIA is sent back into the FTIR electronics for Analog to Digital (ADC) conversion and spectral analysis. Based on the bolometer noise properties, THz optical signals in the picowatt range can be detected with this setup.

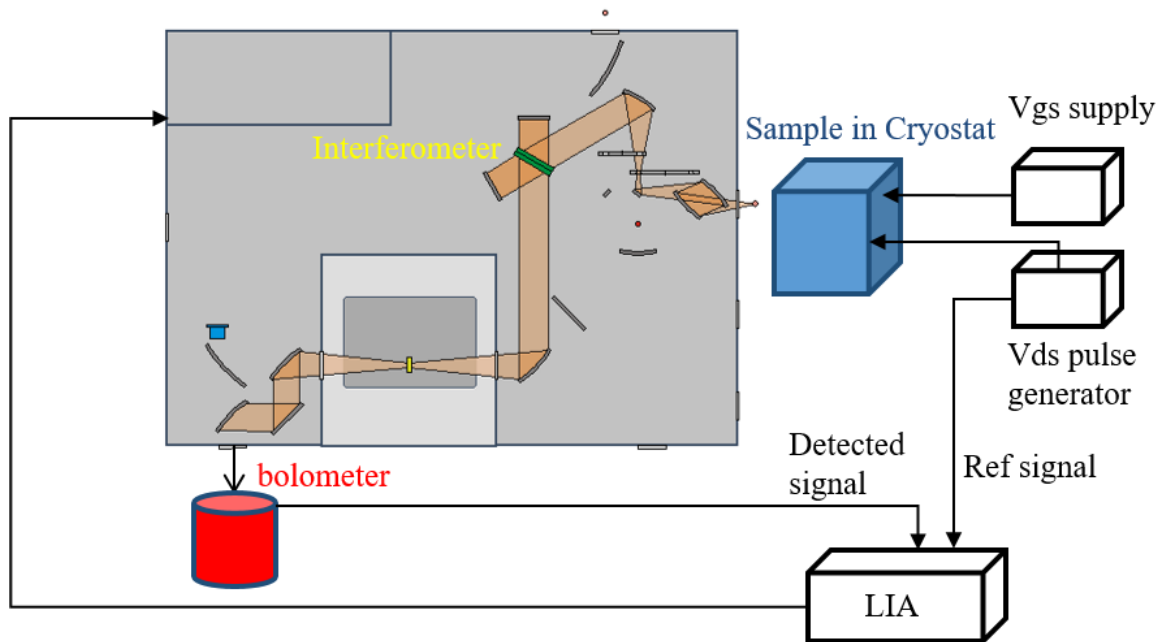


**Figure 3.9 Electroluminescence measurement setup.**

Pronounced emission peaks in the expected frequency range were obtained with the sample of Figure 3.7 at 77 K. Figure 3.10(a) shows representative electroluminescence spectra measured with a fixed source-drain current  $I_{ds} = 24$  mA, for different values of the gate voltage  $V_{gs}$ . A small degree of smoothing was applied to these curves, to remove periodic features due to etalon effects in the bolometer filter. A peak near 8 THz is clearly observed in these plots which is attributed to Smith-Purcell emission, superimposed on a broad pedestal due to blackbody radiation. For the array period of 150 nm of the sample under study, the first-order Smith-Purcell radiation frequency is about 6.7 THz. The shifted emission frequency of the peaks of Figure 3.10(a) can be explained as a result of collision broadening, consistent with the simulation results of Figure 3.2. Figure 3.10(b) shows electroluminescence spectra of the same sample at room temperature, again measured with

$I_{ds} = 24$  mA and different values of  $V_{gs}$ . Compared to the low-temperature data of Figure 3.10(a), the broad blackbody-radiation pedestal is stronger, and no obvious peak attributable to Smith-Purcell emission is observed. This behavior is consistent with the mobility measurements described above. At room temperature, the mean free path is 500 nm, i.e., only about 3 times larger than the array period. In this regime, Smith-Purcell radiation can barely be resolved according to our simulations (as discussed in section 3.2). In contrast, at 77 K the mean free path is over 18 times larger than the period, so that strong Smith-Purcell radiation (only limited by the graphene sheet area of  $30 \times 10 \mu\text{m}^2$ ) is expected.

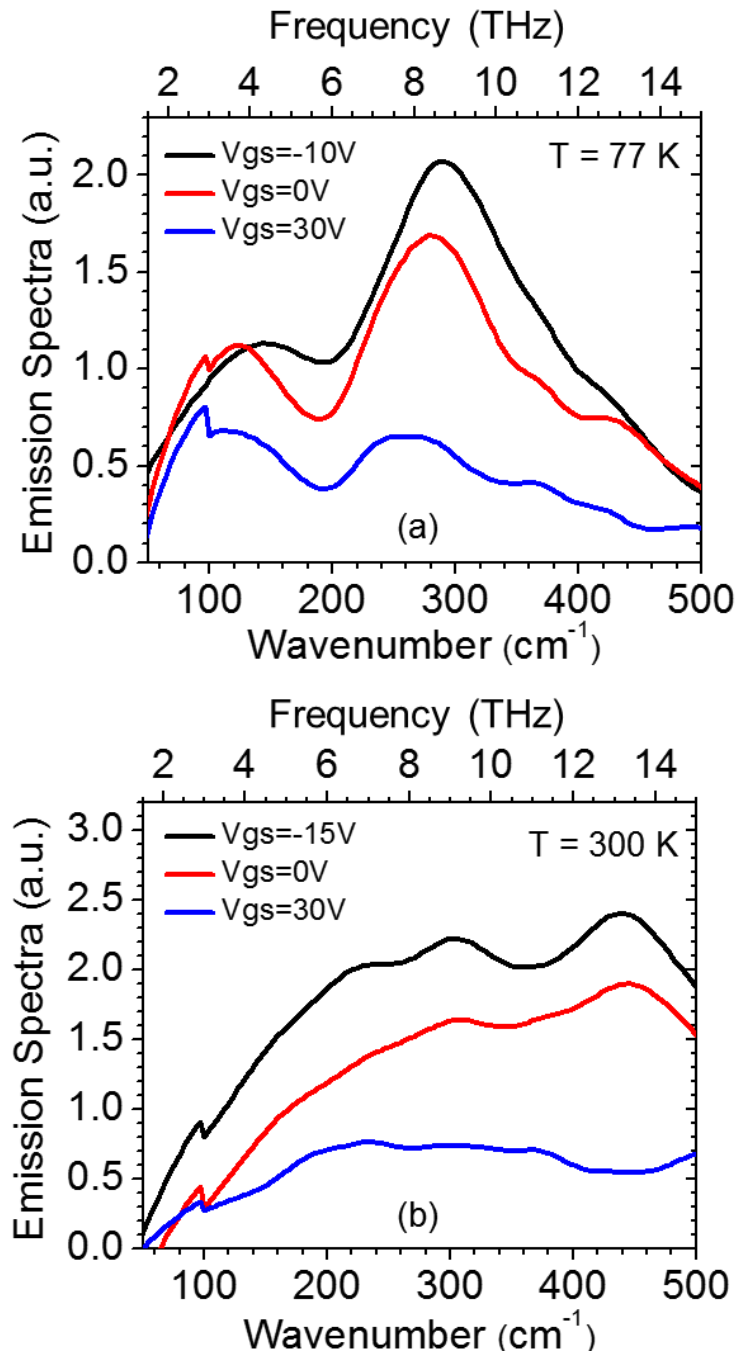


**Figure 3.10** Emission spectrum with different gate voltage  $V_{gs}$  at liquid nitrogen temperature 77 (a), and at room temperature 300 K (b) with fixed  $I_{ds} = 24 \text{ mA}$ .

Figure 3.11 shows similar data measured at a slightly higher source-drain current  $I_{ds} = 28$  mA, where an increase in both the Smith-Purcell emission peak and the blackbody background is observed. In general, increasing  $I_{ds}$  causes an increase in the temperature of the graphene electron gas, which has two opposite effects. On the one hand, the probability that the final electronic states after photon emission are empty [i.e., the factor  $1 - f_{k-g}$  in equation (3.1)] increases, leading to stronger Smith-Purcell radiation. On the other hand, the mobility and mean free path decrease, which tends to quench the Smith-Purcell emission as discussed above. As a result, the Smith-Purcell emission peak does not increase indefinitely with increasing  $I_{ds}$ , and eventually blackbody radiation takes over.

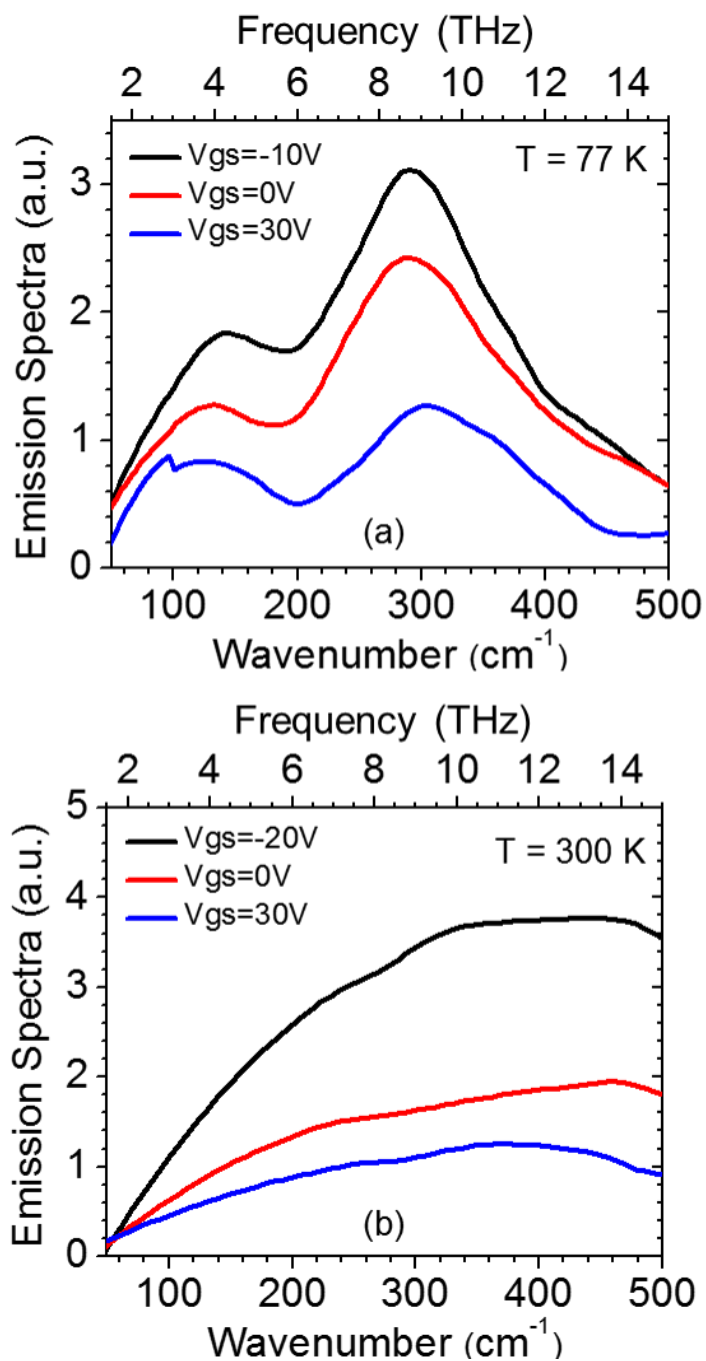


**Figure 3.11** Emission spectrum with different gate voltage  $V_{gs}$  at liquid nitrogen temperature 77 (a), and at room temperature 300 K (b) with fixed  $I_{ds} = 28\text{mA}$ .

These results represent the first experimental demonstration of THz electron-beam radiation from graphene. As clearly illustrated by the temperature dependence of the output spectra, the ultra-high mobility of the hBN-graphene-hBN heterostructure used in these experiments provides a key enabling feature for the measurement of this novel radiation mechanism. It is also important to point out that similar samples have displayed mean free paths  $> 1 \mu\text{m}$  even at room temperature (L. Wang et al. 2013), so that Smith-Purcell emission without cryogenic cooling should also be possible with the same materials platform. Future work in this area will involve additional electroluminescence measurements with samples of different grating periods, to demonstrate the expected geometrical tuning of the emission frequencies.

## **4 TERAHERTZ ELECTRON-BEAM RADIATION IN 1D CARBON NANOSTRUCTURES**

One-dimensional carbon nanostructures such as nanotubes and nanoribbons can also provide near-ballistic electronic transport over micron-scale distances even at room temperature. Here, I consider the generation of terahertz light in these 1D conductors based on the two radiation mechanisms, considered in this thesis (namely cyclotron-like radiation in a sinusoidally corrugated conductor, and the Smith-Purcell effect). In both cases, the radiation properties of the individual charge carriers are again investigated via full-wave electrodynamic simulations, including dephasing effects caused by carrier collisions as in Chapter 3. The overall light output is then computed with a standard model of ballistic charge transport for two particularly suitable types of carbon nanostructures, i.e., zigzag graphene nanoribbons and armchair single-wall nanotubes. Relatively strong emission peaks at geometrically tunable THz frequencies are obtained in each case, with significantly reduced spectral linewidths compared to the graphene samples of the previous chapters, due to the 1D nature of transport in these nanostructures. The corresponding output powers are experimentally accessible even with individual nanowires, and can be scaled to technologically significant levels using array configurations. Therefore, these radiation mechanisms once again represent a promising new paradigm for light emission in condensed matter, which may find important applications in nanoelectronics and THz photonics.

#### 4.1 Proposed radiation mechanisms

One-dimensional carbon nanostructures including graphene and nanotubes represent a promising materials platform for future device applications in nanoelectronics and photonics. Of particular interest for such applications are the large carrier mobilities of these materials, which have enabled the observation of ballistic electronic transport over micron-scale distances even at room temperature. Specific examples of such ballistic samples reported to date include single- and multi-wall carbon nanotubes (Frank et al. 1998)(Javey et al. 2004)(Park et al. 2004)(Purewal et al. 2007), and epitaxial graphene nanoribbons (Baringhaus et al. 2014). Because of their exceptionally long mean free paths, a distinctive analogy can be drawn between the electron (and hole) gases in these nanomaterials and electron beams in vacuum-based systems, so that novel applications inspired by traditional vacuum-tube devices may be envisioned. In the present work (Tantiwanichapan, Swan, and Paiella 2016), I investigate numerically the use of one-dimensional (1D) carbon nanostructures for the generation of terahertz light based on two related electron-beam radiation mechanisms: (I) the emission of cyclotron-like radiation in the presence of mechanical corrugation (as opposed to an externally applied magnetic field), and (II) the Smith-Purcell effect (i.e., radiation by charges in uniform rectilinear motion near a grating (S. J. Smith and Purcell 1953)), as same as examining in 2D graphene in Chapter 2 and 3 respectively.

The basic sample geometries under study are illustrated schematically in Figure 4.1. In Figure 4.1(a), a 1D conductor (such as a carbon nanotube or graphene nanoribbon) is corrugated mechanically to produce a sinusoidal trajectory. In practice, this geometry

could be realized through the direct growth or conformal transfer of the conducting wire on a substrate surface patterned in the shape of a sinusoidal grating. Because of the conductor 1D nature (which ensures that the carrier trajectories perfectly conform to the corrugation), in the presence of a dc voltage the injected electrons (or holes) undergo periodic angular motion and therefore can radiate. This mechanism is analogous to cyclotron radiation as mentioned in Chapter 2. In Figure 4.1(b), I consider a rectilinear conducting wire in the immediate vicinity of a periodic dielectric grating, which could be patterned in the supporting substrate (as in the figure) or fabricated directly above the wire. In this case, radiation can still be emitted by the charge carriers in the 1D conductor as they pass near the grating under uniform rectilinear motion, via the Smith-Purcell effect.

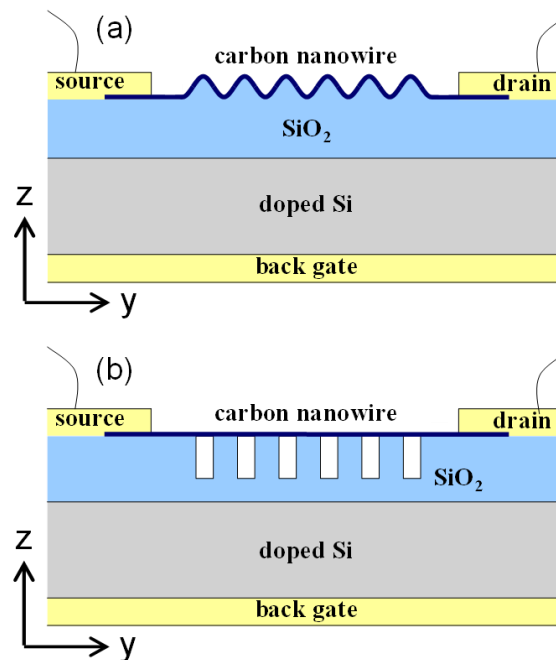


**Figure 4.1 Schematic cross-sectional view of representative device structures for the demonstration of THz electron-beam radiation in 1D carbon nanostructures. (a) Corrugated carbon nanowire for the generation**

**of cyclotron-like THz radiation. (b) Carbon nanowire in the near-field vicinity of a grating for the generation of THz Smith-Purcell radiation.**

For both radiation mechanisms of Figure 4.1, the emission frequency is on the order of  $\nu/\Lambda$  (as shown in detail below), where  $\nu$  is the Fermi velocity and  $\Lambda$  the period of either the sinusoidal trajectory or the nearby grating. In metallic carbon nanostructures, the low-energy electrons and holes generally feature a relatively large Fermi velocity near  $\nu_F \approx 1 \times 10^8$  cm/s. As a result, cyclotron-like and Smith-Purcell radiation frequencies spanning the entire THz spectrum can be obtained with periods of a few hundred nanometers. Therefore, these devices can provide a promising new approach to address a key technology gap of modern-day optoelectronics, namely the lack of practical solid-state THz sources capable of room-temperature operation (Lee and Wanke 2007). More in general, the use of carbon nanomaterials for THz science and technology has already become the subject of increasing interest (Low and Avouris 2014; Tredicucci and Vitiello 2014; Hartmann, Kono, and Portnoi 2014), motivated by their unique electronic properties. In the area of THz sources, several theoretical proposals involving carbon nanotubes (Dragoman and Dragoman 2004; Kibis, Parfitt, and Portnoi 2005; Nemilentsau, Slepyan, and Maksimenko 2007; Kibis, Rosenau Da Costa, and Portnoi 2007; Portnoi, Kibis, and Rosenau da Costa 2008) have been presented, mostly based on interband electronic transitions, tunable plasmonic excitations, or real-space charge oscillations. The experimental demonstrations of THz amplification and emission in optically pumped samples have also already been reported (Sun et al. 2010; Boubanga-Tombet et al. 2012; Prechtel et al. 2012; Bahk et al. 2014; Titova et al. 2015).

In recent chapter, I have investigated numerically the feasibility of THz electron-beam radiation from the two-dimensional electron gas (2DEG) in corrugated (Tantiwanichapan et al. 2013) or grating-coupled (Tantiwanichapan et al. 2014) graphene sheets. In both cases, promising results were obtained in terms of radiated optical power and tunability of the emission frequencies. Here I consider instead two specific types of 1D carbon nanostructures, namely zigzag graphene nanoribbons (ZZ-GNRs) and metallic armchair single-wall nanotubes (AC-SWNTs). The use of 1D conductors for electron-beam radiation is intuitively compelling in light of the aforementioned analogy with vacuum-tube devices, where all electrons can be made to travel roughly along the same direction. In contrast, in a condensed-matter 2DEG the carrier distribution in reciprocal space is such that, even in the presence of a bias voltage, there are carriers traveling along all possible directions on the 2DEG plane. However, carriers traveling along different directions (relative to the corrugation or grating) radiate at different frequencies with different efficiency. Therefore, 1D conductors can be expected to provide narrower and stronger emission peaks, as confirmed by our simulation results presented below. In addition, both zigzag-like GNRs (Baringhaus et al. 2014) and metallic SWNTs (Park et al. 2004; Purewal et al. 2007) have already been shown to exhibit robust ballistic transport over distances longer than 1  $\mu\text{m}$  even at room temperature. Therefore, they both represent a particularly suitable system to investigate THz electron-beam radiation in condensed matter, with significant promise for future technological impact.

#### 4.1.1 Graphene nanoribbons

The crystal structure of a ZZ-GNR (oriented along the  $y$  direction) is shown schematically in Figure 4.2. As in all  $sp^2$ -hybridized carbon allotropes, the underlying lattice is triangular with two carbon atoms per unit cell, denoted A and B. In zigzag nanoribbons, all atoms on each edge parallel to the ribbon axis belong to the same sublattice (A on one edge, B on the other). The opposite extreme is that of armchair edges, which consist of an equal number of alternating A and B atoms. This distinction is important, because the edge shape has a profound impact on the nanoribbon electronic band structure (Nakada et al. 1996). In particular, ZZ-GNRs support localized edge states near the Fermi energy. In contrast, in armchair nanoribbons edge states are absent, and an energy bandgap can be found depending on the ribbon width. In practice, the edges of typical nanoribbons contain both zigzag and armchair sections, and the electronic properties tend to be dominated by the zigzag sites (Katsnelson 2012). Therefore, our present focus on ZZ-GNRs is quite general in terms of applicability to practical samples. Furthermore, the main channel for ballistic transport measured in graphene nanoribbons so far is actually associated with the low-energy subbands involving edge states (Baringhaus et al. 2014), which are characteristic of zigzag-like samples only.

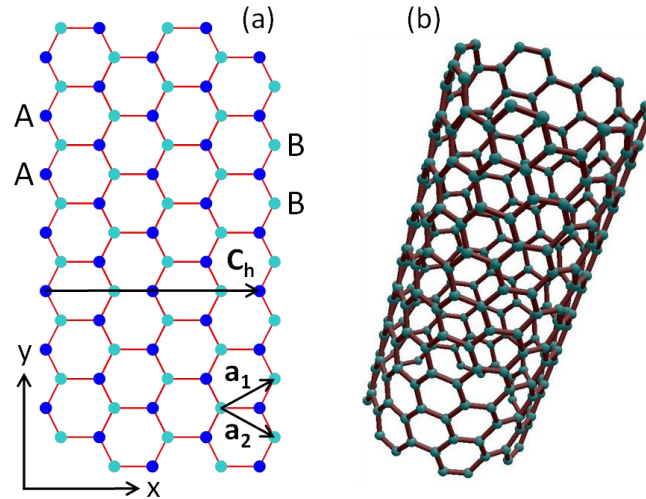


**Figure 4.2** Crystal structure of the 1D carbon nanostructures under study. (a) ZZ-GNR. (b) AC-SWNT. In (a),  $a_1$  and  $a_2$  are the basis vectors of the crystal lattice,  $C_h$  is the chiral vector, and the letters A and B indicate representative atoms belonging to the two sub-lattices.

In general, the energy band diagram of any graphene-derived nanostructure can be computed from that of graphene through the application of suitable boundary conditions. An analytical expression for the dispersion of the conduction and valence bands in graphene can be obtained using a simple tight-binding model as indicated in equation (1.1).

A two-dimensional analogue of the massless Dirac equation can in fact be derived from equation (1.1) using the  $\mathbf{k}\cdot\mathbf{p}$  approximation. In this formulation, the states near the K point are described by a two-component energy eigenvector  $\Psi_K = [\Psi_{KA}, \Psi_{KB}]^T$  (multiplied by the Bloch-periodic function at K), where  $\Psi_{KA}$  and  $\Psi_{KB}$  are the electronic envelope functions over sublattices A and B, respectively. The corresponding energy eigenvalues  $E$  are obtained from the equation

$$v_F \begin{bmatrix} 0 & p_x - ip_y \\ p_x + ip_y & 0 \end{bmatrix} \Psi_K = E \Psi_K \quad (4.1)$$

where  $\mathbf{p}$  is the linear momentum operator. Similarly, the envelope functions  $\Psi_{K'A}$  and  $\Psi_{K'B}$  of the energy states near  $K'$  satisfy the same equation with the Hamiltonian matrix replaced by its transpose.

Within this  $\mathbf{k}\cdot\mathbf{p}$  description, the appropriate boundary condition for a zigzag-like edge that mostly contains atoms of one sublattice (e.g., A) is that the envelope functions associated with the other sublattice (B) must vanish everywhere along the edge (Palacios et al. 2010). For the ZZ-GNR of Figure 4.2(a), I can therefore write

$$\Psi_{KB}(x=0) = \Psi_{K'B}(x=0) = \Psi_{KA}(x=W) = \Psi_{K'A}(x=W) = 0 \quad (4.2)$$

where  $W$  is the width of the nanoribbon. Furthermore, because of translational invariance along the  $y$  direction, all envelope functions  $\Psi_\mu$  (for  $\mu = KA, K'A, KB,$  and  $K'B$ ) must vary with  $y$  as  $\Psi_\mu \propto \exp(iky)$  (with the symbol  $k$  now used to indicate the electronic wavevector along the ribbon axis). By combining equation (4.2) with (4.1) (and its counterpart for the states near  $K'$ ), I then find that nontrivial solutions exist only if

$$\tanh(\alpha W) = \pm \alpha/k \quad (4.3)$$

where  $k$  indicates the electronic wavevector along the ribbon axis, and the parameter  $\alpha$  is related to the energy eigenvalues  $E$  according to  $E = \pm \hbar v_F \sqrt{k^2 - \alpha^2}$ . The nanoribbon subbands are finally computed by solving equation (4.3) for  $E$  as a function of  $k$ .

Representative results are shown in Figure 4.3 for a ZZ-GNR of 40-nm width. Of particular interest here are the lowest-energy conduction and valence subbands, which exhibit a nearly flat dispersion for  $k$  between  $K_y = 2\pi/3a$  and  $K'_y = 4\pi/3a$  (i.e., the  $y$

components of the wavevector at K and K', respectively). Vice versa, for  $k < K_y$  or  $> K'_y$ , the slope of both bands rapidly increases to the graphene limit of  $dE/dk = \pm \hbar v_F$ . These subbands contain the aforementioned localized states confined near the edges of the nanoribbon, as can be verified by solving equation (4.1) and its K'-valley counterpart for the envelope functions. In contrast, for all states in the remaining subbands, the wavefunctions are delocalized across the entire width of the nanoribbon. More detailed band structure calculations also show that electron-electron interactions can lift the degeneracy of the partially flat subbands, thereby opening a bandgap even in ZZ-GNRs (Wakabayashi, Takane, and Sigrist 2007). However, whether these modifications are included or not in this analysis, the Fermi level can still be pushed to the high-slope portion of the lowest-energy conduction (or valence) subband at similar carrier densities. The resulting radiation spectra are then going to be essentially the same, since they are mostly determined by the carriers near the Fermi level.

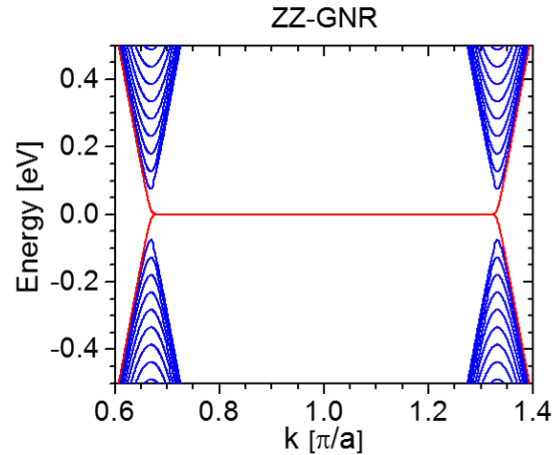


**Figure 4.3 Electronic band structure of a ZZ-GNR with 40-nm width. The wavevector  $k$  is measured along the axis of the nanoribbon, relative to the center of the graphene first Brillouin zone.**

The possibility of ballistic transport in graphene nanoribbons even in the presence of disorder has been investigated theoretically in (Wakabayashi, Takane, and Sigrist 2007). The key conclusion of this study is that the lowest-energy conduction and valence subbands involving edge states can provide a perfectly conducting channel, as long as impurity scattering is sufficiently long range that it cannot promote intervalley transitions (i.e., from states near  $K_y$  to states near  $K'_y$ , and vice versa). The underlying physics is related to the violation of pseudo time-reversal symmetry associated with the different number of forward and backward traveling modes within each valley. Experimentally, room-temperature ballistic transport associated with these conducting channels has been measured in  $\sim 40$ -nm-wide nanoribbons, over distances as long as  $16 \mu\text{m}$  (Baringhaus et al. 2014). At the same time, transport in the higher energy subbands of the same samples has been found to be diffusive, with much shorter mean free paths of about 200 nm. The nanoribbons used in these measurements were synthesized via epitaxial growth on SiC, a

technique that can be scaled to high-density arrays over large device areas.

#### 4.1.2 Carbon nanotubes

The other type of 1D nanostructures considered in this work, AC-SWNTs, is illustrated schematically in Figure 4.2(b). These nanotubes can be conceptually visualized as ZZ-GNRs rolled up about their long axes, so that both ends of the resulting nanocylinders feature armchair edges. As shown in Figure 4.2(a), the chiral vector of AC-SWNTs (i.e., the vector running across the unrolled nanotube perpendicular to its axis) is  $\mathbf{C}_h = n(\mathbf{a}_1 + \mathbf{a}_2) = \sqrt{3}na\hat{\mathbf{x}}$ , where  $\mathbf{a}_1$  and  $\mathbf{a}_2$  are the basis vectors of the crystal lattice and  $n$  is an integer related to the tube circumference  $C = \sqrt{3}na$ . In general, the electronic band structure of carbon nanotubes can be obtained from that of graphene by imposing periodic boundary conditions with periodicity  $C$  along the direction of the chiral vector, i.e., by requiring that the wavevector component in the direction of  $\mathbf{C}_h$  is quantized in integral multiples of  $2\pi/C$  (Saito, Dresselhaus, and Dresselhaus 1998). For AC-SWNTs, this condition simply becomes

$$k_x = \frac{2s\pi}{\sqrt{3}na} \quad (4.4)$$

for any integer  $s$  between 1 and  $2n$ .

Figure 4.4 shows the electronic band structure of an AC-SWNT with  $n = 15$  (corresponding to a typical tube diameter  $C/\pi$  of 2 nm), computed by substituting equation (4.4) into equation (1.1). As illustrated by this plot, AC-SWNTs are metallic, which follows from the fact that the crystal wavevectors of the high-symmetry points K and K'

(where the graphene bandgap is zero) satisfy the boundary condition of equation (4.4) for  $s = n$ . As a result, the conical shape with slope  $\hbar v_F$  and the zero-energy crossing of the graphene conduction and valence bands near K and K' are preserved in the  $s = n$  subbands of AC-SWNTs near  $K_y$  and  $K'_y$ . This arrangement is particularly favorable for the radiation mechanisms under study, because all electrons and holes in the main conducting channels (the  $s = n$  subbands) travel at the same, relatively high velocity  $v_F$ , and therefore can radiate at the same frequency with relatively high output power. In passing I note that approximately one third of all possible types of SWNTs (depending on their chiral vector  $\mathbf{C}_h = n\mathbf{a}_1 + m\mathbf{a}_2$ ) can be expected to be metallic based on similar arguments. Therefore, the calculation results presented below may also be extended to these other types of nanotubes, although in many instances (but not in AC-SWNTs) curvature effects lead to the opening of a small bandgap (Saito, Dresselhaus, and Dresselhaus 1998).

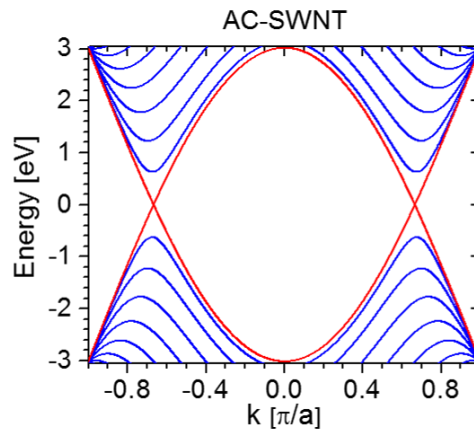


**Figure 4.4 Electronic band structure of an AC-SWNT with 2-nm diameter. The wavevector  $k$  is measured along the axis of the nanotube, relative to the center of the graphene first Brillouin zone.**

The electronic transport properties of metallic SWNTs have been widely investigated over the past several years, including the theoretical prediction (White and Todorov 1998) and experimental observation of (quasi)ballistic conduction (Javey et al. 2004; Park et al. 2004). At room temperature, the electronic mean free path  $l_m$  of high-quality samples is limited by electron-phonon scattering and its specific value depends on the applied voltage. At low bias (less than about 0.2 V), all carriers have insufficient energy to emit optical phonons, and their mobility is limited by a relatively weak acoustic-phonon scattering mechanism, leading to large mean free paths exceeding 1 micron (Park et al. 2004). At higher voltages, the emission of optical phonons becomes allowed, and  $l_m$  is correspondingly decreased by an order or magnitude. Finally, at low temperatures and low bias, mean free paths as long as  $\sim 8 \mu\text{m}$  have been measured, only limited by impurity scattering (Purewal et al. 2007). In general, the electron-beam radiation mechanisms under study require ballistic transport over at least a few periods  $\Lambda$  of the sinusoidal trajectory or nearby grating, and THz radiation frequencies are obtained with periods of a few 100 nm. Therefore, metallic SWNTs also appear to be suitable for these mechanisms, even at room temperature, as long as the applied voltage is kept sufficiently small.

In order to investigate the radiation properties of the nanostructures of Figure 4.1, I first consider an arbitrary individual electron in these 1D conductors and compute its light output using the FDTD method as same as the simulation of graphene in chapter 2 and 3.

Next, I consider a ZZ-GNR or AC-SWNT of length  $L$  and electron density  $N$  (e.g., introduced via electrostatic doping with a back gate), in the geometry of Figure 4.1(a) or

Figure 4.1(b) under a bias voltage  $V$ . Its total output power spectrum per unit length can be calculated as follows

$$P_{\text{tot}}(\nu) = \frac{2}{L} \sum_k P_k(\nu) f(E_0(k)) [1 - f(E_0(k) - h\nu)] \quad (4.5)$$

where  $\nu$  is the emission frequency, the factor of 2 accounts for the spin degeneracy,  $E_0(k)$  is the dispersion relation of the lowest conduction subband,  $P_k(\nu)$  is the output power spectrum of a single electron in the Bloch state of energy  $E_0(k)$ , and  $f$  is the electronic distribution function. Pauli blocking effects are explicitly included in this equation through the last two terms, where  $f(E_0(k))$  is the probability that the initial electronic state is occupied, and  $1 - f(E_0(k) - h\nu)$  is the probability that the corresponding final state after photon emission is empty. At the same time, equation (4.5) does not include any contribution to the output radiation from the higher-energy subbands of the wire, even though these subbands may contain an appreciable number of electrons (particularly in highly doped and/or large wires). The reason is that (quasi)ballistic transport in these 1D carbon conductors has only been measured in the lowest-energy subbands (i.e., the partially flat subbands involving edge states in ZZ-GNRs (Baringhaus et al. 2014), and the linear subbands with zero energy separation in metallic SWNTs (Javey et al. 2004; Park et al. 2004; Purewal et al. 2007)). In contrast, for the higher-energy subbands the measured mean free paths are too small to allow for appreciable electron-beam radiation.

For each device geometry (either cyclotron-like or Smith-Purcell), the single-electron emission spectra  $P_k(\nu)$  depend on the wavevector  $k$  only through the velocity  $v_k = dE_0/d(\hbar k)$ . These spectra are computed via the FDTD simulations described above

for a selection of all possible velocities  $v_k \leq v_F$ , and are generally found to consist of a sharp peak at a frequency on the order of  $v_k/\Lambda$  (weaker features at higher-order harmonics are also obtained in the same calculations, but are not considered in the following analysis for simplicity). From these simulation results, the center frequency, full width at half maximum (FWHM), and integrated power of each peak are determined. Next, the values of the same parameters for all other velocities  $v_k$  are extrapolated using a polynomial fit. The single-electron spectra  $P_k(\nu)$  for all values of  $v_k$  are then approximated in equation (4.5) with Gaussian peaks having the correct center frequencies, FWHMs, and integrated powers (as determined with this fitting procedure). The choice of a Gaussian function is consistent with the shape of the FDTD single-electron emission peaks, and does not in any case significantly affect the resulting shape of  $P_{\text{tot}}(\nu)$ .

Finally, the occupation probabilities  $f$  in equation (4.5) are computed using a standard model for the electronic distribution function of ballistic conductors with ideal (i.e., reflection-less) contacts (Datta 1995). In this model, all electrons moving from left to right can only originate from (and therefore must be in thermal equilibrium with) the contact on the left side of the conductor, and vice versa. As a result, for states with positive velocity (i.e., with  $dE_0/dk > 0$ ), the occupation probability  $f(E_0(k))$  can be taken to be a Fermi-Dirac distribution function with Fermi energy equal to the chemical potential  $\mu_l$  of the left contact. Similarly, all electrons in states with  $dE_0/dk < 0$  can be assumed to be in thermal equilibrium with the same chemical potential  $\mu_r$  as the right contact. To determine  $\mu_l$  and  $\mu_r$ , first I note that their difference must be equal to the applied voltage  $V$  times the electron charge  $-q$ . Second, I require that the sum of the occupation

probabilities of all states in the conducting wire (including states in the higher-energy subbands) must be equal to the electron density  $N$ . The same description of the electronic distribution function  $f$  leads to the Landauer formulation of conduction, which provides a well-established model of (quasi)ballistic transport (Datta 1995).

## 4.2 Simulation results

The simulation methods just described were applied to several structures based on the corrugated wire of Figure 4.1(a) or the Smith-Purcell configuration of Figure 4.1(b), for different values of the period  $\Lambda$  and the electron mean free path  $l_m$ . In each structure the substrate material below the conducting wire is  $\text{SiO}_2$ , modeled with a frequency-dependent permittivity from the internal database of the FDTD simulation engine (“FDTD Solutions” 2015). This choice of substrate material is based on the aforementioned measurements of (quasi)ballistic transport with metallic SWNTs (Javey et al. 2004; Park et al. 2004; Purewal et al. 2007). Alternative substrates may also be considered for the same devices, including hBN, SiC (as used with the ballistic ZZ-GNRs of (Baringhaus et al. 2014)), and  $\text{HfO}_2$ . In fact, theoretical studies indicate that improved transport properties may be obtained with carbon-based conductors deposited or grown on such substrates, due to reduced remote scattering from surface optical phonons and coupled plasmon-phonon modes compared to  $\text{SiO}_2$  (Javey et al. 2004; Park et al. 2004; Purewal et al. 2007). The corrugation of the cyclotron-like samples is sinusoidal with amplitude  $A = \Lambda/4$ , whereas in the Smith-Purcell devices the grating consists of rectangular ridges of width  $W = \Lambda/2$  and height  $H = 300$  nm. These parameters were selected via initial FDTD simulations so as to maximize the output

radiation power. The lateral dimensions of the 1D conductors are the same as in the band-structure calculations of section 4.1.1, i.e., the simulated ZZ-GNRs have a width of 40 nm (as in the ballistic samples of ref. 9) and the AC-SWNTs have a typical nanotube diameter of 2 nm. Additional calculations show that the output radiation depends only weakly on these lateral dimensions, as long as the dispersion of the lowest-energy conduction subband maintains the same features shown in Figure 4.3 and Figure 4.4.

In the FDTD calculations of the single-electron emission spectra, the computational domain has the shape of a cube centered about the dipole distribution, with 600- $\mu\text{m}$  side length and perfectly matched layers on all boundaries. The corrugated substrate or grating lies at the center of the x-y plane, with  $5 \times 5 \mu\text{m}^2$  area. All the FDTD computational parameters including mesh size and frequency resolution were optimized through extensive convergence tests. In passing, I note that the large disparity between the calculated emission wavelengths (several 10  $\mu\text{m}$ ) and the periodicities of the underlying nanostructures (a few 100 nm) makes these simulations extremely demanding in terms of computational resources. As explained above, in the FDTD simulations I consider an electron traveling along the conductor trajectory at a few different velocities  $v_k$  (specifically, 0.2, 0.4, 0.6, 0.8, and 1 times the graphene Fermi velocity  $v_F$ ). The details of the conductor band structure (ZZ-GNR versus AC-SWNT) are then introduced when the total output power spectra are computed from the FDTD simulation results using equation (4.5). In all calculations presented below based on this equation I assume a Fermi energy  $E_F = 100 \text{ meV}$  above the Dirac point, an applied bias voltage  $V = 0.1 \text{ V}$ , and room temperature. In the case of ZZ-GNRs, a wide range of electron velocities  $v_k \leq v_F$

contribute to  $P_{\text{tot}}(\nu)$ , due to the significant curvature of the lowest-energy conduction subband near such Fermi energy. In AC-SWNTs the lowest-energy conduction subband is relatively linear near  $E_F$  and all radiating electrons have velocity close to  $v_F$ .

Representative FDTD simulation results for a cyclotron-like device are shown in Figure 4.5 for all five electron velocities considered. Specifically, the traces plotted in this figure are obtained by dividing the single-electron power spectra  $P_k(\nu)$  by the photon energy  $h\nu$ , which gives the photon emission rate per unit frequency. The corrugation period  $\Lambda$  here is 68 nm, and the corresponding length  $l_{\text{cycle}}$  traveled by the electron in each cycle of the sinusoidal trajectory is approximately 100 nm. The mean free path  $l_m$  (i.e., the length of the equivalent dipole distribution in the FDTD simulations) is taken to be 3  $\mu\text{m}$ , which is large enough to ensure that the resulting broadening does not affect the shape of the output spectra  $P_{\text{tot}}(\nu)$ , but otherwise reasonably short to minimize the computational time. The results presented here therefore apply to the optimal case of highly ballistic samples, whereas the effect of shorter mean free paths is described later in this section. For each electron velocity  $v_k$ , the frequency of peak emission in the spectra of Figure 4.5 is approximately equal to  $v_k/l_{\text{cycle}}$  (i.e.,  $v_k/v_F \times 10$  THz for  $l_{\text{cycle}} = 100$  nm), which is consistent with expectations for cyclotron-like radiation (Jackson 1975). Incidentally, it should be noted that only a relatively narrow spectral region is considered in each one of these calculations, centered about the main radiation peak, so that the aforementioned weaker emission features at higher-order harmonics are not included.

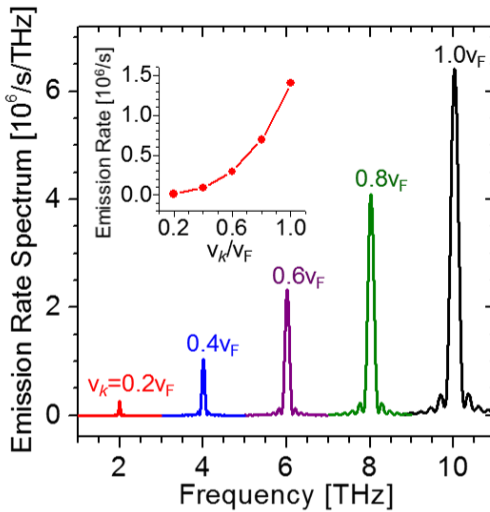


**Figure 4.5 Photon emission rate per unit frequency of an electron in a corrugated carbon nanowire, plotted as a function of radiated frequency for different values of the electron velocity  $v_k$ . The corrugation period and amplitude are 68 nm and 17 nm, respectively. Inset: total emission rate of the same electron, integrated over all frequencies, versus electron velocity.**

The spectra of Figure 4.5 also show that the single-electron output power increases rapidly with increasing electron speed. This behavior is again in agreement with basic expectations: for example,  $P_k \propto v_k^4$  according to the Larmor formula for cyclotron radiation (which however only applies in the limit of  $A \ll \Lambda$ ) (Jackson 1975). The radiation mechanisms under study therefore benefit strongly from the relatively large electron velocities of carbon-based nanostructures. In particular, in the AC-SWNTs of Figure 4.4, the slope  $|v_k| = |dE_0/d(\hbar k)|$  of the lowest-energy conduction and valence subbands is approximately equal to  $v_F \approx 1 \times 10^8$  cm/s over a broad energy range across the Dirac point. In the ZZ-GNRs of Figure 4.3, the lowest subbands feature a nearly flat dispersion with almost zero velocity near the Dirac point, but their slope  $|v_k|$  then rapidly approaches  $v_F$  as the energy is increased or decreased beyond a few  $\pm 10$  meV. As already

mentioned, in the calculations presented below I assume a chemical potential  $E_F = 100$  meV, so that even in the ZZ-GNRs the carriers near the Fermi level (i.e., the carriers that produce the largest contribution to the sum of equation (4.5) travel at a relatively high velocity close to  $v_F$ .

The inset of Figure 4.5 shows the total emission rate  $1/\tau_{rad}$  integrated over all frequencies and plotted as a function of electron velocity. Values above  $1 \times 10^6$  photons/s are obtained for  $v_k \approx v_F$ , corresponding to a radiative lifetime  $\tau_{rad}$  of less than 1  $\mu$ s. I emphasize that such emission rates are significant at THz frequencies. In fact, similar or smaller rates are obtained for spontaneous emission from the active materials of THz quantum cascade lasers (QCLs), which represent the current state-of-the-art for solid-state THz sources, albeit limited to operation at cryogenic temperatures (Lee and Wanke 2007). For example, spontaneous emission lifetimes ranging from 3 to over 60  $\mu$ s are reported in references (Xu, Hu, and Melloch 1997; Rochat et al. 1998; Williams et al. 1999) for different THz QCL designs. Finally, I note that the same FDTD simulations of Figure 4.5 applied to Smith-Purcell devices produce qualitatively similar results.

Figure 4.6 shows a selection of emission spectra  $P_{tot}(v)$  computed with equation (4.5) for different combinations of carbon nanostructure (ZZ-GNR or AC-SWNT) and radiation mechanism (cyclotron-like or Smith-Purcell). Each panel contains four spectra corresponding to different values of the corrugation or grating period  $\Lambda$ , which were selected to produce emission peaked near 4, 6, 8, and 10 THz, as an illustration of the inherent geometric tunability of the underlying radiation mechanisms. The linewidth and shape of these spectra are determined almost entirely by the dispersion of the single-

electron emission frequency with velocity  $|v_k|$ . In general, the output radiation is mostly produced by the electrons in states within a few units of thermal energy  $k_B T$  from the Fermi level (due to Pauli blocking constraints), and the emission spectrum then depends on their velocity distribution. In ZZ-GNR samples,  $|v_k|$  near  $E_F$  exhibits an appreciable variation with  $k$ , which results in the asymmetric broadening observed in the emission spectra of Figure 4.6(a), and Figure 4.6(b), with the slower electrons emitting at lower frequencies and at a smaller rate. In AC-SWNTs,  $|v_k|$  near  $E_F$  is nearly constant with  $k$ , but with slightly different values in the two branches of opposite slope on either side of each conduction-subband minimum. As a result, the AC-SWNT emission spectra consist of two narrow overlapping peaks centered at slightly different frequencies, which can be observed most clearly in the 10-THz feature of Figure 4.6(c). In any case, all spectra shown in Figure 4.6 are significantly narrower than the output of similar radiation mechanisms in 2D graphene samples (Tantiwanichapan et al. 2013; Tantiwanichapan et al. 2014), which suffer from substantial broadening caused by carriers traveling along different directions and emitting at different frequencies.

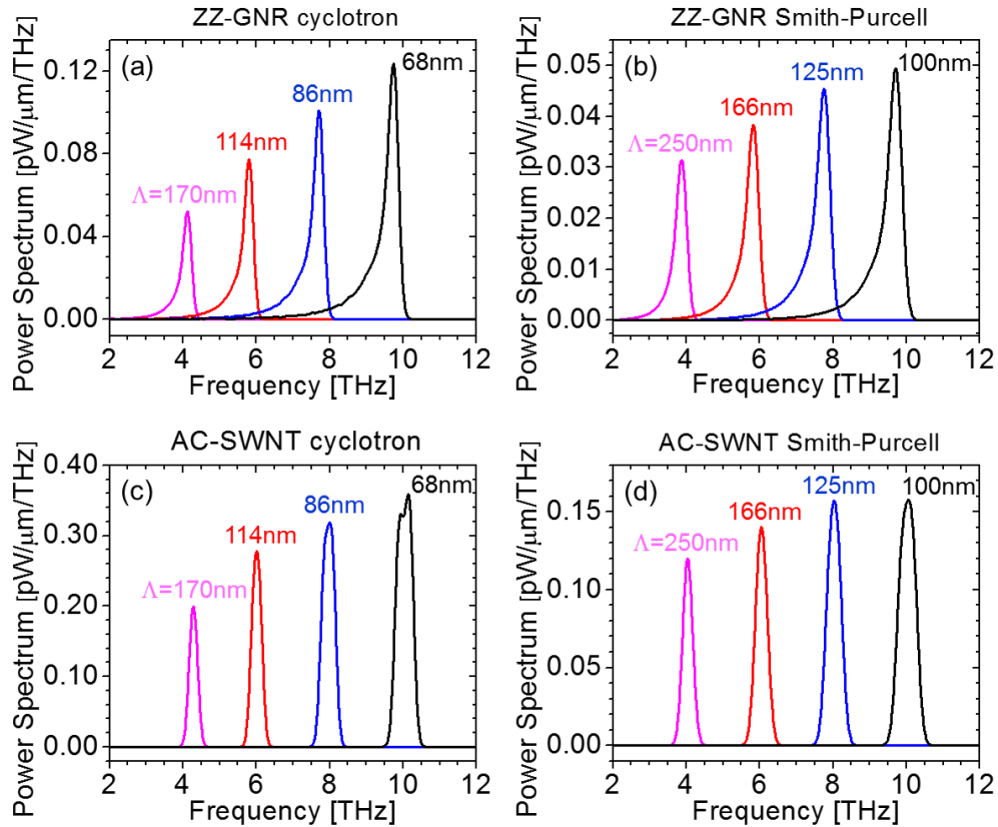


**Figure 4.6** Output radiation spectra per unit length for different periods of the grating or corrugation: (a) cyclotron-like radiation from sinusoidally corrugated ZZ-GNRs; (b) Smith-Purcell emission from ZZ-GNRs near a rectangular grating; (c) cyclotron-like radiation from sinusoidally corrugated AC-SWNTs; (d) Smith-Purcell emission from AC-SWNTs near a rectangular grating.

The total radiation power per unit length produced by the structures of Figure 4.6, integrated over all frequencies, is plotted as a function of the corresponding frequency of peak emission in Figure 4.7. The comparison among the different nanomaterials and radiation mechanisms under study is clearly displayed in this figure. For both types of 1D conductors (ZZ-GNRs and AC-SWNTs), cyclotron-like emission is always more efficient than Smith-Purcell radiation. This observation makes intuitive sense, since the latter

mechanism involves charges in linear rectilinear motion and relies on the (non-unity) diffraction efficiency of the underlying grating. Furthermore, regardless of the emission process, AC-SWNTs consistently produce stronger radiation than ZZ-GNRs emitting at the same frequency. This difference can be ascribed to the more favorable band structure of metallic nanotubes, which leads to a smaller distribution of carrier velocities near the maximum speed  $v_F$  for all the radiating charges.

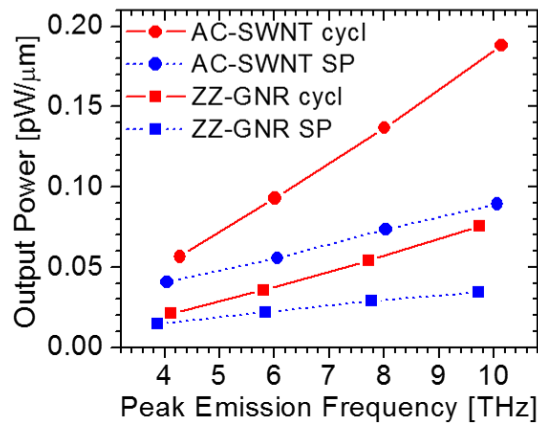


**Figure 4.7 Total output power per unit length of the structures of Figure 4.6, integrated over all frequencies and plotted as a function of the corresponding frequency of peak emission.**

The data of Figure 4.7 also show that experimentally measurable cyclotron-like or Smith-Purcell radiation can be produced even by a single nanotube or nanoribbon. Specifically, for all structures considered in this figure, output powers of several pW (i.e., above the noise equivalent power of standard Si THz bolometers) are obtained with reasonable conductor lengths of about 100  $\mu\text{m}$ . For comparison, I also note that the power levels per unit length shown in Figure 4.7 are about three orders of magnitude higher than theoretical predictions for THz interband spontaneous emission across fully inverted bands

in metallic SWNTs (Kibis, Rosenau Da Costa, and Portnoi 2007). The device structures under study can therefore be envisioned as promising building blocks for future nanoscale electronic circuits operating at ultrahigh frequencies. Furthermore, if the same structures can be integrated in high-density arrays, technologically significant power levels for THz-photonics applications are obtained (e.g., in the  $\mu\text{W}$  range). In particular, the ballistic ZZ-GNRs described in section 4.1.1 are produced by epitaxial growth techniques (Baringhaus et al. 2014), which are readily applicable to the fabrication of ordered arrays with macroscale (e.g., mm-range) dimensions. Significant progress has also been reported in recent years towards the synthesis of high-density arrays of horizontally aligned nanotubes with sorted chirality (Titova et al. 2015; Kang et al. 2007). In principle, these ZZ-GNR or AC-SWNT arrays could also be combined with an optical cavity for the demonstration of coherent stimulated emission, and ultimately even lasing, in analogy with the operation of traditional FELs. The design and analysis of suitable device geometries will be the subject of future study.

Finally, the effect of electronic collisions is illustrated in Figure 4.8, where again each panel corresponds to a different combination of carbon nanostructure and radiation mechanism. In each case, we consider three different values of the mean free path  $l_m$  (i.e., the length of the equivalent dipole distribution in the FDTD simulations), namely 3, 1, and 0.5  $\mu\text{m}$ . The device period  $\Lambda$  is fixed at the value that produces emission near 10 THz, and all other parameters are the same as in Figure 4.6. As expected, decreasing the electronic mean free path causes a broadening of the emission spectra and a reduction in their peak values. A shift in the center frequencies is also observed (particularly in the case of Smith-

Purcell emission), a behavior that is often associated with collision broadening (Peach 1981). In any case, even for the lowest mean free path of  $0.5 \mu\text{m}$  considered in these plots, the emission peaks remain well resolved with relatively large quality factor. The key conclusion is that the phenomenon under radiation study can be implemented using realistic high-quality samples based on existing technologies.

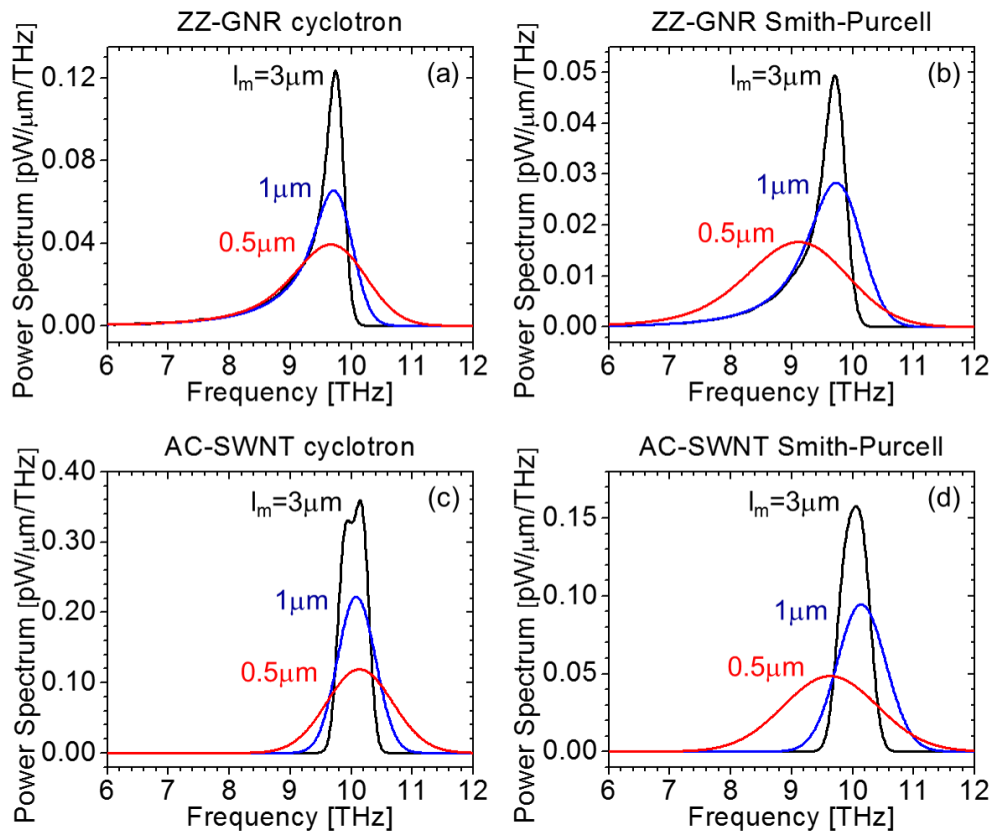


**Figure 4.8** Output radiation spectra per unit length for different values of the electronic mean free path: (a) cyclotron-like radiation from sinusoidally corrugated ZZ-GNRs; (b) Smith-Purcell emission from ZZ-GNRs near a rectangular grating; (c) cyclotron-like radiation from sinusoidally corrugated AC-SWNTs; (d) Smith-Purcell emission from AC-SWNTs near a rectangular grating.

In summary, I have investigated numerically the use of 1D carbon nanostructures

(specifically ZZ-GNRs and AC-SWNTs) for the generation of THz light based on two related electron-beam radiation mechanisms (i.e., cyclotron-like emission in the presence of mechanical corrugation and the Smith-Purcell effect). In all cases I find that experimentally accessible output powers at geometrically tunable THz frequencies can be obtained even with individual nanowires. Of all combinations of radiation mechanism and carbon nanostructure considered, cyclotron-like emission from AC-SWNTs produces the highest output power at all frequencies. At the same time, ZZ-GNRs have the advantage of more immediate compatibility with integration in high-density arrays, at least based on current fabrication methods. The cyclotron-like sample geometry may also be more challenging to implement compared to Smith-Purcell devices, due to the critical requirement of conformal adhesion on a nanoscale sinusoidal grating. Both radiation mechanisms are also found to be relatively robust with respect to electronic collisions, with pronounced emission peaks obtained even in the presence of sub-micron mean free paths. These results suggest that 1D carbon nanostructures represent a uniquely suited materials platform for the demonstration and study of electron-beam radiation processes in condensed matter. Possible applications include ultrahigh-frequency oscillators for future nanoelectronic circuits, and (in the case of high-density arrays) radiation sources for THz photonics. The observed increase in output power with increasing frequency of peak emission (see Figure 4.7) is particularly significant in this respect, since existing room-temperature THz sources are limited to frequencies below  $\sim 1$  THz (Lee and Wanke 2007). The radiation mechanisms under study may therefore provide a promising solution to this important technology gap.

## 5 GRAPHENE TERAHERTZ PLASMONICS

### 5.1 Theoretical background

The basic device geometry investigated in chapter 3 (i.e., a conducting sheet parallel to a nearby grating) can also be for the excitation and outcoupling of 2D plasmon polaritons in the conductor. This approach has been used experimentally to generate THz radiation in high-mobility semiconductor heterojunctions, where the plasmonic oscillations were excited through the decay of hot electrons (injected with an applied bias voltage) and then diffractively scattered by the grating (Höpfel, Vass, and Gornik 1982; Hirakawa et al. 1995). A recent theoretical study has also considered the same radiation mechanism in graphene (S. Liu et al. 2014) with an external electron beam propagating near the graphene layer used for the efficient excitation of THz surface plasmons. In the course of this Thesis work, I have also investigated THz plasmon in grating-coupled graphene via transmission spectroscopy and electroluminescence measurements.

Plasmonics is an exciting area of applied-physics research with a variety of potential applications in information processing, bio-medical sensing, and imaging technologies. Plasmon-mediated THz detection and emission is another promising mechanism, for example in the context of 2D hot plasma oscillations in Field Effect Transistors. Graphene is a relatively new material for plasmonic research with a couple of important advantages, namely high electronic mobility at room temperature leading to relatively low plasmon propagation losses, and dynamically tunable carrier densities that allow tuning the plasmonic dispersion curve.

Surface plasmon polaritons are guided electromagnetic waves propagating along the interface between two materials having negative and positive dielectric constants (e.g., a metal and a dielectric), as shown schematically in Figure 5.1. Their dispersion relation is given by

$$k = \frac{\omega}{c} \sqrt{\frac{\epsilon_m \epsilon_d}{\epsilon_m + \epsilon_d}} \quad (5.1)$$

where  $k$  is the surface-plasmon wavenumber,  $\omega$  is its angular frequency,  $\epsilon_m < 0$  is the dielectric constant of the metal, and  $\epsilon_d > 0$  is the dielectric constant of the dielectric material.

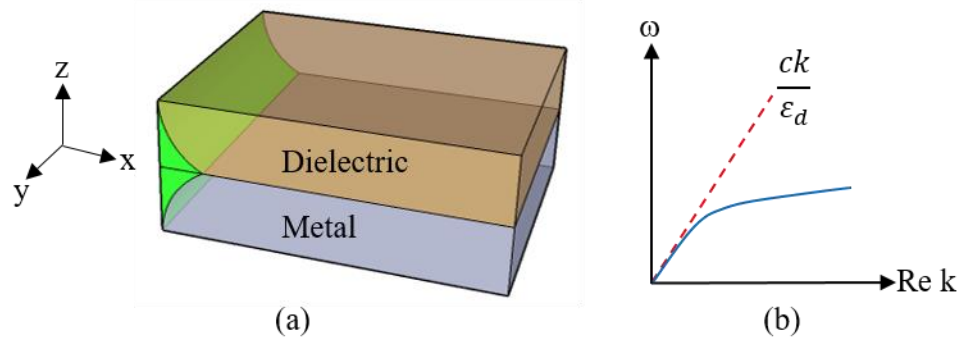


**Figure 5.1 (a) Surface plasmons at the interface between a metal and a dielectric. (b) Dispersion relation of surface plasmons (solid line) and of radiation in the bulk dielectric material (dash line).**

In a sheet of graphene bounded by two dielectric materials, the plasmonic dispersion relation becomes (Jablan, Buljan, and Soljačić 2009)

$$\frac{\epsilon_{r1}}{\sqrt{k^2 - \frac{\epsilon_{r1}\omega^2}{c^2}}} - \frac{\epsilon_{r2}}{\sqrt{k^2 - \frac{\epsilon_{r2}\omega^2}{c^2}}} = -\frac{\sigma(\omega, k)i}{\omega\epsilon_0} \quad (5.2)$$

where the graphene conductance  $\sigma(\omega, k)$  can be approximated as (Jablan, Buljan, and Soljačić 2009)

$$\sigma = \frac{e^2 E_F}{\pi \hbar^2} \frac{i}{\omega + i\tau^{-1}} \quad (5.3)$$

In these equations,  $\varepsilon_{r1}$  and  $\varepsilon_{r2}$  are the dielectric constants of the surrounding materials,  $E_F$  is the graphene Fermi energy, and  $\tau$  is electron relaxation time. By combining equations (5.2) and (5.3), the plasmonic dispersion relation in graphene can be written as

$$k(\omega) = \frac{\pi \hbar^2 \varepsilon_0 (\varepsilon_{r1} + \varepsilon_{r2})}{e^2 E_F} \left(1 + \frac{i}{\tau\omega}\right) \omega^2 \quad (5.4)$$

In general, surface plasmon polaritons have higher wavevector (i.e., momentum) compared to light at the same frequency propagating in the adjacent bulk dielectric material. Therefore, in order to couple externally incident light into plasmon waves (or vice versa), a suitable momentum matching technique must be employed. One option is the use of a diffraction grating of period  $\Lambda$ , leading to the phase matching condition  $Re(k(\omega)) = \frac{2\pi}{\Lambda}$  (for the case of normally incident light). Using equation (5.4), this condition implies that a grating of period  $\Lambda$  can be used to couple normally-incident light into and out of graphene plasmons at the specific frequency  $\omega_0$  given by (Gao et al. 2012)

$$\omega_0 = \sqrt{\frac{2e^2 E_F}{\hbar^2 \varepsilon_0 (\varepsilon_{r1} + \varepsilon_{r2}) \Lambda}} \quad (5.5)$$

It is important to note that since the Fermi energy  $E_F$  depends on the gate voltage, the resonance frequency of grating-coupled graphene plasmons can be tuned electrically by

varying  $V_{gs}$  (Gao et al. 2012; P. Q. Liu et al. 2015). A plot of  $\omega_0$  versus carrier density  $n$  for different values of the grating period  $\Lambda$  is shown in Figure 5.2. It is clear from this figure that  $\omega_0$  can be tuned across the entire THz spectrum by suitably varying the gate voltage and/or the grating period.

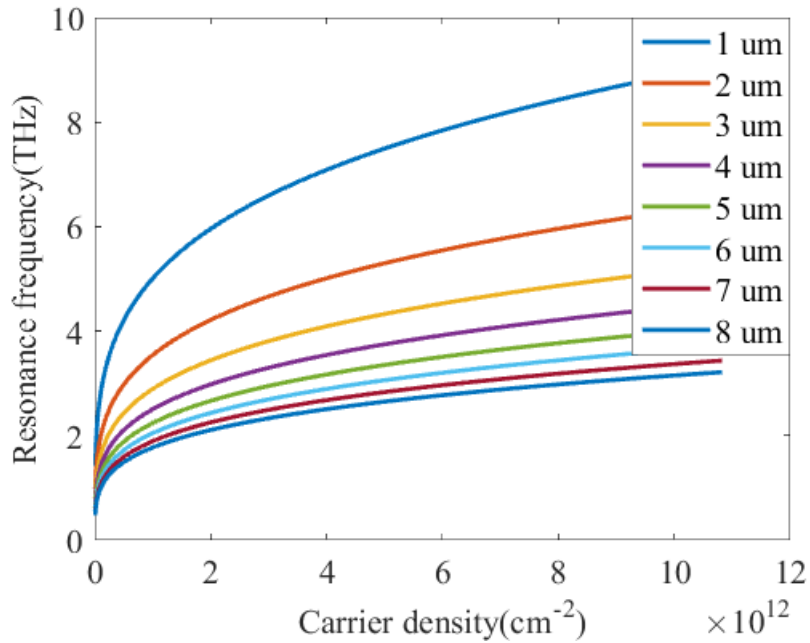


**Figure 5.2 Resonance frequency of grating-coupled graphene plasmons versus carrier density, for different values of the grating period.**

THz plasmons in graphene can then be investigated via normal-incidence transmission spectroscopy measurements with grating-coupled samples, through the observation of absorption peaks at the resonance frequencies of equation (5.5). These measurements have also been carried out during this thesis work. THz emission from the same geometry can also in principle be obtained through the electrical excitation of graphene plasmons and their subsequent outcoupling via diffraction by the grating. As in

the work of reference (Höpfel, Vass, and Gornik 1982) and (Hirakawa et al. 1995), this mechanism can be driven by a sufficiently large DC bias, leading to the creation of a high density of hot electrons, some of which will then decay into plasmonic oscillations. Compared to the SP effect described in the previous sections, grating-coupled plasmon emission at THz frequencies requires larger grating periods, and has the advantage of longer mean free paths of the underlying electronic excitation (i.e., plasmons as opposed to individual electrons). On the other hand, its excitation process is likely less efficient as a significant fraction of the excited hot electrons are likely to decay by other means (e.g., phonon emission). In previous work with traditional semiconductor 2DEGs (Wirner et al. 1993; Höpfel, Vass, and Gornik 1982; Hirakawa et al. 1995), stronger THz emission from grating-coupled plasmons has been measured compared to Smith-Purcell radiation. However, as described in the previous chapter, this situation may be different in graphene by virtue of its unique electronic properties.

## **5.2 Sample fabrication**

To investigate these THz plasmons in graphene, I have fabricated several samples consisting of 2D metal pillar arrays on CVD using the process shown in Figure 5.3. CVD graphene sheets are used in this work because they can be substantially larger than mechanically exfoliated flakes, as needed for transmission measurements with the relatively large ( $\sim 1\text{mm}^2$ ) beam of the FTIR Spectrometer. The fabrication process starts with the formation of the gate contact on a doped-Si substrate by photolithography, BOE etching, and deposition of Cr and Au by electron-beam evaporation (same as in section 3.3). CVD graphene is then transferred on the  $\text{SiO}_2/\text{Si}$  substrate by my collaborator Xuanye

Wang from Professor Swan's group. Specially, Xuanye first spins PMMA on top of CVD graphene grown on a copper foil. Next, the PMMA/graphene stack floating in the copper etchant is scooped with a piece of Si and cleaned in DI water. Finally, the same PMMA/graphene stack is picked up it with the pre-gated substrate and the PMMA is removed with acetone. In order to identify high-quality regions in the transferred graphene sheet, Xuanye also performs a detailed Raman spectroscopy map. Next, I pattern the graphene sheet using Electron beam lithography (EBL) and plasma ashing to produce a rectangular sample of high-quality graphene. Finally, I fabricate the 2D metal pillar array and the source-drain contacts using EBL and electron-beam evaporation consisting of a Cr/Au bilayer with 5nm and 60nm thickness, respectively.

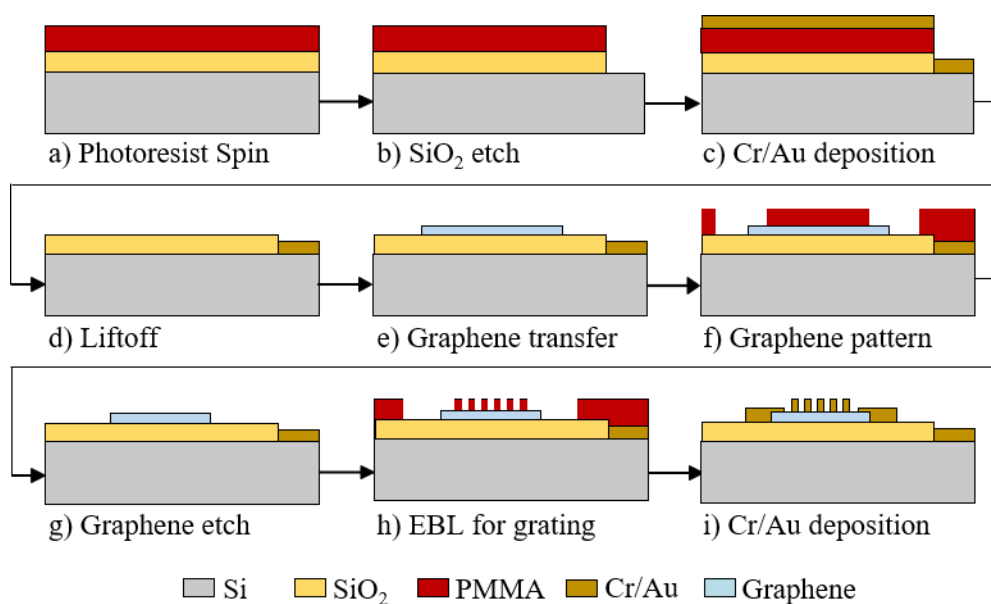
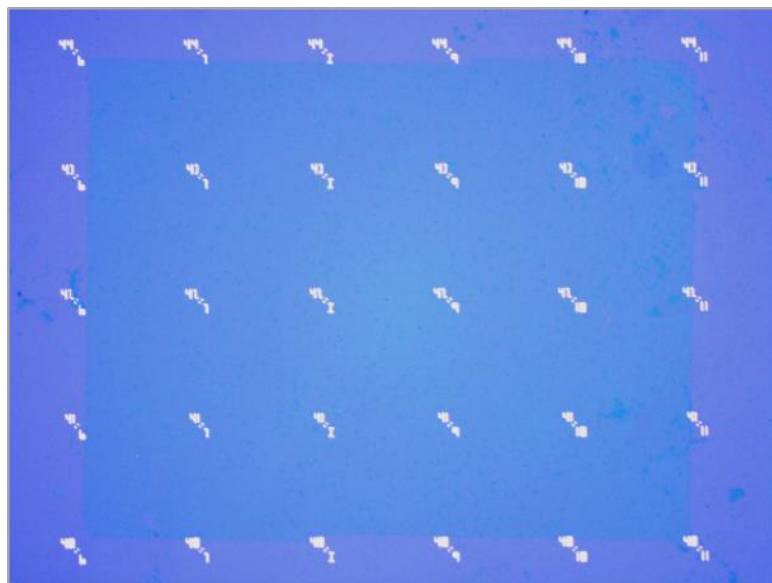


**Figure 5.3 Schematic process flow for the fabrication of pillar arrays on graphene.**

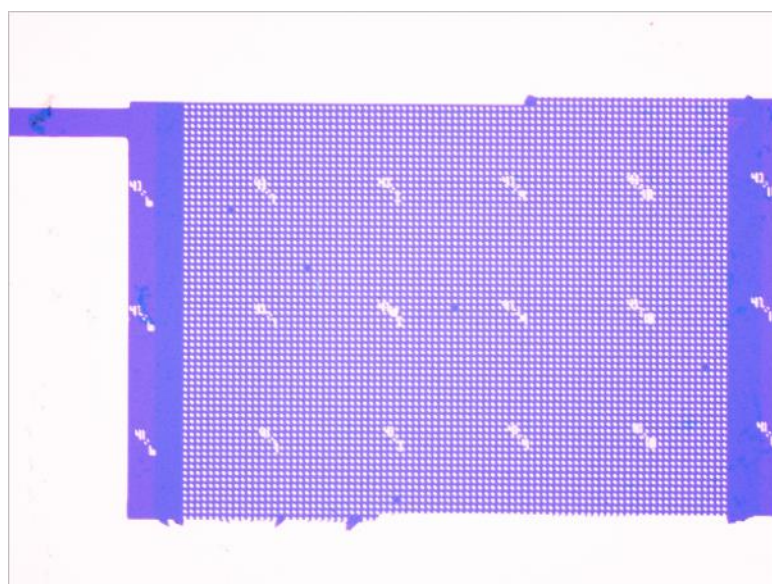
Figure 5.4 shows a graphene sample fabricated with the process just described.

Figure 5.4(a) is an optical microscope image of an 800x1000  $\mu\text{m}^2$  sheet of CVD graphene

after the patterning step of Figure 5.3(g). The same sample after fabrication of the source-drain contacts and a 2D array with 10- $\mu\text{m}$  period and 5- $\mu\text{m}$  pillar diameter is shown in Figure 5.4(b).



(a)



(b)

**Figure 5.4 CVD graphene for transmission measurements, after patterning (a) and after deposition of the pillar array and source-drain contacts (b).**

The electrical characteristics of these samples were measured using the same method described in Section 3.4 to confirm the graphene quality after all the fabrication

processes. The measured mobilities are in the range of 2000-6000  $\text{cm}^2/\text{Vs}$  which is quite good for CVD graphene.

### 5.3 Transmission spectroscopy and electroluminescence results

The samples just described were characterized via transmission measurements using the FTIR spectrometer. Representative results are shown in Figure 5.5(a) and 5.5(b), measured with two different samples having 1.5- $\mu\text{m}$  and 5- $\mu\text{m}$  array period, respectively. In each case, the sample is held at room temperature, and several spectra are recorded for different values of the gate voltage  $V_{\text{gs}}$  (listed in the caption relative to the charge neutrality point  $V_{\text{cnp}}$ ). The traces shown in both figures are normalized to the transmission spectrum of the respective device at  $V_{\text{cnp}}$ , where no plasmons can be excited due to the very low carrier density. In Figure 5.5(a), a sharp transmission dip around  $240 \text{ cm}^{-1}$  (7.2 THz) is observed, in agreement with the expected grating-coupled plasmon frequency of equation (5.5) for  $\Lambda = 1.5 \mu\text{m}$  and carrier densities in the order of  $10^{12} \text{ cm}^{-2}$ . If the period is increased to 5  $\mu\text{m}$ , as in the device of Figure 5.5(b), the transmission dip is red shifted to the  $117\text{-}122 \text{ cm}^{-1}$  (3.5-3.7 THz) range, again consistent with the predictions of equation (5.5). The results of similar measurements with several other devices of different array period are summarized in Figure 5.6, where the geometrical tunability of the graphene plasmon resonance across the THz spectrum is clearly illustrated.

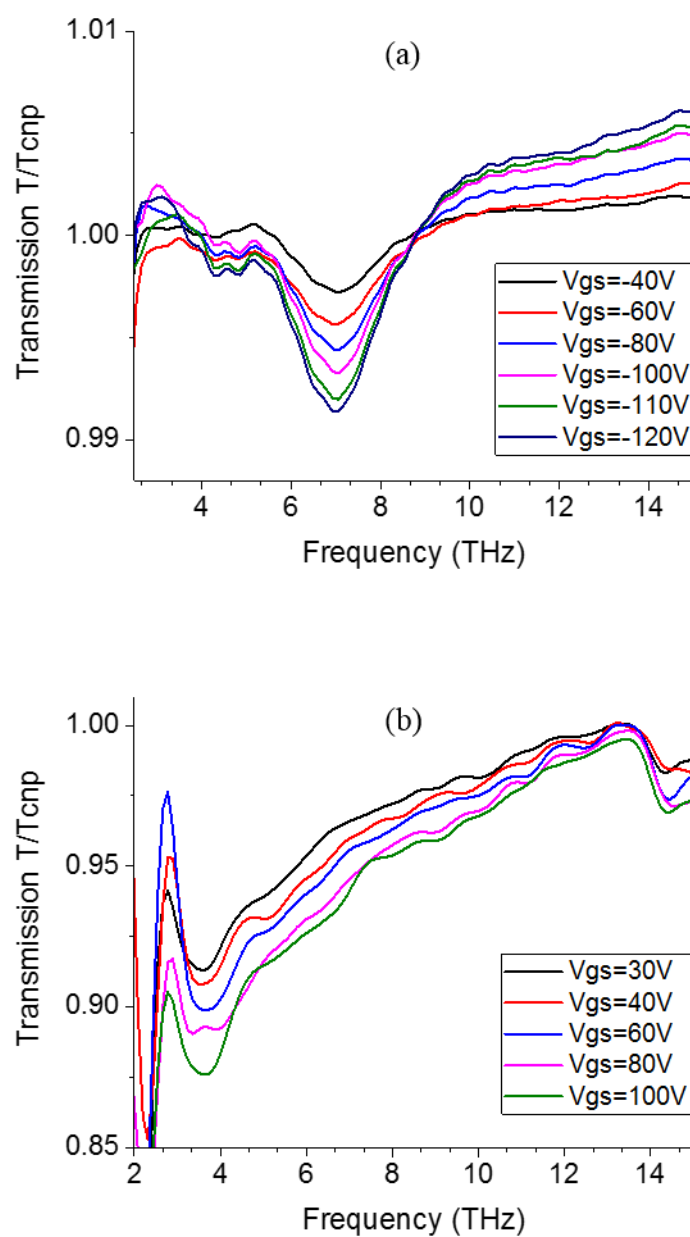


**Figure 5.5** Transmission spectrum from plasmons graphene sample with 1.5 $\mu\text{m}$  period (a) and 5 $\mu\text{m}$  period (b) 2D metal pillar array.

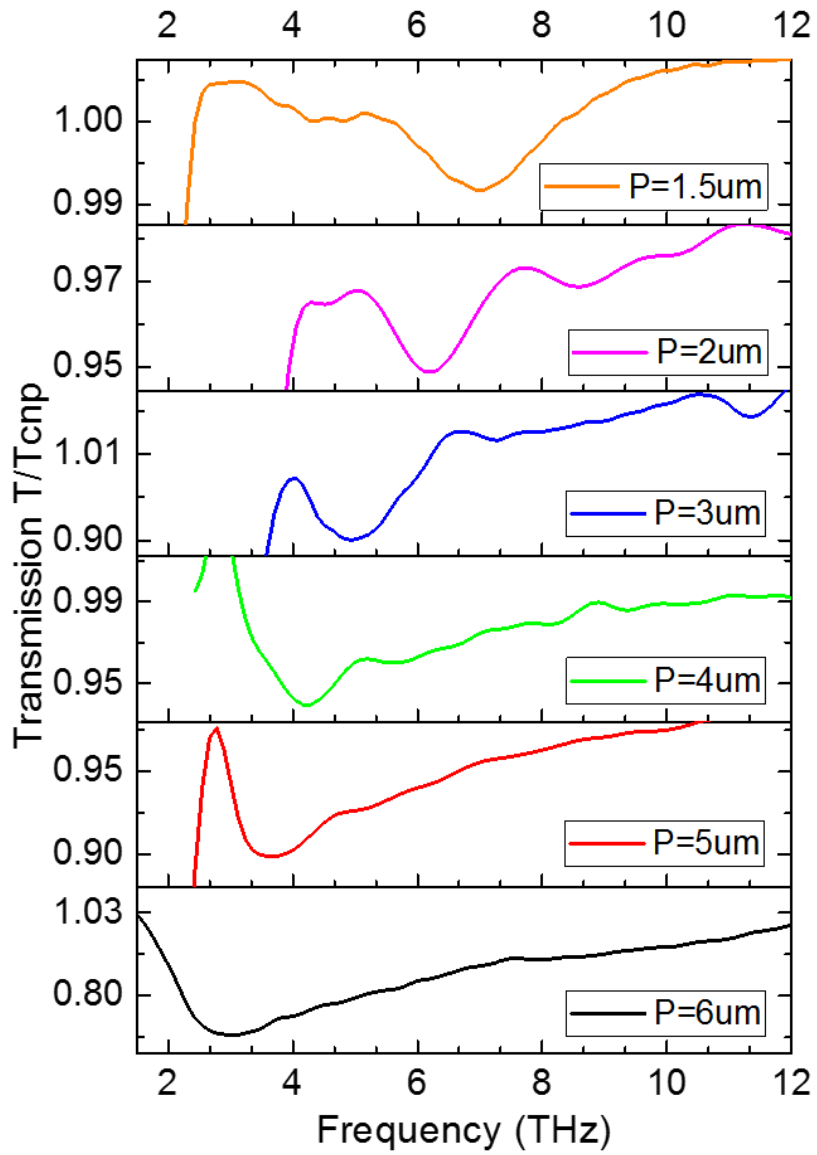


**Figure 5.6** Transmission spectrum from plasmons graphene sample with different period  $P$ .

In each device, increasing the gate voltage away from the charge neutrality point (i.e., increasing  $|V_{gs}-V_{cnp}|$ ) has the effect of producing stronger plasmonic absorption, due to the corresponding increase in the overall carrier density in the graphene sheet.

Furthermore, a small blue shift in the frequency of peak absorption with increasing gate voltage is also observed, as shown most clearly in Figure 5.5(b). This shift however is generally found to be smaller than predicted by combining equation (5.5) with equation (1.2). The likely explanation for this discrepancy is a large variation in carrier density across the sample area, with the regions of highest density producing the strongest contribution to the plasmonic absorption. Therefore, as  $|V_{gs}-V_{cnp}|$  is increased, the absorption strength increases since a larger and larger fraction of the sample area contains a high density of carriers, but the frequency of peak absorption does not tune as effectively. In any case, the plasmonic resonances revealed by the data of Figure 5.5 Figure 5.6 are promising for applications in THz photonics, including the development of spatial light modulators for imaging and spectroscopic sensors.

## 6 CONCLUSION

In this thesis work, the generation of THz radiation based on cyclotron-like emission and the Smith-Purcell effect in graphene and in 1D carbon conductors on nanoscale gratings is investigated numerically and experimentally. Full-wave electrodynamic simulations combined with a basic model of charge transport are applied in the calculations. The simulation results indicate that technologically significant power levels of several  $\mu\text{W}/\text{mm}^2$  can be obtained at geometrically tunable THz frequencies. In particular, cyclotron radiation from AC-SWNTs provides the most efficient mechanism with the narrowest emission peaks, compared to the other structures considered in this thesis. In practice, the initial experimental results demonstrate electroluminescence at 8 THz from the electron beam in an hBN/graphene/hBN stack transferred on a 150-nm-period hole array, in agreement with numerical simulations of Smith-Purcell emission. Finally, tunable THz absorption from plasmons in CVD graphene coated with a 2D array of metallic nanocylinders is also observed experimentally in this work.

To further develop this study in the future, Smith-Purcell radiation from graphene on nanoscale gratings can be investigated with different hole array periods to verify its tunable emission frequency. The hole depth and size are also interesting parameters to control the Smith-Purcell effect and optimize its output power. In contrast, THz cyclotron radiation from graphene is more challenging to demonstrate experimentally, due to the difficulty of producing good graphene conformation on the corrugated substrate and the resulting strain variations that can decrease the sample quality. THz radiation from 1D carbon conductors (i.e., ZZ-GNRs and AC-SWNTs) is also intriguing due to its higher

efficiency and narrower emission spectra predicted by the simulation result. Finally, THz emission from graphene plasmons should be pursued by optimizing hot-carrier injection and plasmon diffraction in the grating-coupled samples studied in the final section of this thesis.

**BIBLIOGRAPHY**

- Bahk, Young-mi, Gopakumar Ramakrishnan, Jongho Choi, Hyelynn Song, Geunchang Choi, Yong Hyup Kim, Kwang Jun Ahn, Dai-Sik Kim, and Paul C M Planken. 2014. "Plasmon Enhanced Terahertz Emission from Single Layer Graphene." *ACS Nano* 8 (9): 9089–9096.
- Baringhaus, Jens, Ming Ruan, Frederik Edler, Antonio Tejada, Muriel Sicot, Amina Taleb-Ibrahimi, An-Ping Li, et al. 2014. "Exceptional Ballistic Transport in Epitaxial Graphene Nanoribbons." *Nature* 506 (7488): 349–354.
- Berger, Claire, Zhimin Song, Xuebin Li, Xiaosong Wu, Nate Brown, Cécile Naud, Didier Mayou, et al. 2006. "Electronic Confinement and Coherence in Patterned Epitaxial Graphene." *Science* 312 (5777): 1191–1196.
- Bolotin, K. I., K. J. Sikes, J. Hone, H. L. Stormer, and P. Kim. 2008. "Temperature-Dependent Transport in Suspended Graphene." *Physical Review Letters* 101 (9): 096802.
- Boubanga-Tombet, S., S. Chan, T. Watanabe, A. Satou, V. Ryzhii, and T. Otsuji. 2012. "Ultrafast Carrier Dynamics and Terahertz Emission in Optically Pumped Graphene at Room Temperature." *Physical Review B* 85 (3): 035443.
- Bratman, V. L., B. S. Dumes, A. E. Fedotov, P. B. Makhalov, B. Z. Movshevich, and F. S. Rusin. 2010. "Terahertz Orotrons and Oromultipliers." *IEEE Transactions on Plasma Science* 38 (6): 1466–1471.
- Castro Neto, A. H., N. M. R. Peres, K. S. Novoselov, A. K. Geim, and F. Guinea. 2009. "The Electronic Properties of Graphene." *Reviews of Modern Physics* 81 (1): 109–162.
- Datta, Supriyo. 1995. *Electronic Transport in Mesoscopic Systems*. Cambridge University Press.
- Dean, C. R., A. F. Young, I. Meric, C. Lee, L. Wang, S. Sorgenfrei, K. Watanabe, et al. 2010. "Boron Nitride Substrates for High-Quality Graphene Electronics." *Nature Nanotechnology* 5 (10): 722–726.
- Dorgan, Vincent E., Myung Ho Bae, and Eric Pop. 2010. "Mobility and Saturation Velocity in Graphene on SiO<sub>2</sub>." *Applied Physics Letters* 97 (8): 082112.
- Dragoman, D., and M. Dragoman. 2004. "Terahertz Oscillations in Semiconducting Carbon Nanotube Resonant-Tunneling Diodes." *Physica E* 24 (3-4): 282–289.
- Du, Xu, Ivan Skachko, Anthony Barker, and Eva Y. Andrei. 2008. "Approaching Ballistic Transport in Suspended Graphene." *Nature Nanotechnology* 3 (8): 491–495.
- "FDTD Solutions." 2009. Vancouver: Lumerical Solutions.

- “FDTD Solutions.” 2015. Vancouver: Lumerical Solutions.
- Fedorchenko, A. I., H. H. Cheng, G. Sun, and R. A. Soref. 2010. “Radiation Emission from Wrinkled SiGe/SiGe Nanostructure.” *Applied Physics Letters* 96 (11): 113104.
- Frank, S., P. Poncharal, Z. L. Wang, and W. A. de Heer. 1998. “Carbon Nanotube Quantum Resistors.” *Science* 280 (5370): 1744–1746.
- Gao, Weilu, Jie Shu, Ciyuan Qiu, and Qianfan Xu. 2012. “Excitation of Plasmonic Waves in Graphene by Guided-Mode Resonances.” *ACS Nano* 6 (9): 7806–7813.
- Hartmann, R. R., J. Kono, and M. E. Portnoi. 2014. “Terahertz Science and Technology of Carbon Nanomaterials.” *Nanotechnology* 25: 322001.
- Hirakawa, K., K. Yamanaka, M. Grayson, and D. C. Tsui. 1995. “Far-infrared emission-spectroscopy of hot 2-dimension plasmons in Al<sub>0.3</sub>Ga<sub>0.7</sub>As/GaAs heterojunctions.” *Applied Physics Letters* 67 (16): 2326–2328.
- Höpfel, Ralph A., Erich Vass, and Erich Gornik. 1982. “Thermal Excitation of Two-Dimensional Plasma Oscillations.” *Physical Review Letters* 49 (22): 1667–1671.
- Hwang, E. H., S. Adam, and S. Das Sarma. 2007. “Carrier Transport in Two-Dimensional Graphene Layers.” *Physical Review Letters* 98 (18): 186806.
- Jablan, Marinko, Hrvoje Buljan, and Marin Soljačić. 2009. “Plasmonics in Graphene at Infrared Frequencies.” *Physical Review B - Condensed Matter and Materials Physics* 80 (24): 245435.
- Jackson, J D. 1975. *Classical Electrodynamics*. New York: Wiley.
- Javey, Ali, Jing Guo, Magnus Paulsson, Qian Wang, David Mann, Mark Lundstrom, and Hongjie Dai. 2004. “High-Field Quasiballistic Transport in Short Carbon Nanotubes.” *Physical Review Letters* 92 (10): 106804.
- Ju, Long, Baisong Geng, Jason Horng, Caglar Girit, Michael Martin, Zhao Hao, Hans a Bechtel, et al. 2011. “Graphene Plasmonics for Tunable Terahertz Metamaterials.” *Nature Nanotechnology* 6 (10): 630–634.
- Kang, Seong Jun, Coskun Kocabas, Taner Ozel, Moonsub Shim, Ninad Pimparkar, Muhammad a Alam, Slava V Rotkin, and John a Rogers. 2007. “High-Performance Electronics Using Dense, Perfectly Aligned Arrays of Single-Walled Carbon Nanotubes.” *Nature Nanotechnology* 2 (4): 230–236.
- Katsnelson, M. I. 2012. *Graphene: Carbon in Two-Dimensions*. Cambridge University Press.
- Kibis, O. V., D. G. W. Parfitt, and M. E. Portnoi. 2005. “Superlattice Properties of Carbon Nanotubes in a Transverse Electric Field.” *Physical Review B* 71: 035411.

- Kibis, O. V., M. Rosenau Da Costa, and M. E. Portnoi. 2007. "Generation of Terahertz Radiation by Hot Electrons in Carbon Nanotubes." *Nano Letters* 7 (11): 3414–3417.
- Kittel, Charles. 1986. *Introduction to Solid State Physics*. New York: Wiley.
- Köhler, Rüdiger, Alessandro Tredicucci, Fabio Beltram, Harvey E. Beere, Edmund H. Linfield, A. Giles Davies, and David A. Ritchie. 2002. "High-Intensity Interminiband Terahertz Emission from Chirped Superlattices." *Applied Physics Letters* 80 (11): 1867–1869.
- Koppens, Frank H. L., Darrick E. Chang, and F. Javier Garcia De Abajo. 2011. "Graphene Plasmonics: A Platform for Strong Light-Matter Interactions." *Nano Letters* 11 (8): 3370–3377.
- Lee, Mark, and Michael C. Wanke. 2007. "Searching for a Solid-State Terahertz Technology." *Science* 316 (5821): 64–65.
- Liu, Peter Q., Federico Valmorra, Curdin Maissen, and Jerome Faist. 2015. "Electrically Tunable Graphene Anti-Dot Array Terahertz Plasmonic Crystals Exhibiting Multi-Band Resonances." *Optica* 2 (2): 135.
- Liu, Shenggang, Chao Zhang, Min Hu, Xiaoxing Chen, Ping Zhang, Sen Gong, Tao Zhao, and Renbin Zhong. 2014. "Coherent and Tunable Terahertz Radiation from Graphene Surface Plasmon Polaritons Excited by an Electron Beam." *Applied Physics Letters* 104 (20): 201104.
- Low, Tony, and Phaedon Avouris. 2014. "Graphene Plasmonics for Terahertz to Mid-Infrared Applications." *ACS Nano* 8 (2) 1086–1101.
- Luo, Chiyan, Mihai Ibanescu, Steven G. Johnson, and J. D. Joannopoulos. 2003. "Cerenkov Radiation in Photonic Crystals." *Science* 299 (2003): 368–371.
- Marshall, T. C. 1985. *Free Electron Lasers*. New York: Macmillan.
- Mayorov, Alexander S., Roman V. Gorbachev, Sergey V. Morozov, Liam Britnell, Rashid Jalil, Leonid A. Ponomarenko, Peter Blake, et al. 2011. "Micrometer-Scale Ballistic Transport in Encapsulated Graphene at Room Temperature." *Nano Letters* 11 (6): 2396–2399.
- Nakada, Kyoko, Mitsutaka Fujita, Gene Dresselhaus, and Mildred Dresselhaus. 1996. "Edge State in Graphene Ribbons: Nanometer Size Effect and Edge Shape Dependence." *Physical Review B* 54 (24): 17954–17961.
- Nemilentsau, A. M., G. Ya Slepyan, and S. A. Maksimenko. 2007. "Thermal Radiation from Carbon Nanotubes in the Terahertz Range." *Physical Review Letters* 99 (14): 147403.

- Novoselov, K. S., A. K. Geim, S. V. Morozov, D. Jiang, M. I. Katsnelson, I. V. Grigorieva, S. V. Dubonos, and A. A. Firsov. 2005. "Two-Dimensional Gas of Massless Dirac Fermions in Graphene." *Nature* 438 (7065): 197–200.
- Novoselov, K. S., A. K. Geim, S. V. Morozov, D. Jiang, Y. Zhang, S. V. Dubonos, I. V. Grigorieva, and A. A. Firsov. 2004. "Electric Field Effect in Atomically Thin Carbon Films." *Science* 306 (5696): 666–669.
- Oster, Ludwig. 1960. "Effects of Collisions on the Cyclotron Radiation from Relativistic Particles." *Physical Review* 119: 1444–1456.
- Palacios, J. J., J. Fernández-Rossier, L. Brey, and H. A. Fertig. 2010. "Electronic and Magnetic Structure of Graphene Nanoribbons." *Semiconductor Science and Technology* 25: 033003.
- Park, Ji Yong, Sami Rosenblatt, Yuval Yaish, Vera Sazonova, Hande Üstünel, Stephan Braig, T. A. Arias, Piet W. Brouwer, and Paul L. McEuen. 2004. "Electron-Phonon Scattering in Metallic Single-Walled Carbon Nanotubes." *Nano Letters* 4 (3): 517–520.
- Peach, G. 1981. "Theory of the Pressure Broadening and Shift of Spectral Lines." *Advances in Physics* 30 (3): 367–474.
- Portnoi, M.E., O.V. Kibis, and M. Rosenau da Costa. 2008. "Terahertz Applications of Carbon Nanotubes." *Superlattices and Microstructures* 43 (5-6): 399–407.
- Prechtel, Leonhard, Li Song, Dieter Schuh, Pulickel Ajayan, Werner Wegscheider, and Alexander W. Holleitner. 2012. "Time-Resolved Ultrafast Photocurrents and Terahertz Generation in Freely Suspended Graphene." *Nature Communications* 3: 646.
- Purewal, Meninder S., Byung Hee Hong, Anirudhh Ravi, Bhupesh Chandra, James Hone, and Philip Kim. 2007. "Scaling of Resistance and Electron Mean Free Path of Single-Walled Carbon Nanotubes." *Physical Review Letters* 98 (18): 186808.
- Rana, F. 2008. "Graphene Terahertz Plasmon Oscillators." *IEEE Transactions on Nanotechnology* 7 (1): 91–99.
- Ren, Lei, Qi Zhang, Jun Yao, Zhengzong Sun, Ryosuke Kaneko, Zheng Yan, S?bastien Nanot, et al. 2012. "Terahertz and Infrared Spectroscopy of Gated Large-Area Graphene." *Nano Letters* 12 (7): 3711–3715.
- Rochat, Michel, Jérôme Faist, Mattias Beck, Ursula Oesterle, and Marc Illegems. 1998. "Far-Infrared ( $\lambda=88 \mu\text{m}$ ) Electroluminescence in a Quantum Cascade Structure." *Applied Physics Letters* 73 (25): 3724–3726.
- Ryzhii, V., M. Ryzhii, and T. Otsuji. 2007. "Negative Dynamic Conductivity of Graphene with Optical Pumping." *Journal of Applied Physics* 101: 083114.

- Saito, Riichiro, Gene Dresselhaus, and Mildred S. Dresselhaus. 1998. *Physical Properties of Carbon Nanotubes*. Imperial College Press.
- Sensale-Rodriguez, Berardi, Rusen Yan, Michelle M Kelly, Tian Fang, Kristof Tahy, Wan Sik Hwang, Debdeep Jena, Lei Liu, and Huili Grace Xing. 2012. "Broadband Graphene Terahertz Modulators Enabled by Intraband Transitions." *Nature Communications* 3: 780.
- Smith, Don D, and Alexey Belyanin. 2011. "Room-Temperature Semiconductor Coherent Smith-Purcell Terahertz Sources." *Applied Physics Letters* 98 (6): 063501.
- Smith, S. J., and E. M. Purcell. 1953. "Visible Light from Localized Surface Charges Moving across a Grating." *Physical Review* 92 (4): 1069.
- Sun, Dong, Charles Divin, Julien Rioux, John E. Sipe, Claire Berger, Walt A. De Heer, Phillip N. First, and Theodore B. Norris. 2010. "Coherent Control of Ballistic Photocurrents in Multilayer Epitaxial Graphene Using Quantum Interference." *Nano Letters* 10 (4): 1293–1296.
- Tantiwanichapan, Khwanchai, Jeff DiMaria, Shayla N. Melo, and Roberto Paiella. 2013. "Graphene Electronics for Terahertz Electron-Beam Radiation." *Nanotechnology* 24 (37): 375205.
- Tantiwanichapan, Khwanchai, Anna K. Swan, and Roberto Paiella. 2016. "One-Dimensional Carbon Nanostructures for Terahertz Electron-Beam Radiation." *Submitted*.
- Tantiwanichapan, Khwanchai, Xuanye Wang, Anna K. Swan, and Roberto Paiella. 2014. "Graphene on Nanoscale Gratings for the Generation of Terahertz Smith-Purcell Radiation." *Applied Physics Letters* 105 (24): 241102.
- Titova, Lyubov V., Cary L. Pint, Qi Zhang, Robert H. Hauge, Junichiro Kono, and Frank A. Hegmann. 2015. "Generation of Terahertz Radiation by Optical Excitation of Aligned Carbon Nanotubes." *Nano Letters* 15 (5): 3267–3272.
- Tredicucci, Alessandro, and Miriam Serena Vitiello. 2014. "Device Concepts for Graphene-Based Terahertz Photonics." *IEEE Journal on Selected Topics in Quantum Electronics* 20 (1): 8500109.
- van den Berg, P. M., and T. H. Tan. 1974. "Smith—Purcell Radiation from a Line Charge Moving Parallel to a Reflection Grating with Rectangular Profile." *Journal of the Optical Society of America* 64 (6): 325.
- Vicarelli, L., M. S. Vitiello, D. Coquillat, A. Lombardo, a. C. Ferrari, W. Knap, M. Polini, V. Pellegrini, and A. Tredicucci. 2012. "Graphene Field-Effect Transistors as Room-Temperature Terahertz Detectors." *Nature Materials* 11 (10): 865–871.

- Wakabayashi, Katsunori, Yositake Takane, and Manfred Sigrist. 2007. "Perfectly Conducting Channel and Universality Crossover in Disordered Graphene Nanoribbons." *Physical Review Letters* 99 (3): 036601.
- Wang, L, I Meric, P Y Huang, Q Gao, Y Gao, H Tran, T Taniguchi, et al. 2013. "One-Dimensional Electrical Contact to a Two-Dimensional Material." *Science* 342 (6158): 614–617.
- Wang, Xuanye, Khwanchai Tantiwanichapan, Jason W. Christopher, Roberto Paiella, and Anna K. Swan. 2015. "Uniaxial Strain Redistribution in Corrugated Graphene: Clamping, Sliding, Friction, and 2D Band Splitting." *Nano Letters* 15 (9): 5969–5975.
- White, C. T., and T. N. Todorov. 1998. "Carbon Nanotubes as Long Ballistic Conductors." *Nature* 393 (6682): 240–242.
- Williams, Benjamin S. 2007. "Terahertz Quantum-Cascade Lasers." *Nature Photonics* 1: 517–525.
- Williams, Benjamin S., Bin Xu, Qing Hu, and Michael R. Melloch. 1999. "Narrow-Linewidth Terahertz Intersubband Emission from Three-Level Systems." *Applied Physics Letters* 75 (19): 2927–2929.
- Wirner, C., C. Kiener, W. Boxleitner, M. Witzany, E. Gornik, P. Vogl, G. Bohm, and G. Weimann. 1993. "Direct Observation of the Hot Electron Distribution Function in GaAs/AlGaAs Heterostructures." *Physic Review Letter* 70 (17): 2609–2612.
- Xu, Bin, Qing Hu, and Michael R. Melloch. 1997. "Electrically Pumped Tunable Terahertz Emitter Based on Intersubband Transition." *Applied Physics Letters* 71: 440.
- Yan, Hugen, Xuesong Li, Bhupesh Chandra, George Tulevski, Yanqing Wu, Marcus Freitag, Wenjuan Zhu, Phaedon Avouris, and Fengnian Xia. 2012. "Tunable Infrared Plasmonic Devices Using Graphene/insulator Stacks." *Nature Nanotechnology* 7 (5): 330–334.
- Zhang, Yuanbo, Yan-Wen Tan, Horst L. Stormer, and Philip Kim. 2005. "Experimental Observation of the Quantum Hall Effect and Berry's Phase in Graphene." *Nature* 438 (7065): 201–204.

**CURRICULUM VITAE****KHWANCHAI TANTIWANICHAPAN**

khwan@bu.edu

**EDUCATION**

PhD in Electrical Engineering, 2016

*Boston University, Boston MA*

MS in Electrical Engineering, 2011

*Boston University, Boston MA*

BS in Electronic Engineering and Technology, 2001

*King Mongkut's Institute of Technology Ladkrabang, Bangkok Thailand*

**RESEARCH AND TEACHING**

Boston University, Boston MA

*Research Assistant*

- Development of light emitting devices based on cyclotron radiation from mechanically corrugated graphene on SiO<sub>2</sub> sinusoidal gratings. Simulate radiation from cyclotron radiation in graphene by using FDTD. Design and fabricate SiO<sub>2</sub> sinusoidal grating samples. Design and setup test station for I-V measurement to characterize graphene mobility.
- Development of light emitting devices based on Smith-Purcell radiation from hBN-graphene-hBN nanoscale gratings. Simulate radiation from Smith-Purcell radiation in graphene on hole-arrays by using FDTD. Design and fabricate SiO<sub>2</sub> 2D nanoscale hole-array grating samples. Design and setup the emission measurement at low temperature by using FTIR, Cryostat, and Lock-In Amplifier.

- Simulate radiation from cyclotron radiation and Smith-Purcell radiation in zigzag graphene nanoribbons and armchair single wall carbon nanotube.
- Development of light emitting devices based on plasmons in graphene from metal coupled-grating on CVD graphene. Design and fabricate 2D microscale metal pillar arrays on CVD graphene samples. Design and setup the emission measurement at low temperature by using FTIR, Cryostat, and Lock-In Amplifier.

Boston University, Boston MA

#### *Teaching Assistant*

- Courses taught: “Introduction to Photonics Lab”, “Photonics Lab”

### **PUBLICATIONS**

#### *Journal Articles*

- **K. Tantiwanichapan**, J. DiMaria, S. N. Melo, and R. Paiella, “Graphene electronics for terahertz electron-beam radiation,” *Nanotechnology* **24**, 375205 (2013).
- **K. Tantiwanichapan**, X. Wang, A. K. Swan, and R. Paiella, “Graphene on nanoscale gratings for the generation of terahertz Smith-Purcell radiation,” *Appl. Phys. Lett.* **105**, 241102 (2014).
- **K. Tantiwanichapan**, A.K. Swan, and R. Paiella., “One-dimensional carbon nanostructures for terahertz electron-beam radiation,” submitted (2016)
- X. Wang, **K. Tantiwanichapan**, J. W. Christopher, R. Paiella, and A. K. Swan., “Uniaxial Strain Redistribution in Corrugated Graphene: Clamping, Sliding, Friction, and 2D Band Splitting,” *Nano Letters* **15**, 5969-5975 (2015)

#### *Conference Presentations*

- X. Wang, **K. Tantiwanichapan**, R. Paiella, A. K. Swan., “How strain affect graphene’s optical contrast on SiO<sub>2</sub>/Si gratings”, MRS March Meeting 2014.
- **K. Tantiwanichapan**, X. Wang, J. Dimaria, S. Melo, A. K. Swan, and R. Paiella., “Graphene on Nanoscale Gratings for Terahertz Electron-Beam Radiation”, MRS Fall Meeting 2014.
- X. Wang, **K. Tantiwanichapan**, J. W. Christopher, R. Paiella, and A. K. Swan., “Strain variation in corrugated graphene”, MRS March Meeting 2015.

- **K. Tantiwanichapan**, X. Wang, A. K. Swan, and R. Paiella., “Graphene on nanoscale gratings for terahertz Smith-Purcell radiation”, Conference on Lasers and Electro-Optics(CLEO) 2015.
- **K. Tantiwanichapan**, X. Wang, A. K. Swan, and R. Paiella., “Graphene on nanoscale gratings: a novel materials platform for THz electron-beam radiation”, Advance Photonics 2015.
- **K. Tantiwanichapan**, X. Wang, A. K. Swan, and R. Paiella., “Terahertz Electron-Beam Radiation in Graphene”, Conference on Metamaterials Photonic Crystals and Plasmonics. 2016.